

UC Irvine

UC Irvine Electronic Theses and Dissertations

Title

Development and optimization of the Virus-Bioresistor: A potential Point-of-care diagnostic platform

Permalink

<https://escholarship.org/uc/item/7h20h739>

Author

Bhasin, Apurva

Publication Date

2020

Peer reviewed|Thesis/dissertation

UNIVERSITY OF CALIFORNIA,
IRVINE

Development and optimization of the Virus-Bioresistor:
A potential Point-of-care diagnostic platform

DISSERTATION

submitted in partial satisfaction of the requirements
for the degree of

DOCTOR OF PHILOSOPHY

in Chemistry

by

Apurva Bhasin

Dissertation Committee:
Professor Reginald M. Penner, Chair
Associate Professor Shane Ardo
Professor Andrej Luptak
Professor Regina Ragan

2020

Portion of Chapter 1 © 2020 American Chemical Society

Chapter 2 © 2020 American Chemical Society

Chapter 3 © 2020 American Chemical Society

Chapter 4 © 2020 Apurva Bhasin

All other materials © 2020 Apurva Bhasin

DEDICATION

To my family and friends.

This dissertation couldn't be possible without my father, who believed in me and sowed the seed for pursuing PhD; my mother, who assured me a smooth transition from a country to another.

To friends back in India, who never seem to be far and to those I met in US, who were a family away from home.

To my nani, for being the strong woman, I look up to and who will always be a constant source of inspiration.

To my nana, who has always got my back from day one of this journey.

To Yash, for existing and making my research life busier and personal life easier.

I know the price of success: dedication, hard work and an unremitting devotion to the things you want to see happen. ~ *Frank Lloyd Wright*

TABLE OF CONTENTS

	Page
LIST OF FIGURES	vi
LIST OF TABLES	xiv
ACKNOWLEDGEMENTS	xv
VITA	xvi
ABSTRACT OF THE DISSERTATION	xviii
Chapter 1.....	1
Introduction	1
1.1 Nanomaterials involved in biosensor construction.....	2
1.2 Transduction principles and strategies for signal generation.....	4
1.3 The Virus bio-resistor and quest for cancer detection.....	7
1.4 Phage display for customized affinity and specificity.....	7
1.5 Biosensor journey preceding VBR in Penner Group	9
1.5.1 A Covalent Virus Layer (CVL).....	9
1.5.2 Mass-Based Signal Transduction of the CVL.....	11
1.5.3 Electrochemical Signal Transduction of the CVL.....	13
1.6 Virus-PEDOT Bioaffinity Layers	14
1.6.1 Electrodepositing a Virus-PEDOT Composite Film.....	14
1.7 Biosensing with Virus-PEDOT Nanowires.	18
1.8 Electrochemical Signal Transduction for virus-PEDOT films.	19
1.9. The two-sided virus-PEDOT biosensor.....	21
1.10 Scope of this dissertation.....	23
Chapter 2.....	25
The Virus Bioresistor: Wiring Virus Particles for the Direct, Label-Free Detection of Target Proteins.....	25
2.1 Introduction	26
2.2 Experimental Methods.....	28
2.2.1 Materials.....	28
2.2.2 Phage Library Design and the Selection of HSA Binders	28

2.2.3 VBR Fabrication	28
2.2.4 Impedance Spectroscopy (IS).....	31
2.2.5 AFM and SEM Analysis.	31
2.3 Results and Discussion	32
2.4 Summary.....	43
Chapter 3.....	44
The Virus Bioresistor: Wiring Virus Particles for the Direct, Label-Free Detection of Target Proteins.....	44
3.1 Introduction	45
3.2 Experimental methods.....	46
3.2.1 Materials and methods.....	46
3.2.2 VBR Fabrication.....	48
3.2.3 Impedance Spectroscopy (IS).....	49
3.2.4 Time scan experiment.....	49
3.2.5 Control experiments	50
3.2.6 SEM Analysis	50
3.3 Results and Discussion	50
3.3.1 VBR Fabrication and Characterization.....	50
3.3.2 VBR Electrical Response and Signal.....	56
3.3.3. Tuning the VBR signal amplitude using $R_{PEDOT-PSS}$	60
3.3.4. A proposed mechanism for VBR signal generation.....	68
3.4 Summary	74
Chapter 4.....	77
Oxidized VBR for detecting antibodies	77
4.1 Introduction	78
4.2 Experimental Methods.....	83
4.2.1 Antibodies and reagents:.....	83
4.2.2 VBR Fabrication.....	84
4.2.3 Impedance Spectroscopy (IS).....	85
4.2.4 Control experiments.....	85
4.2.5 SEM Analysis	86
4.3 Results and Discussion	86

4.3.1 Fabrication of <i>VBR</i>	86
4.3.2 Optimization of oxidation method: CA vs potentiodynamic oxidation.....	88
4.3.3 Detection of DJ1 protein for sensor optimization	89
4.3.4 Antibody detection with oxidized <i>VBR</i>	91
4.3.5 Serum measurements	96
4.4 Summary.....	97
Bibliography.....	99
Appendix A.....	110
Supplementary information for Chapter 3.....	110

LIST OF FIGURES

Figure 1.1 The covalent virus surface (CVS). a). Stepwise assembly (steps 1–3) and functionalization (steps 4–6) of the CVS. (b-d) Noncontact mode AFM images ($1\ \mu\text{m} \times 1\ \mu\text{m}$). (b) A single M13 virion on mica, (c) A self-assembled monolayer (SAM) of N-hydroxysuccinimide thioctic ester on gold after exposure to BSA. No virus particles were attached to this surface. The dark fissure at upper right is a grain boundary. (d) A functional CVS consisting of a SAM of N-hydroxysuccinimide thioctic ester (NHS-TE) on polycrystalline gold, reacted first with M13 to produce covalent attachment, and then exposed to BSA (Figure 1, step 3). After Ref.43..... 10

Figure 1.2 Quartz Crystal Microbalance (QCM) studies of covalent virus surfaces. a,b) Schematic diagram of the QCM and flow cell used for investigations of the CVS. c). QCM evaluation of the efficacy of three wash solutions: (top) 0.1 M glycine (pH~2 adjusted with HCl), (middle) 0.25 M HCl, and (bottom) 0.5 M HCl. d,e). d) Plot of mass vs time (top) for the exposure of a CVS to doses of p-Ab, ranging in concentration from 6.6 to 200 nM. Bound p8-Ab was removed after each injection using 0.5 M HCl. f) Plot of maximum mass change vs p8-Ab concentration for the data shown in (d,e). The mass change was proportional to the concentrations of injected p8-Ab ($R^2 = 0.997$) and yielded a sensitivity of $0.018\ \mu\text{g cm}^{-2}/\text{nM}$ and a limit of detection (LOD) of 6.6 nM. 12

Figure 1.3 Electrodeposition of a virus-PEDOT bioaffinity layer. a). The virus-PEDOT electrodeposition reaction, b). QCM analysis of virus-PEDOT electrodeposition shows increased mass loading as a decrease in frequency. c) Frequency change versus deposition charge, Q_{tot} , for QCM measurements. The positive deviation of Δf for virus-containing solutions is due to virus incorporation into these films. d) Calibration curve showing the linear correlation of the virus concentration within the PEDOT film (vertical axis) versus the concentration of virus in solution. (e-j). Topography of virus-PEDOT films imaged by scanning electron microscopy at two magnifications. All films were prepared using 10 deposition cycles (20 mV/s) from a solution of aqueous 12.5 mM LiClO_4 , 2.5 mM EDOT, and virus particles at three concentrations: (e,f) $[\text{virus}]_{\text{soln}} = 3\ \text{nM}$, (g,h) $[\text{virus}]_{\text{soln}} = 9\ \text{nM}$, and (I,j) $[\text{virus}]_{\text{soln}} = 15\ \text{nM}$ 17

Figure 1.4 PSMA Detection in Synthetic Urine Using Synergistic, Dual-Ligand Phage. a) Schematic diagram of bidentate binding to PSMA by chemically synthesized (KCS-1, green) and genetically encoded (peptide, red) ligands to PSMA. The former ligand wraps non-covalently onto the negatively charged P8 proteins found on the phage surface due to conjugation with a positively charged K14 peptide (blue). Simultaneous binding by the two

ligands provides higher apparent affinity to PSMA. b). Schematic diagram showing the polymerization of EDOT in the presence of: (top) LiClO₄ or (center) PSMA-binding phage, and (bottom) PSMA-binding phage and exposure to the wrapper KCS-1 (Green), c). Schematic diagram of the biosensing experiment. (d) $\Delta R/R_0$ of the film increases with the PSMA concentration. (e) Comparison of PSMA detection in synthetic urine (green) with detection in PBF buffer (purple).20

Figure 1.5 The Two-Sided Biosensor: A Monolithic Biosensor for Human Serum Albumin (HSA). a). Engineering diagram of two electrode virus-PEDOT biosensor. b,c) Nyquist plots (Z_{im} vs. Z_{re}) for a control protein (BSA) and HSA. d). Signal-to-noise versus frequency plot for HSA and BSA. e). ΔR_{re} versus HSA concentration calibration curve. Controls for BSA, and off-virus binding also shown.....23

Figure 2.1 The Virus BioResistor (VBR). a) Schematic diagram of a VBR showing critical components and dimensions. b) A buffered salt solution alters the solution resistance, R_{soln}, but not the resistance of the VBR channel, R_{VBR}. c) In the presence of a target protein (HSA in this case), R_{VBR} is increased, enabling determination of its concentration.27

Figure 2.2 Process flow for the four-step VBR fabrication process, including the process windows that were enforced for this process, indicated in red.....30

Figure 2.3 VBR biosensor fabrication. a) Two pairs of gold-electrodes from which two VBRs are prepared. The gold electrodes have width of 2 mm and their separation of 1.5 mm defines the channel length of these devices. The two pairs of gold electrodes are separated by 0.5 mm. b) A layer of PEDOT:PSS is spin-coated onto the gold-electrode device and baked for 1 h at 90 °C. c) A 2 mm x 2 mm PMMA cell is attached defining the area of the bioaffinity layer. d) A virus-PEDOT top layer is electropolymerized on top of the PEDOT-PSS bottom layer by using $\approx 100 \mu\text{L}$ of plating solution and applying two oxidizing voltammetric scans. e) The virus-PEDOT plating solution is removed, and the cell is rinsed. Electrodes are used to enable impedance measurements at each of the two VBR sensors. One background impedance measurement is acquired in buffer, and a second in a solution containing added HSA. The calculated ΔR_{VBR} is used to determine the HSA concentration in this sample with reference to a calibration curve.32

Figure 2.4 Electrodeposition and SEM/AFM characterization of virus-PEDOT bioaffinity layers. (a) Electrodeposition of a virus-PEDOT film on a PEDOT-PSS film using cyclic voltammetry (50 mV/s). The virus-PEDOT top layer is prepared by two cycles from an aqueous virus-EDOT solution containing 2.5 mM EDOT, 12.5 mM LiClO₄, and 8 nM HSA phage. (b) cross sectional scanning electron microscopy (SEM) image of a PEDOT-PSS/virus-PEDOT film. The PEDOT-PSS bottom layer and virus-PEDOT top layer can be distinguished.

(c) Plan view SEM image of a PEDOT only film (no virus) prepared by two consecutive cycles of deposition in aqueous EDOT solution containing 2.5 mM EDOT, 12.5 mM LiClO₄. (d) Plan view SEM image of a virus-PEDOT film prepared as described in (a). (e, f, g, h) Atomic force microscopy (AFM) images of PEDOT films (e, g) and virus-PEDOT films (f, h). The same AFM image data are represented in two ways: (e, f) shows height versus position data while (g, h) show a three-dimensional rendering of these the same data shown in (e, f). The rms roughness for PEDOT and virus-PEDOT films are ≈ 5 nm and ≈ 10 nm, respectively.....34

Figure 2.5 Orthogonal measurement of R_{soln} and $RVBR$ using a VBR biosensor. Nyquist plots summarizing the impedance response of VBRs from 1 Hz to 10 kHz with equivalent circuit fits (red traces). (a,b,c) VBRs in solutions of run buffer of: a). 1x PBS (purple), b). 2.5x PBS (yellow), c). 5x PBS (green), before and after exposure to 75 nM HSA in the same buffer. (d,e). Plots of R_{soln} and $RVBR$ as a function of buffer concentration extracted from the data of a,b, and c. Shown are the values of these two circuit elements in pure buffer, and in buffer with added 75 nM HSA, as indicated. (f,g,h) Experiment in which the HSA concentration is increased from 0 nM (1x PBS) to 750 nM (in 1x PBS) showing the invariance of R_{soln} and the linear increase in $RVBR$37

Figure 2.6 Calibration plots for 20 VBRs exposed to HSA concentrations 7.5 nM – 900 nM generated by two methods (5a) sensing signal ΔZ_{re} , measured at 5 Hz, versus concentration (5b) sensing signal defined as $\Delta RVBR$, versus concentration. At each of seven concentration points, three data point for three different VBR sensors are plotted here with error bars defined as the standard deviation, $\pm 1\sigma$. The exception is the 900 nM concentration point where just two sensors were used, and two data points are shown. It should be noted that these three data points are not all seen at all concentrations, since some are superimposed on others. Impedance data for HSA exposed to virus-PEDOT films containing HSA phage is fitted to the hill equation (red line). c) compares the CoV% for the signals from two methods obtained by the variation in signal generated by three devices exposed to concentrations [HSA] = 7.5 nM - 900 nM.40

Figure 2.7 VBR specificity and speed. a). A specificity assay. Blue bars represent three VBRs with PEDOT films containing HSA binding phage exposed to 750 nM HSA; Red bars show the response to a 750 nM BSA solution of three VBRs containing HSA binding phage; Green bars show the response to a 750 nM HSA solution for three VBRs containing STOP4 phage that have no affinity for HSA. b). Real time VBR sensing data. Responses for three VBR sensors are shown for [HSA] exposures of 220, 370, and 600 nM that show response times of 30 s, 3 s, and 3 s, respectively. The specificity assay summarized in (a) are also repeated here, in real-time sensing format, again showing no measurable responses.....42

Figure 3.1 Two ELISAs for M13 phage binding of DJ-1: a) Phage ELISA of the DJ-1-binding phage DL-1 and a negative control Stop4 phage. Here, DJ-1 is immobilized and the DL-1 phage is detected. The data were fit with a four-parameter logistic curve fit ($R^2 = 0.9230$). Measurements were performed in triplicate; error bars represent the standard deviation of the mean. b) Sandwich ELISA of DJ-1. In this case, DL-1 phage (or the control Stop4 phage) are immobilized and the DJ-1 protein is detected. This format mimics the function of the VBR. The data were fit as described above ($R^2 = 0.9944$). Measurements were performed in triplicate; error bars represent the standard deviation of the mean.....47

Figure 3.2 The Virus BioResistor (VBR). a) Rendering of gold electrodes for a two-VBR chip showing its dimensions. The two electrodes at left comprise one VBR and the two on the right a second VBR. These two VBRs will share a single bioaffinity layer. b) The three-step process for fabricating a VBR: Step 1 – a conductive PEDOT-PSS base layer is spin-coated onto the gold-on-glass template shown in (a). This film is baked at 90 °C for 60 min; Step 2 – A poly(methylmethacrylate)(PMMA) cell is attached on top of the dried PEDOT-PSS film; Step 3 – the PMMA cell is filled with aqueous EDOT-virus plating solution, and a virus-PEDOT film is deposited by electrooxidation. This VBR biosensor is ready for use. c) Photograph of a two-VBR chip with PMMA solution cell.....51

Figure 3.3 Electrodeposition and SEM cross-sections of virus-PEDOT bioaffinity layers. a). A virus-PEDOT bioaffinity layer is electrodeposited on a PEDOT-PSS base layer using two voltametric scans, as shown. The plating solution is aqueous 2.5 mM EDOT and 12.5 mM LiClO₄, 8 nM virus, and the scan rate is 20 mV/s. The DC resistance, R_{PEDOT-PSS}, of the PEDOT-PSS layer here is 75 – 79 Ω. b). Same electrodeposition process for a thinner, PEDOT-PSS base layer with R_{PEDOT-PSS} in the range from 240 – 380 Ω. c,d). Cross-sectional SEM images of these two layers show that the more conductive PEDOT-PSS layer (R_{PEDOT-PSS} = 75 – 79 Ω) is 70 nm (± 3 nm) in thickness whereas the less conductive PEDOT-PSS layer is 48 nm (± 2 nm) in thickness. The electrodeposited virus-PEDOT layer is also somewhat thinner in (d) relative to (c) in accordance with the lower deposition currents observed for the second deposition scan.....53

Figure 3.4 Plan-view SEM images, acquired with secondary electron detection (SED), of virus-free (a,b) and virus-containing (c,d,e) bioaffinity layers. (a,b) Control VBR bioaffinity layer prepared by electrodeposition from a solution containing no virus particles. Micron scale protrusions from the surface of this film are characteristic of electrodeposited PEDOT. These protrusions are not seen at PEDOT-PSS films prepared by spin-coating. We refer to these structures as “PEDOT stalagmites”. (c,d,e) VBR bioaffinity layers containing M13 virus particles. Filamentous M13 virus particles comprise the dark regions of these images. Lighter gray regions contain no virus. PEDOT stalagmites are also observed. Enhanced contrast (e) exposes tangles of M13, again distributed nonuniformly inside a virus-PEDOT bioaffinity layer.....55

Figure 3.5 The VBR equivalent circuit (a) and a typical impedance response (b). This Nyquist plot (Z_{im} versus Z_{re}) shows the impedance frequency spectrum plotted between 1.0 Hz and 40 kHz for a synthetic urine solution that was supplemented with DJ-1. A single VBR measured these solutions at the indicated DJ-1 concentrations.58

Figure 3.6 RPEDOT-PSS tuning of the VBR sensitivity for HSA. (a). The equivalent circuit for the VBR places the electrical impedance of the virus-PEDOT layer, RVBR, in parallel with that of the PEDOT-PSS bottom layer, RPEDOT-PSS, forming a current divider. (b) Increasing RPEDOT-PSS from 80 Ω to 300 Ω , by reducing the PEDOT-PSS layer thickness, forces current, i , through the virus-PEDOT measurement layer, increasing the signal for 100 nM HSA by a factor of 3 to 5 from 200 Ω to more than 900 Ω . (c,d,e) Three Nyquist plots corresponding to three values of the resistor, RPEDOT-PSS, as indicated. In each plot, impedances are plotted in the complex plane from 1 Hz (right) to 40 kHz (left). A shift in the low frequency Z_{re} from synthetic urine only (blue trace) to 100 nM DJ-1 (orange trace) approximates the signal, $\Delta RVBR$. (f) RVBR versus [HSA] calibration plots for a series of 42 VBR sensors (21 in each plot) with RPEDOT-PSS values in the range from 80 to 100 Ω and 260 to 300 Ω . The higher RPEDOT-PSS devices produce 3 to 5 times more signal amplitude across the HSA binding curve.61

Figure 3.7 RPEDOT-PSS tuning of the VBR sensitivity for DJ-1. (a) Increasing RPEDOT-PSS from 80 Ω to 300 Ω , by reducing the PEDOT-PSS layer thickness increases the signal for 100 nM DJ-1 by a factor of ≈ 10 from 50 Ω to 550 Ω . (b, c, d) Three Nyquist plots corresponding to three values of the resistor, RPEDOT-PSS, as indicated. In each plot, impedances are plotted in the complex plane from 1 Hz (right) to 40 kHz (left). A shift in the low frequency Z_{re} from synthetic urine only (blue trace) to 100 nM DJ-1 (green trace) approximates the signal, $\Delta RVBR$62

Figure 3.8 DJ-1 sensing performance using VBRs with RPEDOT-PSS = 280 to 300 Ω . (a, b, c) Nyquist plots for three DJ-1 concentrations of (a) 10 pM, (b) 1 nM, and (c) 300 nM. Also shown (blue traces) are background Nyquist responses in synthetic urine only. (d) A calibration curve for the detection of DJ-1 using the RVBR signal constructed using 21 individual measurements from the same number of VBRs, at seven concentrations. Values of K_D and h (the Hill exponent) obtained from a best fit of the experimental data to equation (2), are indicated. (e) Bar plot for $\Delta RVBR$ measurements acquired from 21 electrodes, illustrating the sensor-to-sensor reproducibility of these data. CoVs for these data, shown, are in the 2 to 8% range across four orders of magnitude in DJ-1 concentration. The values of each of the circuit elements is indicated in Table 3.2.63

Figure 3.9 VBR specificity and speed. (a) Three control experiments: At left is the response of three VBRs prepared with no phage exposed to 500 nM DJ-1. To the right of this is the

response of three VBRs prepared with Stop-4 phage that has no displayed peptides on its surface. Finally, at right are shown the results of three VBRs containing DL1 phage (selected for the binding to DJ-1) upon exposure to IL-6, a protein of similar MW (20.9 kDa) and pI (6.2) to DJ-1 (20.7 kDa and pI of 6.7, respectively). (b) Real-time VBR sensing data. Responses for five VBR sensors are shown for DJ-1 exposures of 0 pM (green trace), 10 pM, 30 pM, 100 pM, and 1.0 nM. These traces were obtained by first stabilizing sensors in synthetic urine for 9 min, measuring a RVBR baseline at 0.10 Hz, and then interrupting for 1.0 min while the synthetic urine was replaced with synthetic urine supplemented with DJ-1 at the specified concentration, after which Δ RVBR signal was acquired.....66

Figure 3.10 (a) Signal-to-noise (S/N) versus frequency for the detection of DJ-1. Shown are three plots of S/N versus frequency measured for three VBRs immersed in three DJ-1-spiked synthetic urine solutions containing DJ-1 at the indicated concentrations. Noise is calculated as the standard deviation of three replicate measurements at each frequency. S/N consistently increases from high to low frequencies. (b) Comparison of Δ RVBR for the detection of DJ-1 in two electrolytes: synthetic urine (pH = 5.5) and PBS buffer (pH = 8.0). The charge state of DJ-1 (pI = 6.7) inverts across this pH difference, and is negatively charged at pH = 8.0 and positively charged at pH = 5.5. However, Δ RVBR at two different concentrations are the same, despite changes in pH, within the reproducibility of these measurements.....67

Figure 3.11 Schematic representation of a hypothesized signal transduction mechanism for the VBR. (a) The virus-PEDOT layer shown here consists of semi-crystalline PEDOT with virus particles that are concentrated within disordered regions of the PEDOT layer, (b) When exposed to the DJ-1 protein solution, Δ RVBR is initially zero, because an induction time is associated with the rate-limiting diffusion of the protein into the virus-PEDOT layer. (c) Permeation of the virus-PEDOT layer by DJ-1 is associated with an increase in its resistance as the insulating protein interferes with conduction pathways within this layer. 71

Figure 3.12 Measurement of DJ-1 mass loading for VBR bioaffinity layers using quartz crystal microbalance (QCM) gravimetry. (a) Four step fabrication of a complete VBR bioaffinity layer on a commercial QCM crystal. (b) Change in frequency, Δ f, versus time for the exposure of two VBRs to solutions of DJ-1 at 100 pM and 100 nM. The measured DJ-1 mass loading is indicated, and traces are shifted along the Δ f axis for clarity. (c) The concentration of DJ-1 versus its measured mass loading. This isotherm was acquired in PBS buffer solution..... 73

Figure 4.1 Fabrication of VBR (a) Schematic cartoon of VBR fabrication. The regular film fabrication follows the procedure mentioned in section A.2. Thereafter, the cell is filled with 12.5 mM LiClO₄ solution and oxidized. The oxidized film appears transparent as compared

to the regular PEDOT film. Images of regular VBR and oxidized VBR are placed right below their respective cartoons. (b) Chronoamperometric method of oxidation holds the potential 0.8 V vs MSE for different time points, example for 50 seconds (CA50) and 100 seconds CA100, depicted in the figure. (c) Potentiodynamic method involves sweeping the potential from 0.2 to 1 V vs MSE for two cycles at 20 mV/s.87

Figure 4.2 The Nyquist plots for oxidized films. The overall effect of oxidation can be recognized as increased resistance of the bioaffinity films. Each film tested contains the virus particles to include the effect of uneven surface that results from virus loading (a) Increased resistance is depicted from regular VBR. Higher the time limit for oxidation, higher is the resistance. (b) The baseline Nyquist for 7 devices is presented. The loss of semi-circle is accounted for stripping of bioaffinity layer from the gold electrode. (c) The higher success rate obtained for CA oxidation for 50 and 100 seconds. 10 out of 11 devices tested retained their semi-circle and the films didn't delaminate.89

Figure 4.3 (a) Comparing signals for 100 nM DJ1 from regular and oxidized VBR for 4 different concentrations. The signals were averaged from three devices, the error bars represent the standard deviation for three devices. (b) Highest signals from three control sensors were compared with the highest background obtained for oxidized sensors. The orange bar stacked upon green bar is the extra background signal generated for the oxidized VBR. (c) Plan view SEM for sputtered sample of regular PEDOT film. The surface appears to be smooth compared to (d) oxidized VBR, wherein pores are visible, and surface appears to be rough. (e) A magnified image of oxidized film. Oxidized films retain the PEDOT stalagmites from the regular film without any significant change of structure.90

Figure 4.4 Plan view SEM for (a) oxidized PEDOT films without virus particles incorporated (b) Oxidized PEDOT:virus films at the same magnification as (a), confirming the presence of dense phage particles that remain on the film despite oxidation treatment. This clarifies that phage loading remains unaffected during the treatment. The non-uniform distribution of the virus particles is evident in this image (c) magnified image of PEDOT:virus film.....92

Figure 4.5 Detection of Anti-FLAG antibody with C2 phage loaded sensors. (a, b) Nyquist plots for a low concentration and high concentration anti-FLAG. Plots were obtained after 20-minute incubation in PBS for baseline measurement (purple) and 20-minute incubation of anti-FLAG (green) spiked in PBS. (c) Bar plot displaying signals imparted by 20 individual sensors. The CoVs lower than 13% assure that oxidation doesn't affect the reproducibility of the sensor. (d) Oxidized VBR specificity towards anti-FLAG detection for four control experiments. (e) Calibration plot fit to the Hill equation. The green dots display the signals generated by regular VBR in response to anti-FLAG.....95

Figure 4.6 Serum measurements for individual devices. The high variability depicted can affect reliable antibody measurements.....96

LIST OF TABLES

Table 2.1 Equivalent circuits and equations representing the electrical response of a VBR biosensor.....	35
Table 3.1 VBR circuit element values, and $\Delta RVBR$, corresponding to the Nyquist plots of Figure 3.5b.....	59
Table 3.2 VBR circuit elemental values corresponding to the Nyquist plots of Figure 3.8a-c.....	64
Table 4.1 Electrochemical immunosensors for antibody detection.....	82

ACKNOWLEDGEMENTS

I would like to thank my advisor, Dr. Reginald Penner for giving me the opportunity to work on such a wonderful project. The experience is very valuable and will remain the most prized asset. I am thankful to my committee members, Dr. Andrej Luptak and Dr. Shane Ardo for taking interest in my work and guiding me with their expertise. This work wouldn't have been possible without the contribution from Dr. Gregory Weiss and his team, Sudipta Majumdar, Emily Sanders, Jason Garrido, Alicia Santos and Sanjana Sen. This work has been equally supported by phageteq team Philip Tam, Jeffrey Briggs, Marie True. It has been pleasure working with the group and learning about the biochemistry counterpart of the project.

PhD labwork is very challenging, and I am lucky to have shared my workspace with awesome lab-mates Shaopeng Qiao, Alana Ogata, Josh Ziegler, Vivian Chen, Eric Choi, Ilektra Andoni, Nick Drago, and Valen Yoon. They made the workplace fun and welcoming.

This work has been supported by National Science Foundation; National Cancer Institute of the NIH (1R33CA206955-01), PhageTech Inc; Chao Family Comprehensive Cancer Center, UC Irvine. FE-SEM data were acquired using the instrumentation of the LEXI (lexi.eng.uci.edu/) and IMRI (ps.uci.edu/imri/) facilities at UCI. I thank the healthy urine donors who consented to have their urine used in this study through UCI clinical protocol IRB HS# 2014-1758.

CURRICULUM VITA

Apurva Bhasin

August 30, 2020

EDUCATION

Doctor of Philosophy in Chemistry

University of California, Irvine

2020

Irvine, California, USA

B.Sc. HONORS: Chemistry

Institute for Excellence in Higher Education

2012

Bhopal, Madhya Pradesh, India

M.Sc.: Chemistry

Institute for Excellence in Higher Education

2014

Bhopal, Madhya Pradesh, India

RESEARCH EXPERIENCE

Graduate Research Assistant

University of California, Irvine

2016 -2020

Irvine, California, USA

Research Assistant

Amity University Noida

2014-2016

Noida, Uttar Pradesh, India

Research Intern

Nirma University

2014

Ahmedabad, Gujrat, India

Publication(s)

1. The Virus Bioresistor: Wiring Virus Particles for the Direct, Label-Free Detection of Target Proteins. *Nano Lett.* 2018, 18, 3623–3629.
2. A Virus BioResistor (VBR) for Bladder Cancer Detection: Dip-and-Read Detection of DJ-1 in Urine at 10 pM in One Minute. (Submitted)

Patent(s)

- Invention title "Virus Bioresistors". Application number: PCT/US19/24939

ABSTRACT OF THE DISSERTATION

Development and optimization of the Virus-Bioresistor: A potential Point-of-care diagnostic platform

by

Apurva Bhasin

Doctor of Philosophy in Chemistry

University of California, Irvine, 2020

Professor Reginald M. Penner, Chair

Point of Care (PoC) diagnostics have made healthcare available for a large audience of non-specialists and patients with introduction of miniaturized, simple and user-friendly electronic devices. Electrochemical biosensors have emerged victorious candidates for PoC owing to the ease of transforming a biological interaction to simple electrical signal. This work is dedicated towards exploring a sensor architecture that connects the biological sensing element, virus, to an external circuitry at nanometer scale. Chapter 2 introduces the Virus-bioresistor in detail. It is demonstrated that M13 phage particles can be wired into an electrical circuit by embedding them in an electronically conductive polymer composed of poly(3,4-ethylenedioxythiophene) or PEDOT via electropolymerization. The signals transduced by impedance spectroscopy are recorded as an increased resistance of the virus-PEDOT material in the presence of the target protein and the amplitude of the resistance change allows its concentration in the contacting solution to be measured. This concept is

demonstrated on a model system in which a dynamic range of 7.5 nM – 900 nM human serum albumin (HSA, 66kDa) is detected in phosphate buffer solution. The VBR overcomes the challenges of label-free, non-faradaic sensors pertaining to non-specific adsorption and lower sensitivity. Elemental problem of coupling of target binding from ionic conduction is solved as an equivalent circuit description for the data procured, establishes signal independence over solution conductivity. The next segment employs the VBR for detection of bladder cancer biomarker, DJ-1 (20 kDa), which is achieved by engineering the sensing layer that enables successful pico-molar detection of analyte without compromising on the speed and reproducibility of detection. A range of 10 pM – 300 nM DJ-1 protein is detected, which beautifully accommodates the established 100-1000 pM DJ-1 detected in bladder cancer patient's urine. A possible signal transduction mechanism is uncovered with experiments based on quartz crystal microbalance (QCM) gravimetry. The last section exploits the potentiality of the VBR to be modified in a controlled fashion to enable large biomolecule (antibody) sensing. This is achieved by oxidizing the VBR channel using chronoamperometry. The morphological changes for VBRs have been tracked with microscopy techniques. Overall, this work establishes that VBRs can be associated with speed, specificity and reproducibility with coefficient of variation values <16%. The signal output can be tuned as per convenience to detect biomolecules with molecular weights that fall within an appreciable range of 20 kDa to 150 kDa.

Chapter 1

Introduction

A major portion of this chapter is adapted from a research article "Viruses Masquerading as Antibodies in Biosensors: The Development of the Virus BioResistor" submitted to Accounts of Chemical Research.

The diagnostic industry has come a long way from specialized testing limited to hospitals and pathology labs to the ambitious “at-home diagnosis” with an exciting journey ahead to ease the diagnosis of many chronic diseases including the infamous cancer. It has found motivation in the growing prevalence of chronic diseases and the expense associated with the diagnostic, limiting access to a large population in need. So, what holds the major share of attention for PoC devices? Undoubtedly, electrochemical biosensors are amongst trending research over past few years. The idea of marrying point of care systems with electrochemical transducers has demonstrated a great potential for rapid, simple and cost-effective on-site healthcare. The first ever glucose sensor is the most successful example in this field. The glucose test strip is based on enzyme modified-screen printed electrodes, coupled to an amperometric transducer. This field has been applauded by micro and nano-scale fabrication technology, not limited to sensor design itself, but extending to miniaturization of complex potentiostat measurements that can be now, performed on a cellphone. Publications and research work in this field have constantly tried to overcome challenges like specificity, reproducibility, low cost, simplicity of the instrumentation operation. These sensors are designed focusing on new materials and strategies to ultimately grow into a point of care system. It is beyond the scope of this dissertation to explore the rich literature on electrochemical sensors but a few sensing platform and strategies in their proof-of-concept stage will be discussed.

1.1 Nanomaterials involved in biosensor construction

Five features govern the development and construction of a biosensor:

- a. Technology and material employed for sensor fabrication
- b. The working principle of the transducer
- c. The parameter detected upon binding event
- d. The chemical/biochemical principle involved for entrapment and detection
- e. The field of application

The essence of the biosensor is the material used for the electrode and supporting substrate. These materials are expected to be chemically stable and conductive, while exhibiting low currents in electrolyte solution. Platinum, gold, carbon, silicon, metal oxides (indium tin oxide ITO) are frequently used electrode materials in biosensors. Surface modification of the electrode greatly affects the sensing capability of the final sensor. High surface to volume ratio of nano-objects makes their electrical properties increasingly susceptible to external influences. Since nanometer size of these objects is comparable to the size of the target biomolecules, higher measurement sensitivity may result.¹

Nanomaterials involved in biosensor construction can be multipurpose in nature, employed for electrode construction or modification and for immobilization of bioelements. The nanomaterials are commonly categorized as carbon and non-carbon based materials. The carbon-based nanomaterials are a popular choice for electrode material (screen-printed electrode, glassy carbon electrode) and substrate material (carbon nanotubes, nanofibers), owing to their reduced manufacturing cost, easy large-scale production and disposability. Biosensors based on carbon nanotube CNT,^{2,3,4,5,6} graphene,^{7,8} graphene oxide nanoplatelets⁹ and carbon nanoparticles.¹⁰

Non-carbon based materials include conducting polymers, magnetic nanoparticles,¹¹ semiconductor quantum dots,¹² ferrocenyl terminated dendrimers,¹³ hydrogel,¹⁴ aptamers and molecular-imprinted electrodes¹⁵ among a plethora of options. Hybrid materials are often used to enhance sensitivity or biomolecule attachment. Examples of sensors based on hybrid material include; AuNP tagged graphene oxide ¹⁶ and AuNP in Dendrimer,¹⁷ etc.

1.2 Transduction principles and strategies for signal generation

Electrochemical sensors can be based on transduction principles of amperometry, potentiometry, conductometry, chronoamperometry, electrochemical impedance spectroscopy (EIS), field effect transistors (FET).

Amperometric devices focus on recording current generated in a biosensor system as a result of oxidation or reduction of electroactive species.¹⁸ Amperometry measures current at a constant potential whereas voltammetry measures current while potential is tuned in a controlled fashion. The value of current recorded is a function of the concentration of the analyte/electroactive species generated during biosensing event. Such devices use mediators to accomplish sensing, since not all analytes can intrinsically serve as redox partners in electrochemical reaction.¹⁹ Besides the extensively used cyclic voltammetry technique, chronoamperometry studies the current alterations resulting from the expansion or reduction of the diffusion layer.²⁰

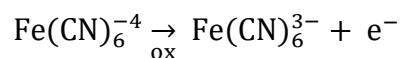
Potentiometric devices take advantage of the charge accumulated on the working electrode surface versus a reference electrode when no significant current flows between them. Such sensors make use of ion selective electrodes to convert biological reactions to

electrical signals. Biosensors based on biologically coupled ion-sensitive field effect sensors are the most valued candidates in potentiometric biosensing.²¹

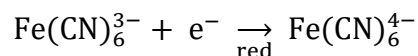
Impedimetric sensors, rely on applying a small sinusoidally varying potential and recording the current response. This potential is applied at varied frequencies to enable analysis of complex impedance constituting the electrical resistance (real component) and capacitive reactance (imaginary component). These sensors monitor changes induced at the surface of modified electrode as a consequence of biorecognition event.^{22,23}

Field-effect transistors use electric field to alter the conductivity of a semiconducting channel between two electrodes, known as source and drain. In biosensors this channel is made up of biochemically sensitive surface. ISFET (ion-selective FET) and En(FET) are more valuable to biosensing applications.^{24,25} Other techniques and nanomaterials have been extensively discussed in the following reviews.^{1,26,18,27}

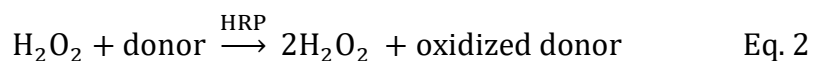
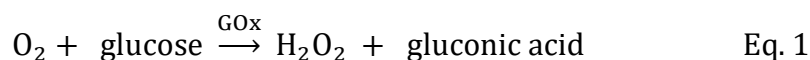
Strategies for signal enhancement or sensitivity enhancement include use of redox mediators or techniques that involve DNA hybridization. DNA hybridization biosensors rely on the conversion of the DNA base pair recognition event into a useful electrical signal. An electroactive indicator that selectively binds to DNA duplex is detected as an increased current signal.²⁸ Soluble redox probes like $\text{Fe}(\text{CN})_6^{4-/3-}$ or $\text{Ru}(\text{NH})_3^{2+/3+}$ are integral to increasing sensitivity and signal for most amperometric and aptasensors. The potential at the working electrode (WE) is controlled vs a reference electrode (RE), example $\text{Ag}/\text{AgCl}(\text{s})/(\text{satd. KCl})$ electrode. The controlling potential that is applied across the WE and the auxiliary electrodes is the excitation signal. As sufficiently positive potential is applied to oxidize $\text{Fe}(\text{CN})_6^{-4}$, the anodic current results from the following reaction at electrode:



As the scan direction is switched to negative, and the electrode becomes a sufficiently strong reductant, Fe(CN)_6^{3-} , which has been forming adjacent to the electrode surface, will be reduced by the electrode process, resulting in a cathodic current from the equation:



This chemistry is employed in biosensors wherein the access of redox couple to electrode is restricted as the analyte of interest binds to the biorecognition element affixed on the electrode surface. Although this strategy is attractive to demonstrate a sensor in its proof of concept, it is fairly unattractive as a portable tool for PoC as it adds to complexity to use an extra solution within redox probe. The alternative approach uses enzyme labels enzyme labels horseradish peroxidase (HRP), glucose oxidase, alkaline phosphatase used as mediators²⁹ The surface immobilized enzyme selectively catalyzes the transformation of specific substrate.³⁰ This approach, however, decreases the lifetime of the sensors, due to instability of such molecules. Reaction schemes are given in equation 1 for GOx and equation 2 for HRP. Donors for the reaction with HRP are molecules such as phenols, aromatic amines, or iodide. Other, less commonly used enzymes comprise beta-lactamase,³¹ urea and urease.¹⁰



Methylene Blue and ferrocene are amongst the redox probe that offer higher stability. Their operation principle relies on electron transfer rate which varies according to the distance of the label from the electrode.²⁷ An interesting biosensor was fabricated for microRNA

quantification based on electrically reconfigurable DNA-Au@MNP (gold coated magnetic nanoparticles) network. With the help of methylene blue redox label, the difference between non-hybridized and target captured hybridized DNA-Au@MNP could be electrochemically quantified. The formation of double helix on Au@MNP surface increases the space between the network, suppressing the current.³²

1.3 The Virus bio-resistor and quest for cancer detection

In 2020, the most reliable techniques used by doctors for cancer surveillance are identical to practices from twenty years ago: colonoscopy (colon cancer), mammogram (breast cancer), and Pap smear (cervical cancer). Cancer surveillance involving the analysis of blood and urine for cancer markers – so called liquid biopsies - are not part of an annual physical examination for most Americans because biosensors and laboratory assays that facilitate rapid, reliable, and affordable analyses of these fluids for cancer markers do not yet exist. The success of the glucose meter has inspired development of biosensors for POC electrochemical devices that can be used for cancer detection. This dissertation work is based on exploring a potential candidate for PoC device. The virus bio-resistor (VBR), is virus enabled impedance transduced sensor that increases its electrical resistance upon sensing analyte.

1.4 Phage display for customized affinity and specificity

Until 2005,³³ most biosensors designed to detect the distinctive protein “biomarkers” produced by cancers used antibodies to recognize and bind these proteins. Owing to their

wide availability and robustness among other factors, antibodies have ruled the sensor industry being the no. 1 choice for biorecognition element. An alternative emerged, when some laboratories embedded whole virus particles like M13 bacteriophage in the bioaffinity matrix within biosensors. The basic approach for the “display” of proteins on the M13 phage surface was invented by George Smith in 1985,^{34,35} before Jim Wells and co-workers introduced key and necessary improvements to enable Greg Winter to display an antibody, or Fv, on the phage surface.^{36,37} M13, a filamentous bacteriophage that infects Ecoli, was engineered to “display” Fv antibody fragments on their surfaces providing an intriguing opportunity for the development of cheaper, more robust biosensors. A typical M13 phage includes a viral capsid tube for the viral DNA with an outer diameter of 6 nm, composed principally of 2700 copies of P8, the major coat protein. The N-terminus of the 50 amino acid P8 is exposed to the outside of the virus. Its C-terminus is buried within the core of the capsid, where the P8 sequence provides several lysine residues for packaging the negatively charged viral DNA. The cylindrical virus, 1.0 μm long, is capped at one end by five copies of each of the minor coat proteins P3 and P6 and at the other end by the coat proteins P7 and P9.³⁸ M13 viruses are an attractive alternative to antibodies in biosensors for three main reasons: 1) the cost of engineered viruses is much lower, 2) the affinity of virus particles is similar (often dissociation constants, K_D , are below 10^{-9} M), and, 3) virus particles are quite robust, and, for example, do not require refrigeration to maintain potency. In principle, biosensors based upon virus particles could be cheaper to manufacture and cheaper to distribute and store, especially in the resource-challenged third world.

1.5 Biosensor journey preceding VBR in Penner Group

The VBR is the result of a fourteen-year quest to accomplish, virus-based sensors that are miniaturized, label-free, rapid (60 s), with impressive limit of detection. The following sections trace the development of VBR from 2005 to 2017.

1.5.1 A Covalent Virus Layer (CVL)

A generic biosensor has three components: i) A *bioaffinity layer* equipped with receptors, such as ss-DNA probes or antibodies to recognize and to bind a target DNA or protein, respectively, ii) a *transducer* that detects the binding of the target to the bioaffinity layer using a measurement of properties such as the mass of this layer, or its optical or electrical response, and, iii) *electronics* that convert the transducer signal into an estimate of the concentration of the target. Bioaffinity layers for the detection of proteins have often exploited monolayers of antibodies conjugated to polymer or glass surfaces.³⁹

Early biosensors to exploit the Nobel Prize-winning phage-display technologies^{36,37,34,35} were demonstrated in 2003 by a team at Auburn University lead by Valery Petrenko and Vitaly Vodyanoy.⁴⁰ In that work, M13 virus particles were immobilized by physisorption onto the surface of an acoustic wave sensor and used to measure the dose-dependent binding of β -galactosidase, a 465 kDa protein, at concentrations down to 0.60 nM.⁴⁰ These experiments provided the first proof-of-concept that viruses could function as receptors in biosensors. However, problems were encountered with the stability of the adsorbed virus layer⁴⁰⁻⁴² which was insufficient, compromising the reproducibility of the measurements.

Li-Mei Yang, working with Juan Diaz and Phillip Tam, attempted to remedy the stability problem by preparing monolayers of M13 virus particles that were covalently bonded to a modified gold electrode surfaces (Figure 1.1).^{43,44} Yang accomplished this by first electrochemically roughening a gold electrode, before exposing it to thioctyl NHS ester to form a thiol–Au bonded self-assembled monolayer or SAM, then treating the SAM with a

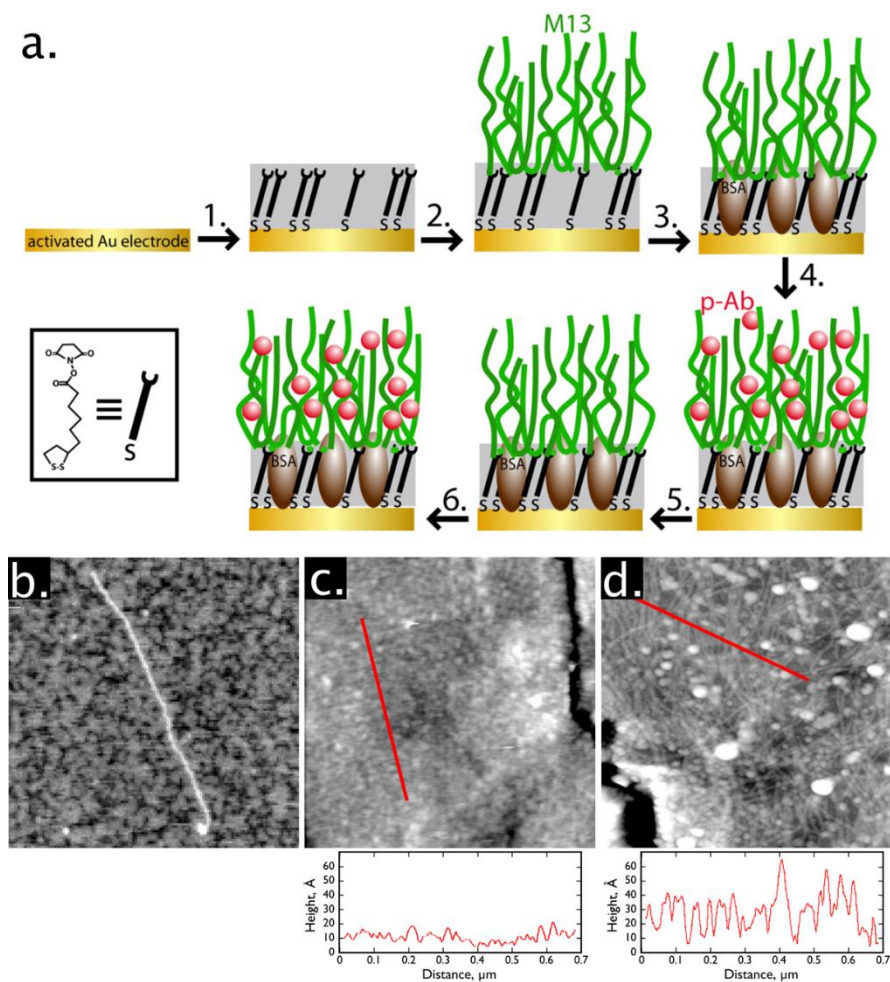


Figure 1.1 The covalent virus surface (CVS). a). Stepwise assembly (steps 1–3) and functionalization (steps 4–6) of the CVS. (b–d) Noncontact mode AFM images ($1\ \mu\text{m} \times 1\ \mu\text{m}$). (b) A single M13 virion on mica, (c) A self-assembled monolayer (SAM) of N-hydroxysuccinimide thioctic ester on gold after exposure to BSA. No virus particles were attached to this surface. The dark fissure at upper right is a grain boundary. (d) A functional CVS consisting of a SAM of N-hydroxysuccinimide thioctic ester (NHS-TE) on polycrystalline gold,

reacted first with M13 to produce covalent attachment, and then exposed to BSA (Figure 1.1, step 3).

suspension of virus particles thereby forming a covalent amide bond between free amines on the phage coat peptide and the activated carboxylate at the surface of the SAM. The final step was to plug any defects in this “covalent virus layer” (CVL) with bovine serum albumin (BSA) to minimize nonspecific adsorption (Figure 1.1.a, step 3).

Atomic force microscopy (AFM)^{43,44} showed that the CVL consists of a close-packed monolayer of filamentous M13 virus particles, one of which is shown in Figure 1.1.b. When many M13 virus are covalently bound to a surface, the densely packed “monolayer” of the virus resembles a shag carpet (Figure 1.1.a). The resulting CVL retains significant free volume as evidenced by the fact that each phage particle is capable of binding 140 antibodies to the p8 majority coat peptide (p8-Ab, 148 kDa) at saturation, on average.⁴³ In the vacuum of a scanning electron microscope (SEM), the water and ions supporting the shag carpet are removed and filamentous virus particles collapsed onto the surface can be clearly seen (Figure 1.1d).

1.5.2 Mass-Based Signal Transduction of the CVL

The properties of the CVL for biosensing were first explored in 2008. Both mass based biosensing,⁴³ conducted by depositing the CVL on a gold quartz-crystal microbalance (QCM) transducer, and electrochemically-based sensing⁴⁴ were evaluated. In these experiments, the response of a CVL-modified gold surface to p8-Ab was studied.^{43,44}

To measure the mass responses of a CVL during exposure of p8-Ab, the QCM crystal was mounted in a Teflon flow cell that provided for the radially symmetric delivery of

solution to the circular QCM electrode surface (Figure 1.2.a,b).⁴³ The increase in mass observed upon p8-Ab exposure ($\approx 3 \mu\text{g}/\text{cm}^2$) could be reversed by washing briefly with aq. 0.50 M HCl, (Figure 1.2.c), enabling mass *versus* [p-Ab] calibration data to be acquired over a wide range of [p-Ab] for a single CVL (Figure 1.2.d-f). These data were linear from 6.6 nM to 200 nM p-Ab.⁴³ A non-binding antibody (n-Ab) control showed negligible non-specific signal over this concentration range, establishing the limit-of-detection for p8-Ab as 20 nM.

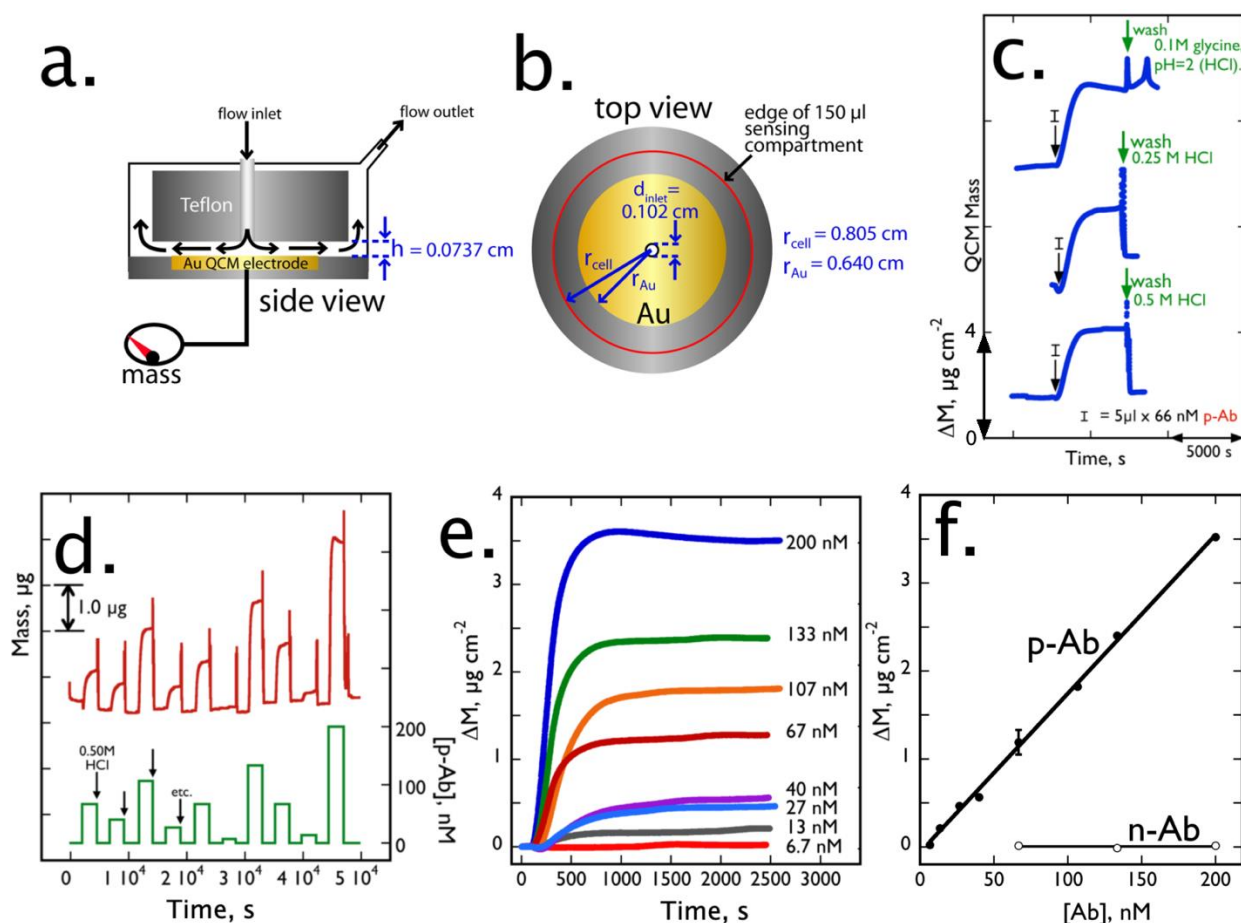


Figure 1.2 Quartz Crystal Microbalance (QCM) studies of covalent virus surfaces. a,b) Schematic diagram of the QCM and flow cell used for investigations of the CVS. c). QCM evaluation of the efficacy of three wash solutions: (top) 0.1 M glycine (pH~2 adjusted with HCl), (middle) 0.25 M HCl, and (bottom) 0.5 M HCl. d,e). d) Plot of mass vs time (top) for the exposure of a CVS to doses of p-Ab, ranging in concentration from 6.6 to 200 nM. Bound p8-Ab was removed after each injection using 0.5 M HCl. f) Plot of maximum mass change vs p8-Ab concentration for the data shown in (d,e). The mass change was proportional to the

concentrations of injected p8-Ab ($R^2 = 0.997$) and yielded a sensitivity of $0.018 \mu\text{g cm}^{-2}/\text{nM}$ and a limit of detection (LOD) of 6.6 nM.

These data demonstrated that virus particles bound within the CVL were available for the rapid binding of antibody in buffer solution, suggesting that the CVL could function as a bioaffinity layer within a biosensor. These data demonstrated that p8-Ab binding, while reversible, exhibited a very slow off-rate of $<10^{-5} \text{ s}^{-1}$, indicating that re-use of the CVL without removal of bound antigen using strong acid would not be impractical.⁴³ The next question was: Can the binding of a target antibody be detected directly using the electrochemical response of these virus-modified electrodes?

1.5.3 Electrochemical Signal Transduction of the CVL

In addition to mass-based transduction using QCM⁴³, the electrochemical response of the CVL to p8-Ab and n-Ab were investigated using electrochemical impedance spectroscopy (EIS).⁴⁴ A goal in these experiments was to carry out *direct detection* of antibody binding to the CVL. “Direct” in this context meant that a redox couple such as $\text{Fe}(\text{CN})_6^{4-/3-}$ was not added to the testing solution, an “*indirect*” approach in which the blocking of Faradaic electron transfer signal protein binding to an electrode surface.⁴⁵⁻⁵⁰ Direct EIS measurements, in contrast, probed changes to the non-Faradaic impedance of the CVL-modified gold electrode caused by antibody binding to the surface.

A surprising conclusion of these experiments was that the highest signal-to-noise (S/N ≈ 20) and best selectivity for p8-Ab binding to the CVL-modified electrode occurred at high frequencies in the range from 4 kHz – 140 kHz, in spite of the fact that the shift in the real component of the impedance signal, ΔZ_{re} , was the smallest in this frequency range – with ΔZ_{re}

$< 10 \Omega$ at all p8-Ab concentrations.⁴⁴ Selectivity for p8-Ab versus n-Ab was completely lost at lower frequencies, where ΔZ_{re} signals as large as $1 \text{ k}\Omega$ were observed. In contrast, prior work on EIS-detected indirect biosensors had emphasized the detection of target proteins at low frequencies, below 5 Hz in most cases. Z_{re} is increased by p8-Ab binding to the CVL because the bound, insulating p8-Ab molecules displace ionically conductive electrolyte from the free volume within the CVL layer.⁴⁴ The LOD for p8-Ab in these experiments, limited by the low ΔZ_{re} signal amplitude, was 20 nM .⁴⁴

The conclusion from these experiments was that this CVL did not afford enough sensitivity to enable the detection of proteins at sub-nM concentrations, as required for cancer screening. A fundamentally new method for preparing a virus-based bioaffinity layer was needed.

1.6 Virus-PEDOT Bioaffinity Layers

1.6.1 Electrodepositing a Virus-PEDOT Composite Film.

Inspiration for a new type of virus-based bioaffinity layer arrived from an unexpected direction. In the 2010 time frame, the Penner group had been investigating the thermoelectric properties of nanowires composed of the electronically conductive organic polymer PEDOT (poly(3,4-ethylene dioxythiophene)).⁵¹ These PEDOT nanowires were prepared by electrodeposition, using the Lithographically Patterned Nanowire Electrodeposition (LPNE) method.^{52,53}

Could PEDOT act as a host for M13 virus particles? This idea was interesting for two reasons: First, the electronic conductivity of PEDOT provided a means by which biosensor signal from M13 particles could be directly transmitted to an external circuit. Second, PEDOT

is positively charged as synthesized, with one positive charge for each 4 or 5 EDOT residues. During electropolymerization (Figure 1.3.a), 3,4-ethylene dioxythiophene (EDOT) is oxidized to a cation radical, and radical coupling occurs near the electrode surface until the resulting oligomers lose solubility and, with anions from the solution to balance the positive charge, they precipitate onto the electrode. M13 virus particles have a net negative charge near 6000, as a consequence of three ionizable moieties, Glu2, Asp4 and Asp5, on the 2700 copy P8 majority coat protein near its exposed N-terminus.⁵⁴ The hypothesis was that the polymerization of positively-charged PEDOT in the presence of negatively charged M13 would electrostatically promote the incorporation of M13 particles within the polymer matrix.

To test this hypothesis, virus-PEDOT biocomposite films were prepared by electropolymerizing EDOT in aqueous electrolytes containing just 12 mM LiClO₄ and nM concentration of M13 virus particles.⁵⁵ In these experiments, it was observed that the virus concentration was increased from 3 to 15 nM (the solubility limit), the EDOT electropolymerization current peak was depressed as compared to the virus-free control.⁵⁵ This observation suggested that the virus particles were either interfering with, or participating in, EDOT polymerization. QCM gravimetry (Figure 1.3.b) showed that the mass of the resulting films was augmented when virus particles were present in the EDOT polymerization solution. The excess mass, relative to pure PEDOT films (Figure 1.3.c), was attributed to the incorporation of virus particles into the growing PEDOT film.⁵⁵ This observation directly demonstrated that virus particles were being incorporated into these electrodeposited PEDOT films, as predicted by the reaction of Figure 1.3.a.

How efficient is the virus incorporation into these films during electropolymerization? The QCM data of Figure 1.3.c provided the answer: The difference in mass (the vertical axis) at a particular deposition charge, Q_{tot} , could be attributed to virus incorporated into the virus-PEDOT composite film. This analysis showed that concentration of the M13 in the virus-PEDOT film prepared by electrodeposition was directly proportional to the M13 concentration in the polymerization solution (Figure 1.3.d), and the slope of this line was an astonishing ≈ 500 . These experiments demonstrated that the reaction shown in Figure 1.3.a provided for highly efficient incorporation of virus into a growing PEDOT film. SEM images of electrodeposited virus-PEDOT composite films showed a striking transformation as virus was incorporated into the plating solution (Figure 1.3.e-j). In these images, bundles of virus particles are seen protruding at the surface of the virus-PEDOT films, and as expected, the density of these virus particles is correlated with the concentration of virus in the deposition solution.⁵⁵

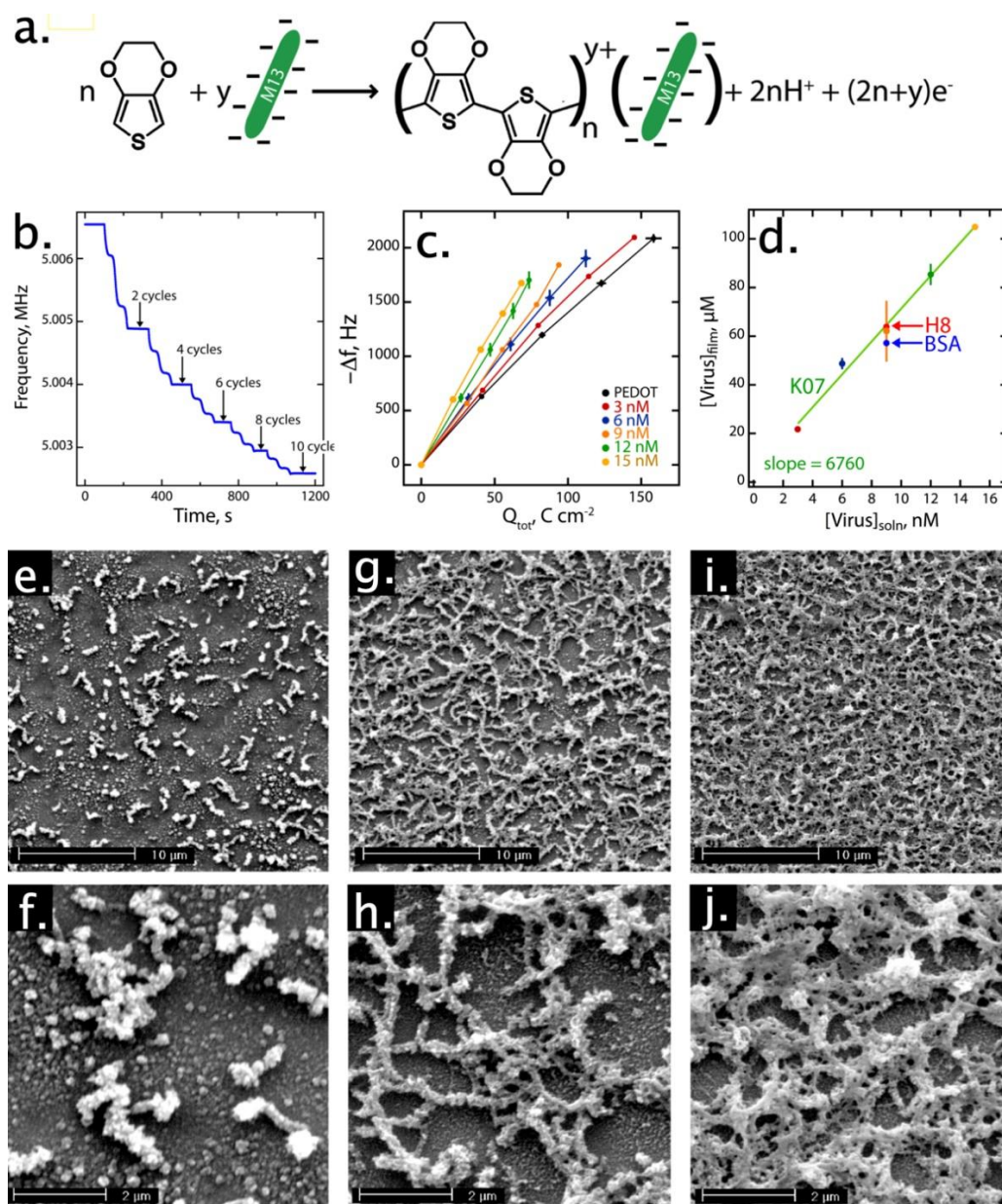


Figure 1.3 Electrodeposition of a virus-PEDOT bioaffinity layer. a). The virus-PEDOT electrodeposition reaction, b). QCM analysis of virus-PEDOT electrodeposition shows increased mass loading as a decrease in frequency. c) Frequency change versus deposition charge, Q_{tot} , for QCM measurements. The positive deviation of Δf for virus-containing solutions is due to virus incorporation into these films. d) Calibration curve showing the linear correlation of the virus concentration within the PEDOT film (vertical axis) versus the concentration of virus in solution. (e-j). Topography of virus-PEDOT films imaged by scanning electron microscopy at two magnifications. All films were prepared using 10 deposition cycles (20 mV/s) from a solution of aqueous 12.5 mM LiClO_4 , 2.5 mM EDOT, and virus particles at three concentrations: (e,f) $[\text{virus}]_{\text{soln}} = 3 \text{ nM}$, (g,h) $[\text{virus}]_{\text{soln}} = 9 \text{ nM}$, and (I,j) $[\text{virus}]_{\text{soln}} = 15 \text{ nM}$.

1.7 Biosensing with Virus-PEDOT Nanowires.

What would be the best way to exploit this new virus-PEDOT material in a biosensor? The initial answer to this question was to prepare arrays of nanowires composed of virus-PEDOT.^{56,57} These were prepared using LPNE^{52,53,58} in conjunction with the same electrodeposition protocol employed for virus-PEDOT films described above.⁵⁵ The resulting virus-PEDOT nanowires, deposited onto glass surfaces, were linear, millimeters in length, ≈ 300 nm in width and 60 nm in height. SEM, AFM and fluorescence microscopy confirmed the incorporation of M13 into the conducting PEDOT nanowire arrays, and further fluorescence studies also demonstrated the viruses remained intact and fully functional for binding to analytes.^{56,57}

Biosensing experiments were conducted by measuring the dc resistance of a virus-PEDOT nanowire array, rather than the frequency-dependent impedance of these arrays,^{56,57} as in previous studies, and p8-Ab and the n-Ab control were compared as before. A p8-Ab concentration dependent increase in resistance was observed, culminating in a 40% increase in response to exposure to 99 nM buffered p8-Ab solutions. A limit-of-detection for p8-Ab of 20 nM was established for these nanowire arrays. n-Ab showed no measurable signal.⁵⁶

Arrays of virus-PEDOT nanowires were also employed for the detection of prostate-specific membrane antigen (PSMA), a promising urine-borne cancer marker for prostate cancer.^{59,60} PSMA is a 750 residue, 100 kDa glycoprotein that is overexpressed as a homodimer on the surface of prostate cancer cells.^{59,60} These studies exploited virus particles engineered to display the PSMA-binding epitope PSMA-3 (amino acid sequence SECVEVFQNSCDW). In spite of this change to the virus, the virus-PEDOT electrodeposition is unaffected because this process is completely modular with respect to the phage

incorporation. In spite of the smaller size of PSMA relative to antibodies (100 kDa *versus* 155 kDa), similar detection metrics were achieved in this study which culminated in a LOD_{PSMA} of 66 nM in high salt (≈ 160 mM) PBS buffer solutions and a linear response up to 150 nM PSMA.

The conclusion of these two studies^{56,57} was that arrays of virus-PEDOT, transduced using the dc resistance, performed approximately as well as the EIS-transduced CVL-modified gold electrodes. A more direct comparison of virus-PEDOT with the CVL was needed in experiments that exploited conventional electrodes and EIS, and this was our next step.

1.8 Electrochemical Signal Transduction for virus-PEDOT films.

As compared with virus-PEDOT nanowires, a simpler approach was to coat a virus-PEDOT film onto a gold electrode. The response of such electrodes was studied using EIS for the detection of PSMA^{61,62} and, separately, p8-Ab.⁶³ p8-Ab detection at virus-PEDOT electrodes showed much higher signal-to-noise, ranging from 17 to 30, at high frequencies in the 100 Hz – 10 kHz range. At 1 kHz, a LOD for p8-Ab of 6 nM was achieved, and quantitation of p8-Ab up to 65 nM was possible. This represented a 65% reduction in LOD for p8-Ab compared to the identical experiment conducted using CVL-modified gold electrodes.

An even better result was obtained for the detection of PSMA as a consequence of the application of a new paradigm: Synergistic dual ligand phage.^{61,62} The hypothesis tested in this paper was that two peptide binders can be better than one. In other words, the sensitivity to PSMA could be improved by incorporating a *second* peptide binder (called K_{CS} .

1) for PSMA onto an engineered phage (phage-2) that already displayed a peptide binder for the protein (Figure 1.4.a). This was accomplished by conjugating a positively charged poly(lysine) tether to the polypeptide and then permitting it to self-assemble by electrostatic attraction onto the negatively charged phage after the electrodeposition of virus-PEDOT bioaffinity layer (Figure 1.4.b).^{61,62} The virus-PEDOT electrode was otherwise identical to those studied previously (Figure 1.4.d). The addition of the second ligand, KCS-1, significantly increased the affinity of the virus for PSMA in ELISA measurements (data not shown), and for electrochemical measurements (Figure 1.4.d). This enhanced sensitivity afforded a $LOD_{PSMA} = 100$ pM was seen both in buffer and in synthetic urine solutions (Figure 1.4.e) for these dual ligand systems.

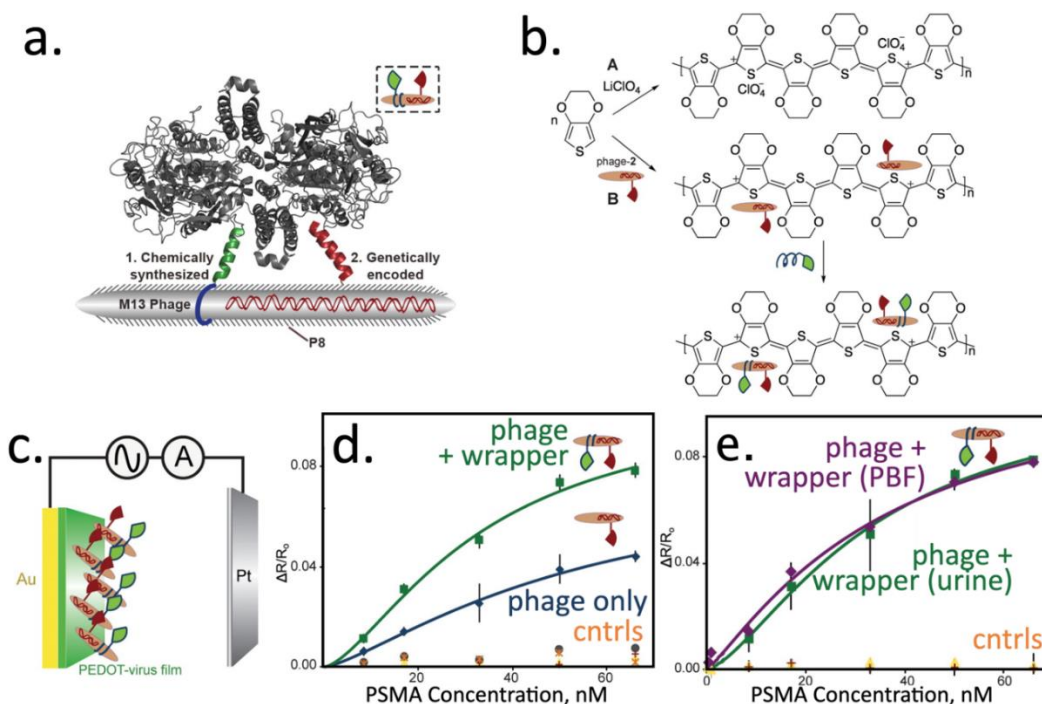


Figure 1.4 PSMA Detection in Synthetic Urine Using Synergistic, Dual-Ligand Phage. a) Schematic diagram of bidentate binding to PSMA by chemically synthesized (KCS-1, green) and genetically encoded (peptide, red) ligands to PSMA. The former ligand wraps non-covalently onto the negatively charged P8 proteins found on the phage surface due to

conjugation with a positively charged K14 peptide (blue). Simultaneous binding by the two ligands provides higher apparent affinity to PSMA. b). Schematic diagram showing the polymerization of EDOT in the presence of: (top) LiClO₄ or (center)) PSMA-binding phage, and (bottom) PSMA-binding phage and exposure to the wrapper KCS-1 (Green), c). Schematic diagram of the biosensing experiment. (d) $\Delta R/R_0$ of the film increases with the PSMA concentration. (e) Comparison of PSMA detection in synthetic urine (green) with detection in PBF buffer (purple).

1.9. The two-sided virus-PEDOT biosensor

All of the virus-based biosensors investigated in Penner laboratories up to 2015 were laboratory experiments^{33,43,44,56,57,61,63-65} in the sense that electrochemical measurements conducted using three-electrode cells incorporating separate reference, counter, and working (sensor) electrodes. A portable, miniaturizable, and commercializable electrochemical sensor architecture – in which the necessary electrodes were incorporated into a single monolithic sensor body - had not been demonstrated.

This advance occurred in 2017 with the demonstration by Alana Ogata, Ming Tan, and others that two virus-PEDOT modified gold electrodes, without separate reference or counter electrodes (Figure 1.5.a), could function as a biosensor for human serum albumin (HSA).⁶⁶ Prior work on PSMA^{62,65} had demonstrated that the signal generated by a virus-PEDOT-modified gold electrode was concentrated in the resistive component of the impedance, Z_{re} , instead of the capacitive component, Z_{im} . The hypothesis explored in the 2017 “two-sided” sensor architecture (Figure 1.5.b) was that arranging *two* virus-PEDOT bioaffinity layers electrically in series would double the impedance signal produced by the biosensor.⁶⁶

Despite its simplicity, the two-sided virus-PEDOT biosensor reliably distinguished HSA from BSA – proteins of identical size and having a 76% sequence homology. This demonstrated that the inherent selectivity of the engineered virus could be recovered with this device (Figure 1.5.b, c). At an optimized detecting frequency of 340 Hz (Figure 1.5d), the two-sided sensor produced a prompt increase in Z_{re} within 5 s and a stable Z_{re} signal within 15 min. HSA concentrations in the range from 100 nM, its LOD, to 5 μ M were detectable using this device (Figure 1.5e). These single-use biosensors demonstrated excellent sensor-to-sensor reproducibility characterized by a coefficient-of-variation of 2–8% across the entire concentration range, a remarkable achievement considering each sensor was hand made in our laboratories.⁶⁶ Two-sided virus-PEDOT sensors in synthetic urine demonstrated a concentration dependent response to HSA similar to PBS buffer.

This performance provided reason for optimism, however the two-sided virus-PEDOT biosensor had two serious deficiencies: First, its 100 nM LOD for HSA was insufficient to enable the measurement of cancer markers in urine at sub-nanomolar concentrations. The two-sided sensor simply didn't produce enough signal - a *maximum* of 12 Ω of signal against a 100-200 Ω background (Figure 1.5e).⁶⁶ Second, the two-sided biosensor required that current was carried through the test solution between the two electrodes, thus convoluting the resistance change due to binding of the target protein with the resistance of the solution. Since urine and other bodily fluids have highly variable ionic conductivities, this imposes a barrier to the use of the biosensor for single patient samples. In order to provide reliable results for highly variable single patient clinical samples, a biosensor architecture that decoupled target binding from ionic conduction was required. Despite of these two issues, the two-sided virus-PEDOT biosensor was the progenitor of the VBR.

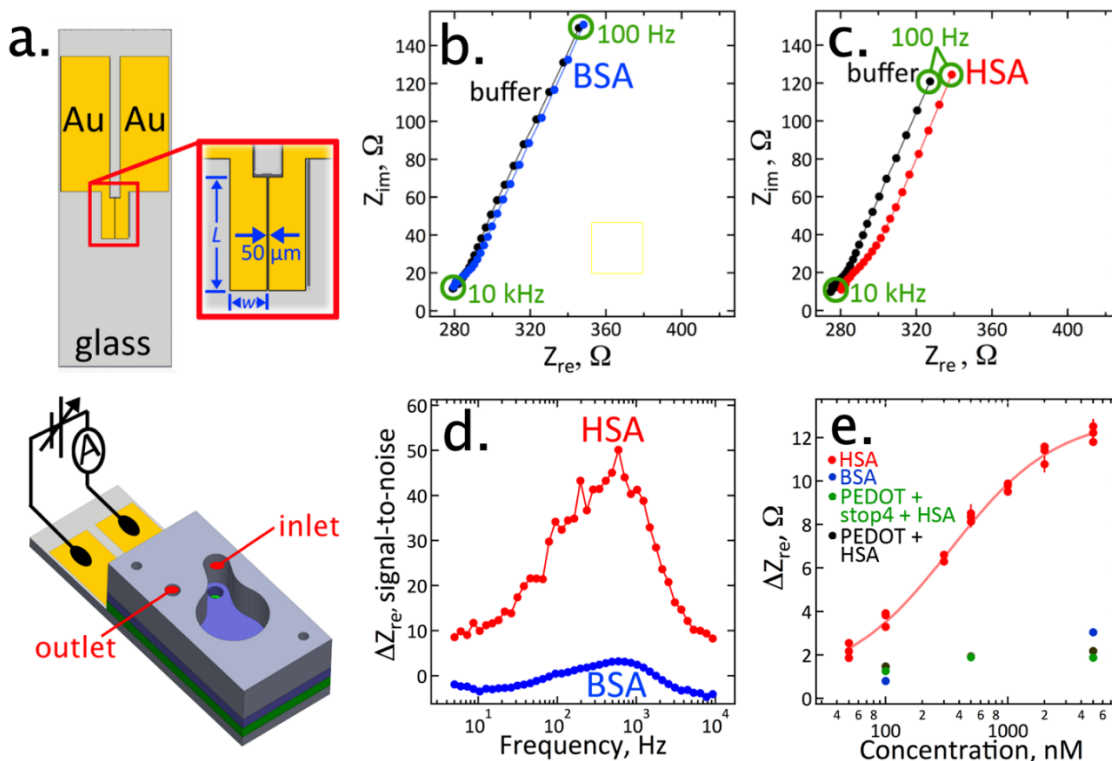


Figure 1.5. The Two-Sided Biosensor: A Monolithic Biosensor for Human Serum Albumin (HSA). a). Engineering diagram of two electrode virus-PEDOT biosensor. b,c) Nyquist plots (Z_{im} vs. Z_{re}) for a control protein (BSA) and HSA. d). Signal-to-noise versus frequency plot for HSA and BSA. e). ΔZ_{re} versus HSA concentration calibration curve. Controls for BSA, and off-virus binding also shown. After Ref.⁶⁷

1.10 Scope of this dissertation

The VBR was conceived in 2017, and since then, to fully realize its capabilities.^{64,67} The extension of the two-sided biosensor to the VBR is almost trivial: The virus-PEDOT bioaffinity layer was extended across the gap between the two gold electrodes. Since the virus-PEDOT layer is electrodeposited, this modification required that a conductor was deposited across this gap first. A spin-coated PEDOT:PSS layer was used for this purpose and the virus-PEDOT layer was electrodeposited on top of it.^{64,67} This two-layer construct connecting the gold electrodes is referred to as the VBR “channel”. The elaboration of the

two-sided biosensor dramatically altered its properties, which are discussed in the second chapter of this dissertation. With HSA as the model system, attributes like detection range, limit of detection, sensitivity and selectivity are uncovered. In the subsequent chapters, methods to increase signal and sensitivity will be discussed along with the implications on overall sensing capability. Chapter 3 modifies the bottom PEDOT:PSS layer and the effect is studied on DJ1 protein, a 20.8 kDa bladder cancer biomarker. Chapter 4 attempts to extend the possibility of VBR application to detect large biomolecules (150kDa) such as antibodies. A different modification is suggested to achieve the goal. Interesting morphological modifications are tracked by microscopy techniques.

Chapter 2

The Virus Bioresistor: Wiring Virus Particles for the Direct, Label-Free Detection of Target Proteins

This chapter is adapted from a research article (Bhasin, A; Ogata, Alana F; Briggs, Jeffrey S; Tam, PY; Tam, Ming X; Weiss, Gregory A; Penner, Reginald M. *Nano Letters*. **2018**, 18 (6), 3623-3629)

2.1 Introduction

Investigating the electrical properties of microscopic biological entities such as organelles, bacteria, eukaryotic cells, and viruses is both interesting from a fundamental science perspective, as well as challenging because they are electrically insulating. How does one “wire” such structures to an external circuit? ^{68,69,70} Elegant solutions to this problem have been demonstrated involving interfaces to single cells, bacteria etc. involving single nanostructures or ensembles of nanostructures (nanowires, nanotubes, nanosheets, etc.). For example, electrical signals from single cells have been measured using graphene field-effect transistors, and nanowire-embedded n-p junctions.^{71,72} The “wiring” of bacteria to electrode surfaces has been accomplished using outer sphere redox mediators.^{73,74,75}

A new approach, the virus bioresistor (or VBR), provides the means for incorporating virus particles into an electrical circuit (Figure 2.1). The key to the VBR is an electronically conductive channel composed of poly(3,4-ethylenedioxythiophene) or PEDOT into which M13 virus particles are embedded (Figure 2.1a). Individual M13 virus particles are filamentous with dimensions of 6 nm (w) x 1.0 μ m (l). The recognition and binding of target molecules to thousands of M13 virus particles embedded in this polymeric channel is signaled by an electrical impedance signature, which can be measured by an external circuit (Figure 2.1b, c). The impedance response of the VBR is modeled by a simple equivalent circuit containing just three circuit elements: A solution resistance (R_{soln}), a channel resistance (R_{VBR}), and an interfacial capacitance (C_{VBR}) (Table 2.1). Information on target binding is contained in the R_{VBR} , which can be measured either at a single frequency or from the best fit of the Nyquist plot across 40 or 50 discrete frequencies using this equivalent circuit.

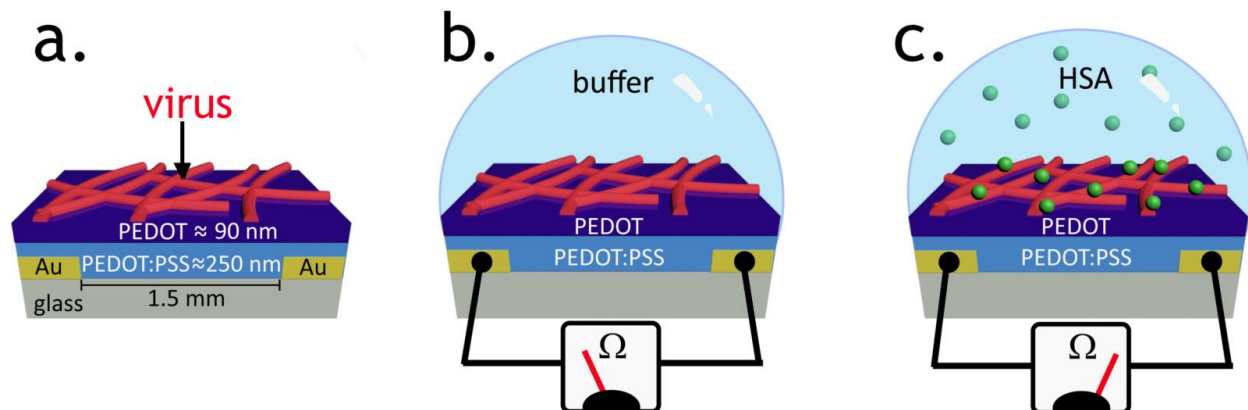


Figure 2. 1 The Virus BioResistor (VBR). a) Schematic diagram of a VBR showing critical components and dimensions. b) A buffered salt solution alters the solution resistance, R_{soln} , but not the resistance of the VBR channel, R_{VBR} . c) In the presence of a target protein (HSA in this case), R_{VBR} is increased, enabling determination of its concentration.

We demonstrate the VBR concept using a model system in which human serum albumin (HSA, 66 kDa), is detected in a phosphate buffer solution. The VBRs described here have a baseline dc resistance of 200-250 Ω which is the same in air or in an aqueous buffer solution, and are capable of producing large signals ($\Delta R_{VBR} \approx 250 \Omega$, or $\Delta R_{VBR}/R_o \approx 100\%$) for the detection of HSA in phosphate buffer solutions across the entire HSA binding curve ranging from $[HSA] = 7.5$ to 900 nM. In spite of the fact that the electrical signal generated by VBRs derives purely from ensembles of biological entities, extremely high sensor-to-sensor reproducibility of this signal is attainable for the response of VBR biosensors culminating in a coefficient-of-variation of the measured $[HSA]$ for 20 sensors less than 15% across the entire HSA binding curve. The VBR achieves these metrics using a two-terminal, monolithic device architecture that is simple, robust, manufacturable, and inexpensive. No reagents and no sandwich amplification of the impedance signal are required, and no redox species are added to the test solution. Collectively, these data demonstrate the feasibility of

adapting the VBR concept to rapid, inexpensive urine and blood-based assays at the point-of-care.

2.2 Experimental Methods

2.2.1 Materials

Devices were designed and manufactured by the Penner lab. Devices and cells (Wainamics Inc., Fremont CA) were cleaned by O₂ plasma using a plasma cleaner (PDC-32G, Harrick Plasma) All chemicals were purchased from Sigma Aldrich and used as received, unless noted. Buffer solutions contained phosphate-buffered saline (PBS, 137 mM NaCl, 2.7 mM KCl, 10 mM Na₂HPO₄, 1.8 mM KH₂PO₄ pH 8) filtered through a 0.22 μM pore size membrane (Corning) and 2 mg/mL of Casein. Human serum albumin (Human Albumin fraction V; low folate, B12; MP Biomedicals; purity > 97%) were analyzed by SDS-PAGE and used as received. Bovine serum albumin (BSA, Calbiochem Omnipur) was used as received. EDOT was purified by silica flash chromatography.

2.2.2 Phage Library Design and the Selection of HSA Binders

The procedures associated with design of the phage library, selection of HSA binders from this library, and screens to isolate the HSA-binding virus were described previously.¹²

2.2.3 VBR Fabrication

The fabrication process for one pair (2) of VBRs involved the following four steps (Figure 2.2). First, two pairs of gold-electrodes are prepared by photolithography. These

gold electrodes have width of 2 mm and their separation of 1.5 mm defines the *VBR* channel length. Gold electrode pairs are separated laterally by 0.5 mm. Second, a layer of PEDOT:PSS is spin-coated onto the gold-electrode device and baked for 1 hr at 90°C. Third, a 2 mm x 2 mm PMMA cell is attached defining the area of the *VBR* bioaffinity layer. Fourth and finally, a virus-PEDOT top layer is electropolymerized on top of the PEDOT-PSS bottom layer by using $\approx 100 \mu\text{L}$ of plating solution and applying two oxidizing voltammetric scans. The virus-PEDOT plating solution is removed and the cell is rinsed. Electrodes are used to enable impedance measurements at each of the two *VBR* sensors. One background impedance measurement is acquired in buffer, and a second in a solution containing added HSA. The difference between these two measurements, calculated at each frequency, is ΔR_{VBR} .

Further details relating to this process are the following: Gold-film electrodes were cleaned by O_2 plasma for 10 min immediately before use. Scotch tape was placed on the ends of the electrodes to protect the contacts. A poly(3,4-ethylenedioxythiophene)-poly(styrenesulfonate) (PEDOT:PSS, 1.0 wt.% in H_2O , high conductivity grade) layer was deposited on the electrodes by spin-coating (2500 rpm, 80s) and baked for 1 hr at 90°C. Electrodes were then allowed to come to room temperature and the cell was then mounted on the gold-film electrodes followed by the incubation of the electrodes in PBS for 90 min. Next, virus-PEDOT films were electropolymerized onto the PEDOT:PSS/gold-film electrodes using a platinum foil counter and a mercurous sulfate electrode (MSE). Virus-PEDOT films were prepared by cycling between 0.2 V and 0.8 V at a scan rate of 20 mV/s in plating solution using a PARSTAT 2263 controlled by Electrochemistry PowerSuit 2.6 software. Plating solutions contained 8 nM M13 bacteriophage, 12.5 mM LiClO_4 , 2.5 mM EDOT and electropolymerized for 2 cycles.

VBRs were evaluated at every step of the fabrication process to ensure the reproducibility of signal for a particular HSA concentration. Starting with the fabrication by photolithography of gold electrodes, the VBR is prepared in four steps (Figure 2.2). The parameters measured at each of these steps is indicated in the diagram for Fig. 2.2. In this diagram, the following definitions apply: R_{Au} is the dc resistance of the gold electrodes prepared in step 1, measured along their longest dimension, R_{trans} is the dc resistance of the PEDOT-PSS film produced in step 2, i_p is the peak current for the electropolymerization, by cyclic voltammetry, of the virus-PEDOT composite in step 3, $Z_{im,m}$ and $Z_{re,m}$ are the baseline impedances measured for the complete VBR measured in 160 mM PBS buffer solution. VBR device yield using these process windows was $\approx 30\%$.

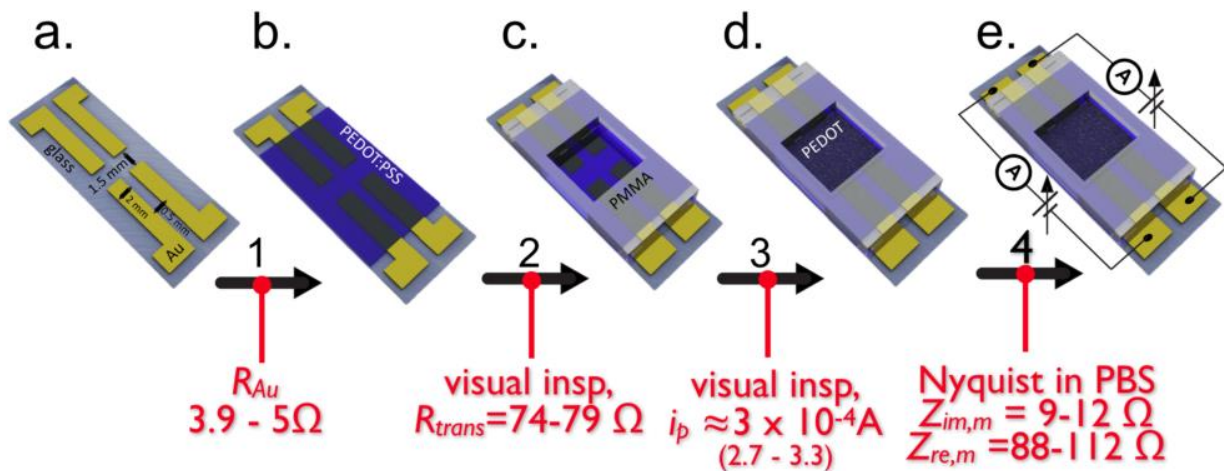


Figure 2. 2 Process flow for the four-step VBR fabrication process, including the process windows that were enforced for this process, indicated in red.

2.2.4 Impedance Spectroscopy (IS)

All buffer solutions were prepared and brought to room temperature (74 °F) prior to EIS measurements. Newly plated phage-PEDOT chemiresistor films were washed three times with PBS and subsequently incubated in PBS for 10 minutes. All EIS measurements were taken with the PBS solution as the run buffer. Three consecutive IS measurements were taken using a PARSTAT 2263 controlled by Electrochemistry PowerSuit 2.6 software. 50 data points were acquired across a frequency range of 5 Hz to 40 kHz. The amplitude of the applied voltage was 10 mV for all EIS measurements. Chemiresistor films were then incubated in HSA solutions in run buffer for 10 min followed by three consecutive IS measurements. Independent electrodes were used for measurements of a single concentration of HSA solutions and BSA solutions. Equivalent circuit fitting was acquired using the EIS Analyzer software (ABC Chemistry).

2.2.5 AFM and SEM Analysis.

Scanning electron microscopy (SEM) were acquired on uncoated films at 2 keV using a FEI Magellan 400L XHR system. Atomic force microscopy (AFM) was performed on chemiresistor films using an Asylum MFP-3D-SA atomic force microscopy (Asylum Research, Santa Barbara, CA) equipped with Olympus AC160TSAFM tips (Olympus) in laboratory ambient air. AC Mode AFM images were acquired at 512 x 512 pixels spanning a 20 μm range. The Asylum image processing software was used to analyze AFM images and amplitude traces.

2.3 Results and Discussion

The fabrication of a VBR involves the preparation of two gold electrical contacts on a glass substrate by photolithography (Figure 2.3). On top of these contacts, a two-layer VBR channel (15 mm (l) x 20 mm (w)) is prepared consisting of a spin-cast PEDOT-PSS semiconductor bottom layer (200-300 nm in thickness) and an electrodeposited virus-PEDOT composite top layer containing thousands of engineered M13 virus particles^{55,57,63} (90 – 100 nm in thickness). This virus-PEDOT electrodeposition process involves the application of two oxidizing voltammetric scans to an aqueous solution containing 8 nM M13 virus particles in 12.5 mM LiClO₄, 2.5 mM EDOT (Figure 2.3a).

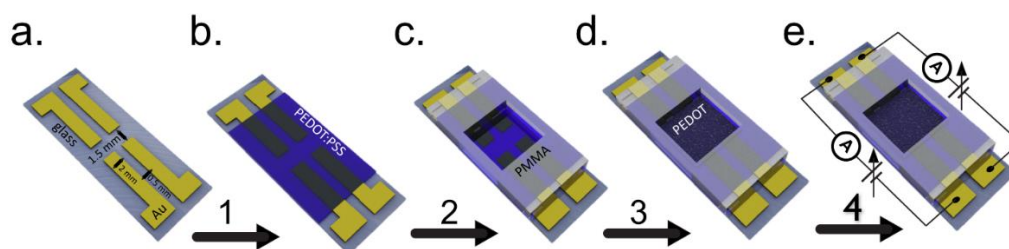


Figure 2.3 VBR biosensor fabrication. a) Two pairs of gold-electrodes from which two VBRs are prepared. The gold electrodes have width of 2 mm and their separation of 1.5 mm defines the channel length of these devices. The two pairs of gold electrodes are separated by 0.5 mm. b) A layer of PEDOT:PSS is spin-coated onto the gold-electrode device and baked for 1 h at 90 °C. c) A 2 mm x 2 mm PMMA cell is attached defining the area of the bioaffinity layer. d) A virus-PEDOT top layer is electropolymerized on top of the PEDOT-PSS bottom layer by using $\approx 100 \mu\text{L}$ of plating solution and applying two oxidizing voltammetric scans. e) The virus-PEDOT plating solution is removed, and the cell is rinsed. Electrodes are used to enable impedance measurements at each of the two VBR sensors. One background impedance measurement is acquired in buffer, and a second in a solution containing added HSA. The calculated ΔR_{VBR} is used to determine the HSA concentration in this sample with reference to a calibration curve.

If the PEDOT-PSS/PEDOT-virus layer that electrically connects the two metal electrodes is severed, forcing current traveling between these two electrodes into the

solution phase, we recently demonstrated that the resulting device still functions as a biosensor.⁶⁶ But the VBR has three attributes not found in this device: 1) An impedance signal that is amplified by a factor of 20 (200 Ω here versus 12 Ω in our prior work.⁶⁶ The result is a limit-of-detection of 7.5 nM in the VBR versus 100 nM in the earlier device,⁶⁶ 2) The ability to decouple this signal from the salt concentration of the solution (*vide infra*), and, 3) A dramatically faster response time of \approx 5 s here versus 8-10 min.⁶⁶

A cross-sectional SEM image of a VBR biosensor film shows a virus-PEDOT top layer with a thickness of \sim 92 nm on top of a \sim 245 nm PEDOT:PSS bottom layer (Figure 2.4b). Plan-view SEMs of pure PEDOT films prepared in an aqueous plating solution of 2.5 mM EDOT and 12.5 mM LiClO₄ show a smooth, homogenous surface (Figure 2.4c). Virus-PEDOT films prepared from the same plating solution with the addition of 8 nM virus show dark, filamentous structures within the virus-PEDOT top layer (Figure 2.4d). These filaments are M13 bacteriophage, which have typical dimensions of 6 nm (diameter) x 1.0 μ m (length). Atomic force microscopy (AFM) images show that in the absence of virus particles, the virus-PEDOT top layer is smooth with an RMS surface roughness of 5 nm (Figure 2.4.e, g). If this layer is produced to contain virus particles, a slightly rougher surface is seen with an RMS roughness of 10 nm; however, a distinct topography reveals the presence of fiber like structures that can be attributed to PEDOT-covered virus strands protruding from the PEDOT surface (Figure 2.4f, h). After the virus-PEDOT top layer is electrodeposited, the bioaffinity layer is complete, and the VBR is ready to use.

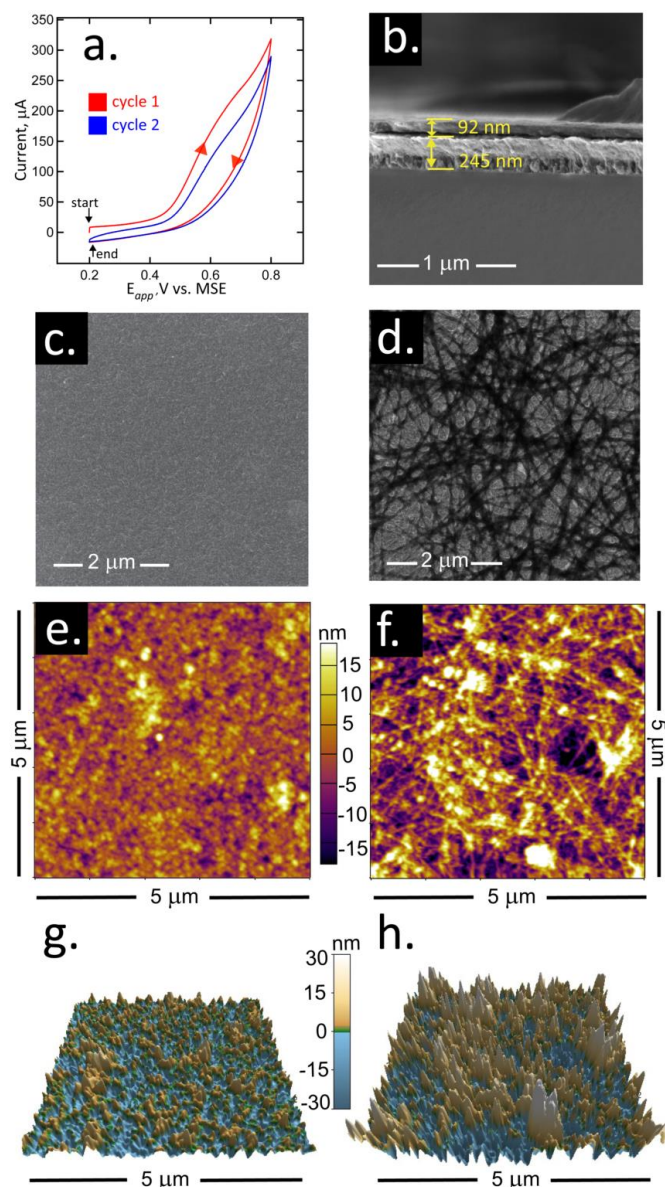


Figure 2. 4 Electrodeposition and SEM/AFM characterization of virus-PEDOT bioaffinity layers. (a) Electrodeposition of a virus-PEDOT film on a PEDOT-PSS film using cyclic voltammetry (50 mV/s). The virus-PEDOT top layer is prepared by two cycles from an aqueous virus-EDOT solution containing 2.5 mM EDOT, 12.5 mM LiClO₄, and 8 nM HSA phage. (b) cross sectional scanning electron microscopy (SEM) image of a PEDOT-PSS/virus-PEDOT film. The PEDOT-PSS bottom layer and virus-PEDOT top layer can be distinguished. (c) Plan view SEM image of a PEDOT only film (no virus) prepared by two consecutive cycles of deposition in aqueous EDOT solution containing 2.5 mM EDOT, 12.5 mM LiClO₄. (d) Plan view SEM image of a virus-PEDOT film prepared as described in (a). (e, f, g, h) Atomic force microscopy (AFM) images of PEDOT films (e, g) and virus-PEDOT films (f, h). The same AFM image data are represented in two ways: (e, f) shows height versus position data while (g, h)

show a three-dimensional rendering of these the same data shown in (e, f). The rms roughness for PEDOT and virus-PEDOT films are ≈ 5 nm and ≈ 10 nm, respectively.

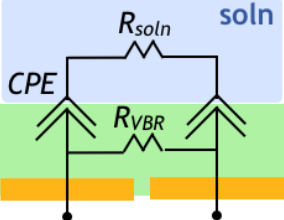
We elected to monitor VBRs using an ac impedance measurement, rather than applying a simpler dc resistance measurement, because prior work on conductive polymer based chemiresistors have shown conclusively that dramatically lower noise can be accessed using ac detection, even at frequencies as low as 5 Hz.^{76,77,78} Analytical equations for the real and imaginary components of the complex impedance, Z_{re} and Z_{im} (Table 2.1), are used to fit experimental impedance data to extract the values of the three circuit elements: R_{soln} , R_{VBR} , and C_{VBR} . A version of the equivalent circuit in which a constant phase element (CPE) is substituted for each capacitor is used for this purpose. This elaboration provides better agreement between the calculated and the experimental impedance data, resulting in improved precision for the measurement of R_{VBR} (Table 2.1). The impedance of a CPE, Z_{CPE} , and the capacitive impedance, Z_C , are defined by these equations:

$$Z_C = \frac{1}{i \omega C} \quad Z_{CPE} = \frac{1}{i \omega Q^n}$$

where ω is the angular frequency (s^{-1}), $i = \sqrt{-1}$. Q^n is the CPE capacitance (F) where n has a value of 1.0 if the CPE is purely capacitive. n is used as a fitting parameter in this study and has a value of $1.0 < n < 1.2$.

Table 2.1 Equivalent circuits and equations representing the electrical response of a VBR biosensor.

Eq. Circuit ^a	
-----------------------------	--

$Z_{re} =$	$\frac{R_{VBR}R_{soln}(R_{VBR} + R_{soln}) + \frac{R_{VBR}}{\omega^2 C_{VBR}^2}}{(R_{VBR} + R_{soln})^2 + \frac{1}{\omega C_{VBR}}}$
$Z_{im} =$	$\frac{\frac{R_{VBR}^2}{\omega C_{VBR}}}{(R_{VBR} + R_{soln})^2 + \frac{1}{\omega C_{VBR}}}$
Eq. Circuit ^b	
$Z_{re} =$	$\frac{R_{VBR} [1 + Q_{VBR} \omega^n (2R_{VBR} + R_{soln}) \cos \frac{\pi n}{2} + R_{soln} Q_{VBR}^2 \omega^{2n} (R_{soln} + R_{VBR})]}{Q_{VBR} \omega^n (R_{soln} + R_{VBR}) \left[(R_{soln} + R_{VBR}) Q_{VBR} \omega^n + 2 \cos \frac{\pi n}{2} \right] + 1}$
$Z_{im} =$	$\frac{- R_{VBR}^2 \omega^n Q_{VBR} \sin \frac{\pi n}{2}}{Q_{VBR} \omega^n (R_{soln} + R_{VBR}) \left[(R_{soln} + R_{VBR}) Q_{VBR} \omega^n + 2 \cos \frac{\pi n}{2} \right] + 1}$

^aCapacitive equivalent circuit, ^bEquivalent circuit with constant phase elements (CPEs).

The *VBR* produces a distinctive impedance response consisting of a semicircular Nyquist plot (Z_{im} versus Z_{re} as a function of frequency) (Figure 2.5a-c). This response resembles the Randles equivalent circuit that is commonly seen for electrochemical biosensors operating in the presence of an added redox species, such as $\text{Fe}(\text{CN})_6^{3-/4-}$.^{79,80} The semicircular Nyquist plot for electro-chemical biosensors derives from electron transfer to and from the redox species present in the solution. When a redox species is not added, no semicircle is observed. The *VBR* produces a semicircular Nyquist plot *without added redox species*. Instead, the *VBR* channel presents a parallel resistance – dominated by electron conduction through the polymer composite *VBR* – and capacitance – produced by the non-Faradaic charging and discharging of the electrical double layer at the surface of the *VBR*.

The semicircular Nyquist plots aids in the precision with which R_{VBR} can be measured – just as it does in electrochemical biosensors that use the diameter of this semicircle – the so-called charge transfer resistance – to transduce target binding.^{81,82,83}

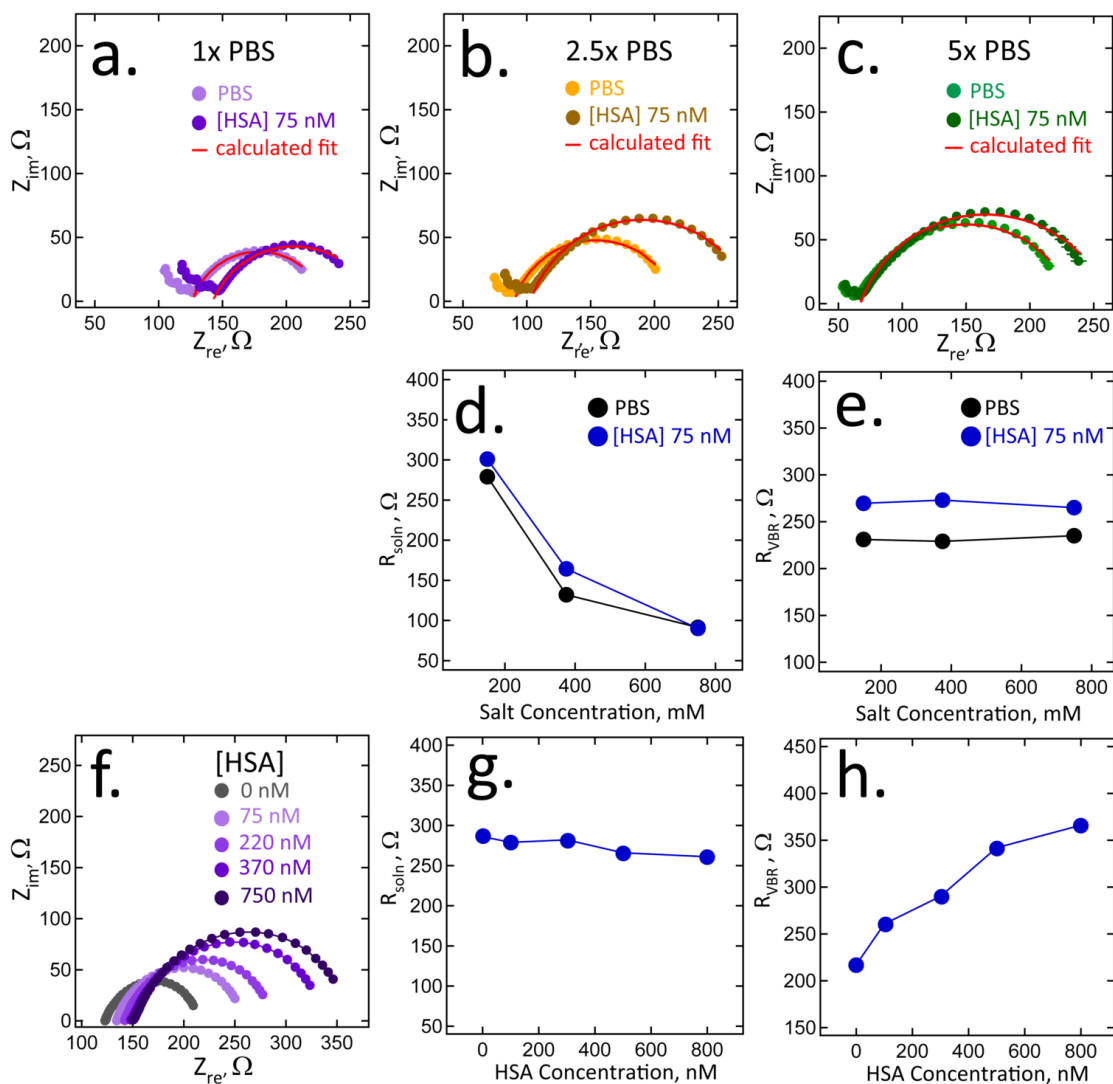


Figure 2.5 Orthogonal measurement of R_{soln} and R_{VBR} using a VBR biosensor. Nyquist plots summarizing the impedance response of VBRs from 1 Hz to 10 kHz with equivalent circuit fits (red traces). (a,b,c) VBRs in solutions of run buffer of: a) 1x PBS (purple), b) 2.5x PBS (yellow), c) 5x PBS (green), before and after exposure to 75 nM HSA in the same buffer. (d,e). Plots of R_{soln} and R_{VBR} as a function of buffer concentration extracted from the data of a,b, and c. Shown are the values of these two circuit elements in pure buffer, and in buffer with added 75 nM HSA, as indicated. (f,g,h) Experiment in which the HSA concentration is increased from 0 nM (1x PBS) to 750 nM (in 1x PBS) showing the invariance of R_{soln} and the linear increase in R_{VBR} .

VBR biosensors are able to distinguish between changes in the electrical resistance of the test solution, caused by variations in the salt concentration for example, and the concentration of target molecules present in this solution. Information on the electrical conductivity of the solution is contained in R_{soln} whereas the concentration of target protein is encoded by R_{VBR} . Virtually no cross-talk occurs between these two circuit elements. For example, Nyquist plots (Z_{im} versus Z_{re} as a function of frequency) for a VBR in three concentrations of PBS buffer (1x PBS, 2.5x PBS and 5x PBS) show the same $\Delta R_{VBR} = R_{VBR,HSA} - R_{VBR,buffer}$ signal for 75 nM HSA (Figure 2.5e) independent of the salt concentration ($[NaCl]$) over the range of 134 to 670 mM. Notably, R_{soln} decreases dramatically with increasing salt concentration (Figure 2.5d).

The complementary experiment is to vary $[HSA]$ in a 1x PBS buffer solution (Figure 2.5f). Here, Nyquist plots are shown for five buffer solutions containing $[HSA] = 0$ nM, 70 nM, 220 nM, 370 nM, and 750 nM. In this case, a quasi-linear increase in ΔR_{VBR} with $[HSA]$ is measured (Figure 2.5h), and R_{soln} remains constant (Figure 2.5g). This property of VBRs – the ability to parse changes in impedance due to the solution resistance and target binding – provides an enormous advantage in terms of the application of this biosensor technology to body fluids where salt concentrations are unknown and uncontrolled.

VBR performance was evaluated for the detection of HSA using 20 VBRs in order to assess sensor-to-sensor reproducibility and coefficient-of-variance (CoV) to determine their practicality for single use biosensors. Two methods for analyzing VBR impedance data are also assessed here. The first method was previously used for non-faradaic impedance biosensors where the signal-to-noise guided the selection of a single frequency at which

either ΔZ_{im} or ΔZ_{re} was calculated by, for example, $Z_{re,HSA} - Z_{re}^0$. Using this approach, the sensing signal at 5 Hz was selected. The second method exploits a range of impedance data across 40-50 discrete frequencies and employs a fit to the equations of Table 2.1 to determine ΔR_{VBR} . Method 1 will afford more rapid analysis because impedance data at a single frequency is required. Method 2 requires longer analysis times; however, the approach has the potential to provide for higher precision and reduced noise for an assay, but can this advantage be demonstrated? To answer this question, the two methods were compared for three independent VBR biosensors ($N = 3$) at each HSA concentration from 7.5 nM to 750 nM to evaluate sensor-to-sensor reproducibility. In addition, two sensors ($N=2$) were tested at 900 nM [HSA].

The performance of Methods 1 and 2 are summarized in the plots of Figure 2.6a and b, respectively. The main conclusion is that there is little difference in the performance of these two methods in terms of sensitivity, precision, and noise. Both ΔZ_{re} , 5Hz (Method 1) and ΔR_{VBR} (Method 2) track increases in the HSA concentration from 7.5 nM to 900 nM HSA, saturating at close to 900 nM. These two calibration plots are both fitted with the Hill equation, which is frequently used to model biosensor response:⁸⁴

$$\Delta Z_{re} = \Delta Z_{re,lim} + \frac{\Delta Z_{re,0} - \Delta Z_{re,lim}}{1 + \left(\frac{C_{HSA}}{K_D}\right)^h}$$

The best fit to the Hill equation for the ΔZ_{re} calibration plot results in $\Delta Z_{re,lim} = 250 \pm 40 \Omega$, $\Delta Z_{re,0} = 16 \pm 5 \Omega$, $K_D = 480 \pm 120 \text{ nM}$, $h = 1.6 \pm 0.3$, and $R^2 = 0.97$. Fit to the Hill equation for the $\Delta R_{channel}$ calibration plot results in $\Delta R_{VBR,lim} = 250 \pm 30 \Omega$, $\Delta R_{VBR}^0 = 20 \pm 5 \Omega$, $K_D = 410 \pm 60 \text{ nM}$, $h = 1.9 \pm 0.3$, and $R^2 = 0.98$. These data provide no justification for the use of multiple

analysis frequencies (Method 2) as compared with a single, S/N-selected, analysis frequency (Method 1). Apparent K_D values are identical within experimental error. Values of h , which indexes the degree of cooperativity in target binding to virus particles, are also identical and equal to 1.6, which indicates significant cooperativity for phage binding to HSA in this system.

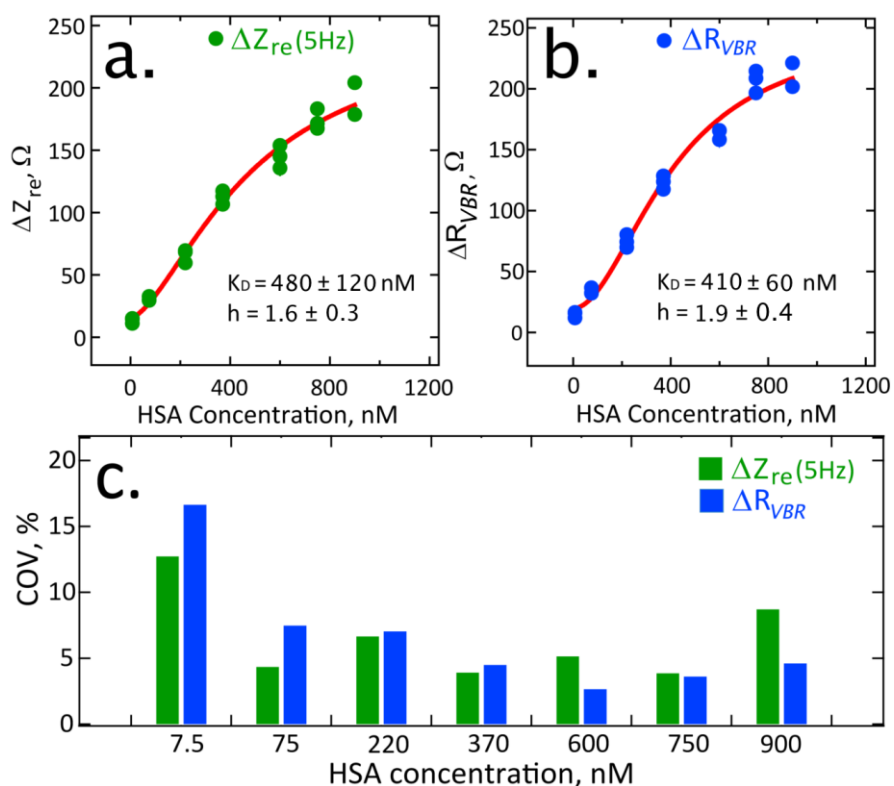


Figure 2.6 Calibration plots for 20 VBRs exposed to HSA concentrations 7.5 nM – 900 nM generated by two methods (a) sensing signal ΔZ_{re} , measured at 5 Hz, versus concentration (b) sensing signal defined as ΔR_{VBR} , versus concentration. At each of seven concentration points, three data point for three different VBR sensors are plotted here with error bars defined as the standard deviation, $\pm 1\sigma$. The exception is the 900 nM concentration point where just two sensors were used, and two data points are shown. It should be noted that these three data points are not all seen at all concentrations, since some are superimposed on others. Impedance data for HSA exposed to virus-PEDOT films containing HSA phage is fitted to the hill equation (red line). (c) compares the CoV% for the signals from two methods obtained by the variation in signal generated by three devices exposed to concentrations [HSA] = 7.5 nM - 900 nM.

The origin of the *VBR* impedance signal is of interest and remains the subject of investigation. Either of two signal transduction mechanisms could reasonably account for our observations: First, the PEDOT-PSS can function as a p-type organic semiconductor field effect transistor (FET).⁸⁵ In this case, an increase in ΔR_{VBR} with [HSA] is accounted for by the binding of a positively charged target molecule to the *VBR*, leading to depletion of majority carriers and an increase in impedance. But HSA has an isoelectric point, $pI = 5.3$,⁸⁶ and our PBS buffer has $pH = 8.0$, so the HSA in these experiments is expected to have an overall negative charge, not a positive charge, at this pH . The binding of HSA to the PEDOT *VBR* should therefore cause the accumulation of majority carriers, reducing its electrical impedance, which is contrary to our experimental observations. As demonstrated in Figure 2.5e, the signal amplitude observed for HSA is unaffected by increases in the salt concentration of the test solution from 1x PBS to 5x PBS. This observation suggests that an electric field effect is not involved in the signal transduction process, since the Debye length in these buffer solutions is both very small (2-8 Å) and variable.

A second, previously observed mechanism involves the disruption of long-range ordering in the PEDOT-PSS polymer chains. For example, bulky intercalators such as tosylate anions can cause an increase in electrical resistance,⁸⁷ or “secondary dopants” – or by “secondary dopants” – including diethylene glycol,⁸⁸ polyethylene glycol,⁸⁹ and dimethyl sulfoxide⁹⁰ – that lubricate the motion of polymer chains thereby promoting a higher degree of long range ordering and a lower electrical resistance. HSA is readily classified as falling into the first category of bulky, structure disrupter. This description qualitatively explains the increases in resistance seen for *VBRs* upon exposure to HSA reported here. Furthermore, this model is consistent with the observed impedance signal for HSA measured at *VBRs*

remaining unrelated to the salt concentration of the test solution. More work needs to be done with other analytes and solutions to cement our understanding of the *VBR* signal transduction mechanism.

In addition to sensitivity and reproducibility, selectivity and speed are the two other attributes important for biosensors. The selectivity of *VBR* biosensors was examined with two control conditions: 1) a *VBR* virus-PEDOT film containing HSA-binding virus measured for binding to 750 nM BSA protein, which is closely matched to HSA in terms of both size (both 66.5 kDa) and amino acid sequence (76% homologous)⁹¹, and, 2) a *VBR* virus-PEDOT film containing the negative control STOP4 virus, which has no displayed peptide ligands, in the presence of 750 nM HSA protein. The sensing signal is described as $\Delta R_{VBR} = R_{VBR,HSA} - R_{VBR,PBS}$, determined by fitting the impedance data with the equivalent circuit of Table 2.1. Both control *VBR* biosensors show less than $\sim 1 \Omega$ in of change (in either ΔR_{VBR} or ΔZ_{re}) in comparison to $\sim 200 \Omega$ resistance increase for HSA-virus-PEDOT films against 750 nM HSA.

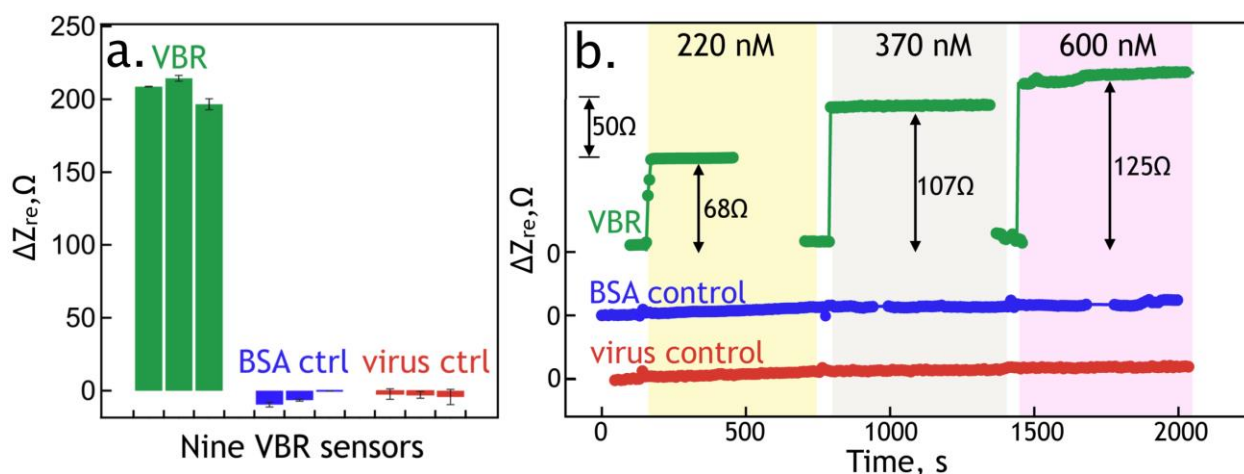


Figure 2.7 VBR specificity and speed. a). A specificity assay. Blue bars represent three VBRs with PEDOT films containing HSA binding phage exposed to 750 nM HSA; Red bars show the response to a 750 nM BSA solution of three VBRs containing HSA binding phage; Green bars

show the response to a 750 nM HSA solution for three VBRs containing STOP4 phage that have no affinity for HSA. b). Real time VBR sensing data. Responses for three VBR sensors are shown for [HSA] exposures of 220, 370, and 600 nM that show response times of 30 s, 3 s, and 3 s, respectively. The specificity assay summarized in (a) are also repeated here, in real-time sensing format, again showing no measurable responses.

The impedance response for *VBRs* gives excellent binding signal specific to HSA at 200x over background (Figure 2.7a). Real-time *VBR* measurements (Figure 2.7b) allow the response time of these devices to be directly measured. We observe a rapid (3 – 30s) step-wise increase in ΔZ_{re} followed by near instantaneous settling of Z_{Re} at the concentration-appropriate value (Figure 2.7b). This constitutes a near ideal response function for a biosensor and demonstrates the potential utility of *VBRs* for point-of-care applications.

2.4 Summary

The *VBR* simplifies the problem of electrically communicating with virus particles, and importantly, extracting valuable information in this process. Communication takes the form of an increase in the electrical impedance of the virus-PEDOT *VBR* in the presence of a target protein disease marker, relative to the impedance measured in a pure buffer solution. This impedance increases of up to 200 Ω signals the degree to which virus-displayed peptides have recognized and bound a particular target protein, leading to precise and highly reproducible measurement of the concentration of this target molecule. The *VBR* can bypass a ubiquitous noise source in electrical or electrochemical biosensing: the variable electrical impedance of the solution itself.

Chapter 3

The Virus Bioresistor: Wiring Virus Particles for the Direct, Label-Free Detection of Target Proteins

This chapter is adapted from a research article (Bhasin, A.; Sanders, E. C.; Ziegler, J. M.; Briggs, J. S.; Drago, N. P.; Attar, A. M.; Santos, A. M.; True, M. Y.; Ogata, A. F.; Yoon, D. V; et al. *Anal. Chem.* **2020**, *92* (9), 6654–6666)

3.1 Introduction

Minimally invasive cancer screening using bodily fluids – so called “liquid biopsies” – may eventually eliminate the evaluation of suspected malignancies using surgery.⁹² Liquid biopsies involve the detection in blood, urine, and other bodily fluids of nucleic acids, circulating tumor cells (in blood), or distinctive protein markers that signal the presence of a particular cancer. DJ-1, a 20.7 kDa protein, is elevated in the urine of people with bladder cancer (BC).^{93,94} Presently, the measurement of DJ-1 in urine requires an enzyme-linked immunosorbent assay (ELISA), which is both slow and inconvenient. A biosensor for DJ-1 could accelerate its assessment for the detection of BC recurrence in patients who have undergone treatment for the disease. But no biosensor for DJ-1 has been demonstrated, to our knowledge. Here we demonstrate that a new type of biosensor – the Virus BioResistor or *VBR* - that uses virus particles as receptors can be programmed to detect DJ-1 in human urine.

The *VBR* is a bioresistor contacted with two gold electrodes. The bioresistor consists of an electronically conductive channel composed of a layer of poly(3,4-ethylene dioxythiophene) (PEDOT) doped with virus particles. Recently,⁹⁵ we demonstrated the *VBR* concept for the detection of human serum albumin (HSA, 66.5 kDa) in high salt (160 mM NaCl) buffer. A limit-of-detection for HSA (LOD_{HSA}) of 7 nM was achieved in that study.⁹⁵ However, a sub-1.0 nM LOD for protein markers is required to enable cancer surveillance in urine. Here we unlock higher sensitivity for *VBRs* simply by engineering the PEDOT channel to concentrate the impedance in an ultra-thin (≈ 90 nm) virus-PEDOT composite layer. With this modification, a limit-of-detection of (LOD_{DJ1}) of 10 pM is achieved in urine (synthetic and

human), coupled with a dynamic range of more than four orders of magnitude from 10 pM to 300 nM. This performance is clinically relevant because it allows for the detection of elevated DJ-1 in the urine of patients who have bladder cancer (≈ 100 pM).^{93,94,96,97} Importantly, the modifications to the *VBR* do not compromise either the speed or the simplicity of its operation. As before⁹⁵, the *VBR* operates in a dip-and-read modality, and produces a stable, quantitative signal within 1.0 min. The sensing performance reported here also eclipses prior virus-based biosensors that we have studied over a period of 14 years in our laboratories.^{33,43,63,57,62,66}

The mechanism by which the *VBR* transduces protein binding remains under investigation. A hypothesis presented here proposes that a target protein permeates the virus-PEDOT layer as it undergoes immunoaffinity-driven partitioning to virus particles entrained in this layer. As the volume fraction of electrically insulating proteins increases, the electrical conductivity of the resistor channel imparted by PEDOT is reduced, generating the *VBR* signal.

3.2 Experimental methods

3.2.1 Materials and methods

Gold electrodes were prepared by photolithography and physical vapor deposition. The following materials and reagents were purchased commercially and used as received: PMMA cells (Wainamics Inc., Fremont CA) and bare gold electrodes were oxygen plasma-cleaned (PDC-32G, Harrick Plasma). PEDOT-PSS (poly(3,4-ethylenedioxythiophene) polystyrene sulfonate) Heraeus Clevious™ PH1000 from Ossila; lithium perchlorate 99+%

purity from Acros organics; EDOT (3,4-ethylenedioxythiophene) from Sigma Aldrich; ethylene glycol from Macron Fine Chemicals. Phosphate buffered saline (PBS, 10x concentrate) from Sigma Aldrich. 1x concentrate of the PBS yielded a phosphate-buffered saline solution at pH 7.4 with a sodium chloride concentration of 0.154 M and a phosphate buffer concentration of 0.01 M. The DJ-1 over-expression plasmid pET3a-His-DJ1 was a gift from Michael J. Fox Foundation, MJFF (Addgene plasmid #51488). DJ-1 was recombinantly overexpressed in *E. coli*. Interleukin 6 (IL-6) was purchased from Tonbo Biosciences. M13 phage library design and procedures for the selection of DJ-1 binders using this library are described in the appendix A.

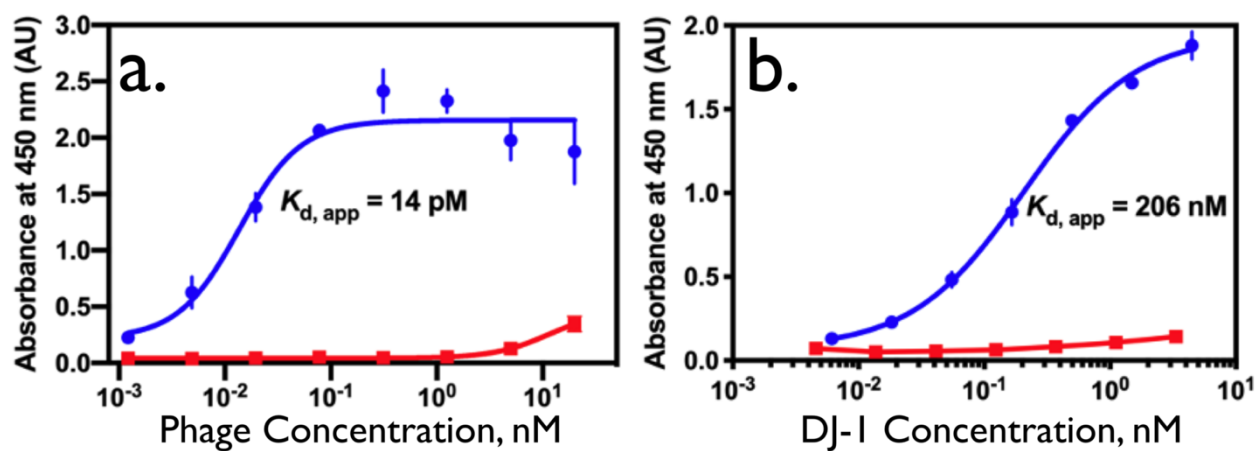


Figure 3.1 Two ELISAs for M13 phage binding of DJ-1: a) Phage ELISA of the DJ-1-binding phage DL-1 and a negative control Stop4 phage. Here, DJ-1 is immobilized and the DL-1 phage is detected. The data were fit with a four-parameter logistic curve fit ($R^2 = 0.9230$). Measurements were performed in triplicate; error bars represent the standard deviation of the mean. b) Sandwich ELISA of DJ-1. In this case, DL-1 phage (or the control Stop4 phage) are immobilized and the DJ-1 protein is detected. This format mimics the function of the VBR. The data were fit as described above ($R^2 = 0.9944$). Measurements were performed in triplicate; error bars represent the standard deviation of the mean.

The affinity of engineered M13 virus particles for DJ-1 can be seen from the results of two enzyme-linked immunosorbent assay (ELISA) measurements (Figure 3.1). The ELISA

measurement was conducted two ways: With DJ-1 adsorbed onto a 96 well plate, measuring the recognition of adsorbed DJ-1 by phage particles in solution (Figure 3.1a), and by adsorbing the phage particles on the plate and measuring the binding of DJ-1 to this virus layer (Figure 3.1b). The latter configuration, which yields a much lower apparent dissociation constant, $K_{d,app}$, more closely resembles that situation relevant to the *VBR*.

3.2.2 *VBR* Fabrication

The fabrication process for the *VBRs* is similar to that described previously⁹⁵ with minor modifications. Briefly, gold-film electrodes were cleaned in an O₂ plasma for 10 min immediately before use. Thick (≈ 70 nm) and thin (≈ 48 nm) PEDOT-PSS films were prepared as follows: thick PEDOT-PSS films were obtained by stirring a solution of 3% (v/v) ethylene glycol with PEDOT-PSS for 30 min. Thin PEDOT-PSS films were obtained by stirring a solution of 1.5% (v/v) ethylene glycol in PEDOT-PSS for 30 min. These solutions were spin-coated on the gold electrodes at 2500 rpm for 80 s and then heated for 1 h at 90 ° C. A PMMA cell was then attached to the PEDOT-PSS film and PEDOT-PSS coated gold electrodes were equilibrated in PBS for 30 min. Next, virus-PEDOT films were electropolymerized onto the PEDOT-PSS/gold-film electrodes using a platinum foil counter and MSE reference electrodes. Virus-PEDOT films were then electrodeposited onto the PEDOT-PSS film from aqueous solutions containing 8 nM M13 bacteriophage, 12.5 mM LiClO₄ and 2.5 mM EDOT by performing two voltammetric scans from 0.2 V to 0.8 V vs. MSE at a scan rate of 20 mV/s. A PARSTAT 2263 controlled by Electrochemistry PowerSuit 2.6 software was used for this deposition. All *VBRs* employed for sensing measurements conformed to the screening

parameters applied at each step of the fabrication process, as described in detail in the SI. For additional detail, see Figure A.1.

3.2.3 Impedance Spectroscopy (IS)

All solutions were prepared and equilibrated at room temperature (20 °C) prior to IS measurements. The *VBR* cell was first rinsed three times with PBS after which impedance measurements were conducted as follows: Background IS measurement (in triplicate) was acquired in urine (synthetic or human) that contained no added protein, and a second IS measurement (again in triplicate) was acquired in the same urine containing added DJ-1 or IL-6 at the indicated concentrations. The difference in Z_{re} between these two measurements at each frequency is ΔR_{VBR} . The two R_{VBR} inputs to ΔR_{VBR} are obtained by fitting an impedance frequency spectrum that spans the range from 1 Hz to 40 kHz. All IS data were acquired using a Princeton Applied Research PARSTAT Model 2263 controlled by Electrochemistry PowerSuit 2.6 software. 50 data points were acquired across a frequency range of 1 Hz to 40 kHz. The amplitude of the applied voltage was 10 mV for all IS measurements. *VBRs* are single use devices. A different *VBR* was therefore used for each measurement. Equivalent circuit fitting was accomplished using EIS Analyzer (ABC Chemistry). Minimization algorithm Powell (300 iterations) was used to generate values for each circuit element.

3.2.4 Time scan experiment

The time scan experiment was performed on four different *VBRs* for four concentrations of DJ-1 protein, 10 pM, 30 pM, 100 pM and 1 nM. Each *VBR* was first equilibrated in synthetic urine for 9 min. A “pure” urine baseline R_{VBR} was then acquired at

$f = 0.1$ Hz for 1.0 min. The synthetic urine was then removed from the PMMA cell and replaced with synthetic urine supplemented with DJ-1 protein at the specified concentration, without disconnecting the *VBR* from the potentiostat. After a one-minute exposure to the test solution, R_{VBR} was again recorded for 10 min.

3.2.5 Control experiments

Three negative control experiments were undertaken to test for signal specificity. In the first, a Stop-4 M13 virus, which has no displayed peptide binding moieties, was substituted for DJ-1-binding phage. The Stop-4 control *VBRs* were exposed to 500 nM DJ-1. Second, *VBRs* containing no phage were exposed to 500 nM DJ-1. Interleukin 6 (IL-6, 20.9 kDa, pI = 6.2) that is similar in size and pI to DJ-1, was used as a third control.

3.2.6 SEM Analysis

Scanning electron microscopy (SEM) data were acquired using a FEI Magellan 400L XHR FE-SEM. An accelerating voltage of 2 keV was used for uncoated films and 10 keV for samples coated with 3 nm of iridium.

3.3 Results and Discussion

3.3.1 *VBR* Fabrication and Characterization.

Starting with patterned gold electrodes on glass (Figure 3.2a), *VBRs* are prepared in three steps (Figure 3.2b). First, a PEDOT-PSS layer is deposited by spin-coating. Second, a poly(methyl methacrylate) or PMMA solution cell with adhesive backing is pressed onto the

PEDOT-PSS layer. Third, this solution cell is used to electrodeposit a virus-PEDOT layer. This electrodeposition process applied the following protocol: The VBR cell is rinsed with PBS buffer and filled with an aqueous solution of EDOT (2.5 mM), LiClO₄ (12.5 mM), and

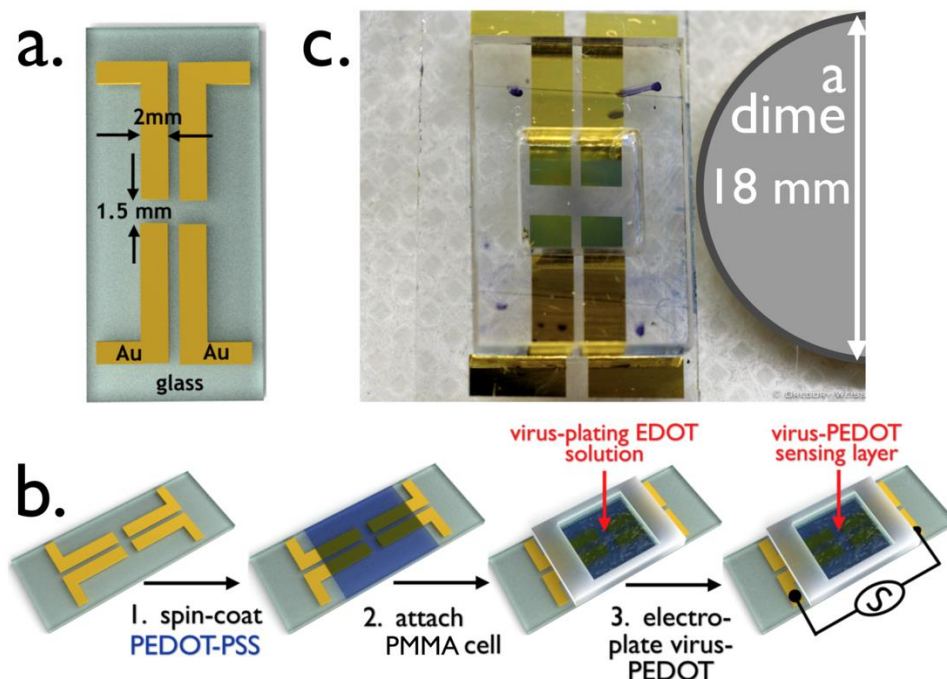


Figure 3.2 The Virus BioResistor (VBR). a) Rendering of gold electrodes for a two-VBR chip showing its dimensions. The two electrodes at left comprise one VBR and the two on the right a second VBR. These two VBRs will share a single bioaffinity layer. b) The three-step process for fabricating a VBR: Step 1 – a conductive PEDOT-PSS base layer is spin-coated onto the gold-on-glass template shown in (a). This film is baked at 90 °C for 60 min; Step 2 – A poly(methylmethacrylate)(PMMA) cell is attached on top of the dried PEDOT-PSS film; Step 3 – the PMMA cell is filled with aqueous EDOT-virus plating solution, and a virus-PEDOT film is deposited by electrooxidation. This VBR biosensor is ready for use. c) Photograph of a two-VBR chip with PMMA solution cell.

engineered M13 virus particles (8 nM). Using a mercurous sulphate reference electrode (MSE), and a platinum counter electrode, the virus-PEDOT composite layer is electrodeposited onto the PEDOT-PSS surface by scanning its potential (20 mV/s) from +0.20 V to +0.80 V and back versus MSE in two cycles (Figure 3.2a, b). Under these

conditions, EDOT is oxidized and the growth of EDOT oligomers proceeds until insoluble cationic PEDOT is precipitated as a film, together with charge-compensating ClO_4^- anions, onto the PEDOT-PSS electrode.⁹⁸ If M13 virus is present in the plating solution, virus particles are incorporated into the growing film, a process promoted by the high negative charge density of these particles. At neutral pH, each M13 virus is blanketed with ≈ 6000 negative charges.⁹⁹ Previously, we have demonstrated that the electrodeposition of films from a plating solution containing M13 virus particles and EDOT produces a composite virus-PEDOT film that concentrates virus particles by a factor of 500 times relative to the M13 concentration in the plating solution.¹⁰⁰ As seen in the photograph of a VBR shown in Figure 3.2c, the resulting VBR “channel”, consisting of a PEDOT-PSS bottom layer and a virus-PEDOT top layer, is transparent.

The VBR device architecture and polymeric channel resembles that of an organic electrochemical transistor (OECT).^{101,102,103,104,105} The differences between these two types of devices are the following: 1). *The VBR is a two-terminal device with no gate electrode.* This simplifies its operation considerably, as the VBR measures the impedance of its channel at its rest potential in the analysis solution without the need for gate scans and the requirement for optimization of the gate potential prior to a measurement.¹⁰⁶ 2). *The VBR measures an impedance frequency spectrum for the channel, typically across five orders of magnitude in frequency instead of the DC resistance of the channel, as is common practice with EOCTs.*^{107,108} This impedance data set allows the channel impedance, R_{VBR} , which provides the VBR signal, to be cleanly separated from the solution impedance, R_{soln} , which is correlated with the salt concentration of the analysis solution.⁹⁵ For bodily fluids such as urine, R_{soln} has the potential to provide information relating to the hydration state of a patient. 3). *VBRs use*

engineered virus particles as receptors. Virus particles may be entrained in a PEDOT film by co-electrodeposition of the virus with the polymer as described above. A fourth difference may be the mechanism of signal generation, as described below.

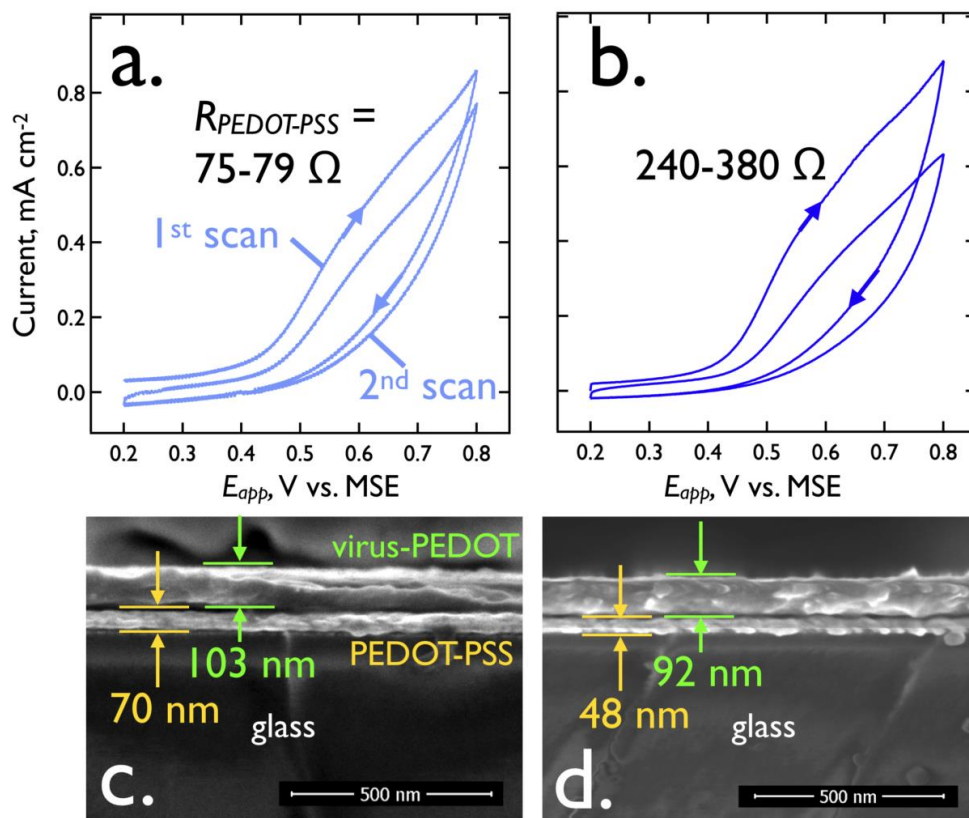


Figure 3.3 Electrodeposition and SEM cross-sections of virus-PEDOT bioaffinity layers. a). A virus-PEDOT bioaffinity layer is electrodeposited on a PEDOT-PSS base layer using two voltametric scans, as shown. The plating solution is aqueous 2.5 mM EDOT and 12.5 mM LiClO₄, 8 nM virus, and the scan rate is 20 mV/s. The DC resistance, $R_{\text{PEDOT-PSS}}$, of the PEDOT-PSS layer here is 75 – 79 Ω . b). Same electrodeposition process for a thinner, PEDOT-PSS base layer with $R_{\text{PEDOT-PSS}}$ in the range from 240 – 380 Ω . c,d). Cross-sectional SEM images of these two layers show that the more conductive PEDOT-PSS layer ($R_{\text{PEDOT-PSS}} = 75 - 79 \Omega$) is 70 nm (± 3 nm) in thickness whereas the less conductive PEDOT-PSS layer is 48 nm (± 2 nm) in thickness. The electrodeposited virus-PEDOT layer is also somewhat thinner in (d) relative to (c) in accordance with the lower deposition currents observed for the second deposition scan.

The architecture and resultant properties of the *VBR* channel dictate its sensing performance. We focus attention here on the importance of the PEDOT-PSS layer thickness and electrical resistance. SEM cross-sectional images (Figure 3.3c, d) show that both polymer layers are tens of nanometers in total thickness. The thickness of the PEDOT-PSS bottom layer is influenced both by the presence of ethylene glycol (EG) in the deposition solution^{109,88} and the spin coater speed. The addition of EG is known to increase the conductivity of PEDOT-PSS by altering its morphology.^{110,111} Relatively thick (70 (\pm 3) nm) low resistance films were obtained using 3% (v/v) EG while high resistance films (48 (\pm 2) nm) were prepared using 1.5% (v/v) EG (Figure 3.3c,d). The electrical resistance of these layers, $R_{PEDOT-PSS}$, is = 75 – 79 Ω (thick) and 240 – 380 Ω (thin). The increased resistance of the PEDOT-PSS bottom layer has little effect on the thickness of the virus-PEDOT top layer electrodeposited on it and the virus-PEDOT top layers had similar thicknesses of 92 (\pm 4) nm (high PEDOT-PSS resistance) versus 103 (\pm 4) nm (low resistance). As we demonstrate below, a reduction in thickness of the PEDOT-PSS layer, and an increase in its resistance, boosts the sensitivity of the *VBR* for the detection of HSA and DJ-1.

Electrodeposited virus-PEDOT and PEDOT-only films have a characteristic topography imparted by PEDOT crystallites protruding by up to a micron from the planar surface of the PEDOT film (Figure 3.4). These “PEDOT stalagmites” are not related to virus particles as they are observed both in the absence (Figure 3.4a, b) and presence (Figure 3.4c, d) of added phage particles. PEDOT stalagmites have attributes of crystallites, including a faceted appearance, as previously reported in the literature.^{112,113} In virus-PEDOT films, entrained M13 virus particles appear as black filamentous objects against a gray PEDOT background (Figure 3.4c,d,e). SEM examination of several samples show that the virus

concentration within the plane of the virus-PEDOT film is nonuniform with $10 \mu\text{m}^2 - 30 \mu\text{m}^2$ regions that are intensely black – indicating high virus concentrations – and other regions

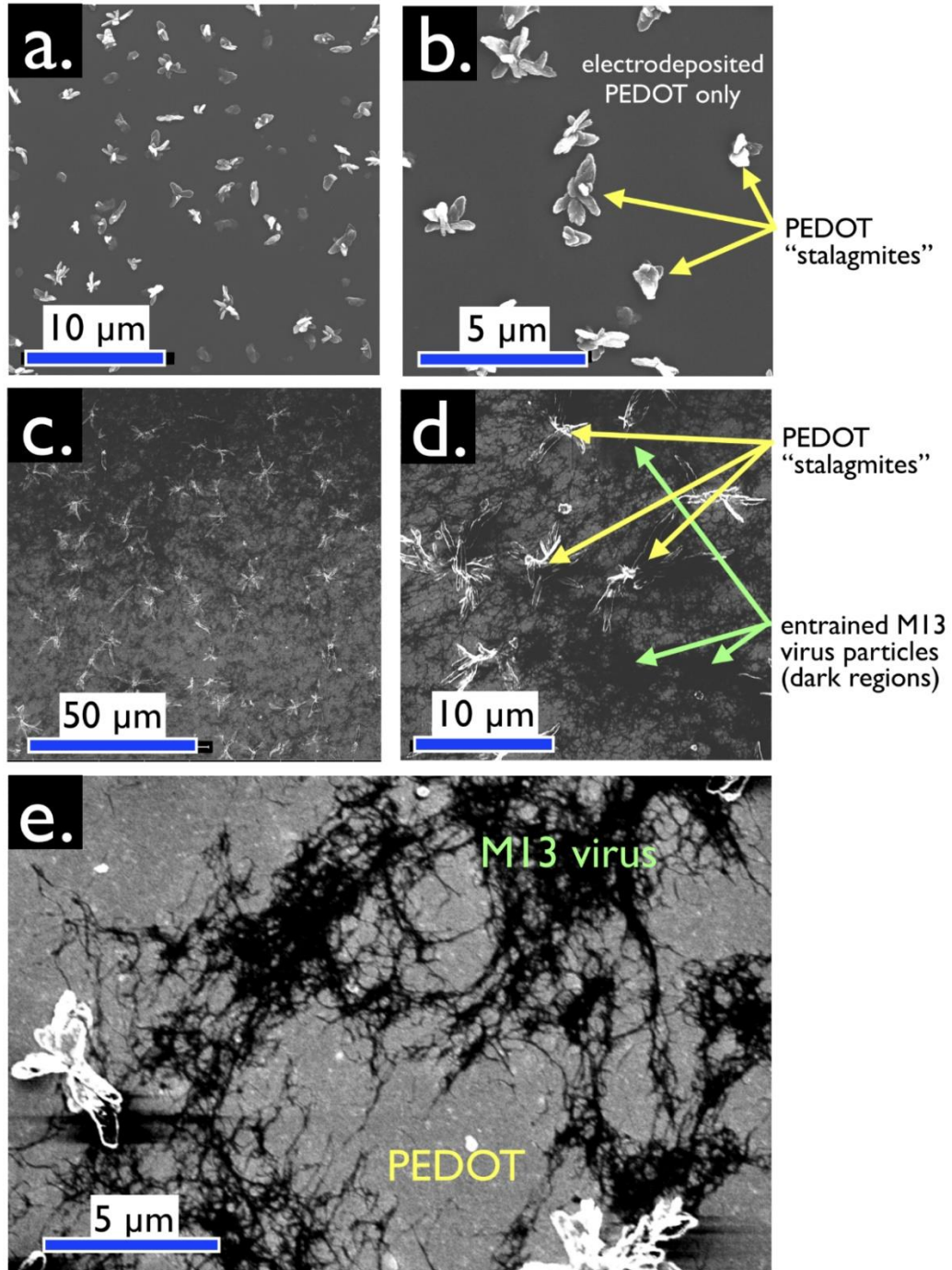


Figure 3.4 Plan-view SEM images, acquired with secondary electron detection (SED), of virus-free (a,b) and virus-containing (c,d,e) bioaffinity layers. (a,b) Control VBR bioaffinity

layer prepared by electrodeposition from a solution containing no virus particles. Micron scale protrusions from the surface of this film are characteristic of electrodeposited PEDOT. These protrusions are not seen at PEDOT-PSS films prepared by spin-coating. We refer to these structures as “PEDOT stalagmites”. (c,d,e) VBR bioaffinity layers containing M13 virus particles. Filamentous M13 virus particles comprise the dark regions of these images. Lighter gray regions contain no virus. PEDOT stalagmites are also observed. Enhanced contrast (e) exposes tangles of M13, again distributed nonuniformly inside a virus-PEDOT bioaffinity layer.

that are gray with a relatively low virus concentration. The clustering of virus particles within the film is interesting and surprising, given the high negative charge density of these particles.

3.3.2 VBR Electrical Response and Signal

As previously proposed⁹⁵, a simple equivalent circuit containing four circuit elements accounts for the measured frequency-dependent impedance of the VBR channel from DC to 40 kHz (Figure 3.5a). In this circuit, the capacitance of the virus-PEDOT/solution interface is represented by a total capacitance, C . This capacitance provides coupling between the AC voltage signal applied to the channel and the analyte solution. Three resistors represent the resistance of the analyte solution (R_{soln}), the resistance of the top polymer layer ($R_{PEDOT-virus}$) and the resistance of the bottom PEDOT-PSS layer ($R_{PEDOT-PSS}$).

The impedance response of a VBR is characterized by a semi-circular Nyquist plot (Z_{im} versus Z_{re} , Figure 3.5b). A qualitative understanding of the VBR response is provided by examining its limiting behaviors at low and high frequencies across the range from 1.0 Hz to 40 kHz. At $f = 1.0$ Hz, the capacitive reactance of the virus-PEDOT/solution interface, ($Z_C =$

$(2\pi fC)^{-1} \approx 6 \text{ k}\Omega$) is larger than R_{VBR} ($\approx 2.1\text{--}2.7 \text{ k}\Omega$, Table 3.1). So, although R_{soln} is small by comparison to R_{VBR} (289–330 Ω), the value of Z_C strongly attenuates the AC signal that accesses R_{soln} . In this limit, R_{VBR} is approximated by the parallel combination of $R_{PEDOT-virus}$ and $R_{PEDOT-PSS}$ (R_{VBR} , Eq. 1).

$$R_{VBR} \approx \frac{(R_{PEDOT-PSS})(R_{PEDOT-virus})}{R_{PEDOT-PSS} + R_{PEDOT-virus}} \quad [1]$$

As shown below and previously,² R_{VBR} increases in the presence of a target protein that is bound by virus particles in the virus-PEDOT layer. The difference between R_{VBR} in the presence and absence of this protein is the VBR signal, ΔR_{VBR} .

At the high frequency limit, $f = 40 \text{ kHz}$, the capacitive reactance approaches zero ($Z_C = (2\pi fC)^{-1} \approx 0.15 \text{ }\Omega$), and the circuit of Figure 3.5a simplifies to three resistors in parallel:

$$R_{VBR} \approx \frac{(R_{PEDOT-PSS})(R_{PEDOT-virus})(R_{soln})}{R_{PEDOT-PSS}R_{PEDOT-virus} + R_{soln}R_{PEDOT-virus} + R_{soln}R_{PEDOT-PSS}} \quad [2]$$

At $f = 40 \text{ kHz}$, R_{VBR} is much lower than at 1 Hz because the small resistor R_{soln} is accessed in parallel to $R_{PEDOT-PSS}$ and $R_{virus-PEDOT}$. To a first approximation, the impedance at both of these frequency limits, 1.0 Hz and 40 kHz, is purely resistive but at intermediate frequencies, a significant capacitive component is introduced, producing the characteristic semicircular Nyquist plot that is observed, as seen in Figure 3.5b.

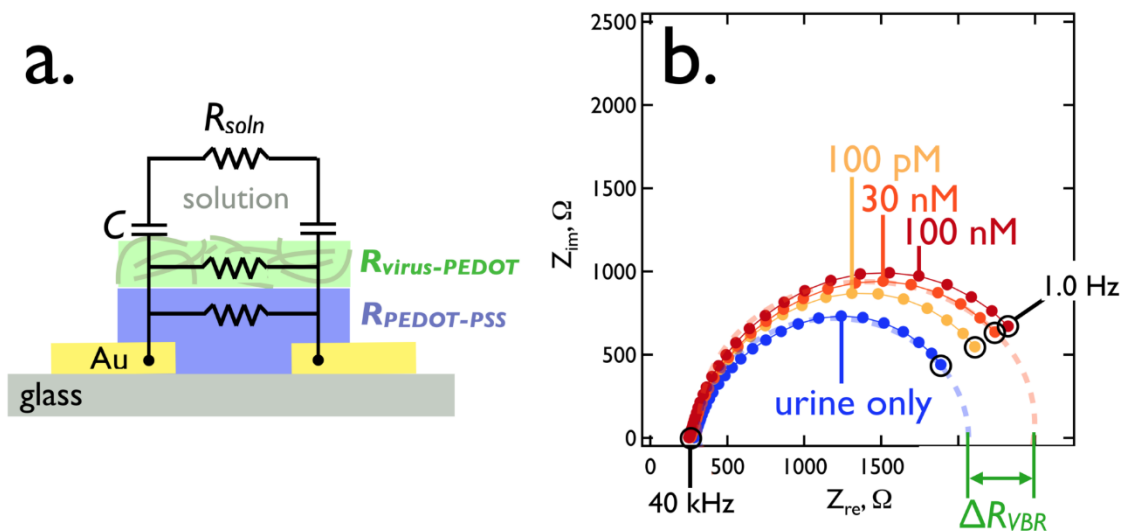


Figure 3.5 The VBR equivalent circuit (a) and a typical impedance response (b). This Nyquist plot (Z_{im} versus Z_{re}) shows the impedance frequency spectrum plotted between 1.0 Hz and 40 kHz for a synthetic urine solution that was supplemented with DJ-1. A single VBR measured these solutions at the indicated DJ-1 concentrations.

The values of C , R_{soln} , and R_{VBR} (encompassing $R_{PEDOT-virus}$ and $R_{PEDOT-PSS}$) are obtained by deconvolution of the complex impedance data set. How do R_{VBR} , R_{soln} , and C , change in response to the concentration of a target protein? For DJ-1 concentrations from 0 – 100 nM, variations of R_{soln} are constant within the error bars for this measurement and are independent of DJ-1 concentration (Table 3.1). The capacitance, C , approximated as a constant phase element (CPE, $Z_C \approx Z_{CPE} = -\frac{1}{Q(i\omega)^n}$), varies weakly with the DJ-1 concentration (Table 3.1). R_{VBR} at low frequency, in contrast, is strongly correlated with the DJ-1 concentration and, as already indicated, ΔR_{VBR} , is used to transduce the concentration of a target protein bound by entrained virus particles (Table 3.1).

Since, as noted above, the VBR signal ΔR_{VBR} is best measured at low frequency, wouldn't it be simpler to use the DC resistance of the VBR channel to derive signal? In practice, the DC measurement does work, but there are two reasons for measuring the frequency spectrum instead: 1). In DC sensing mode, one does not acquire the high frequency impedance (Eq. 2) that permits deconvolution (and measurement) of the solution resistance from the ΔR_{VBR} signal. 2). The reproducibility of the impedance at low frequency is better than for a DC measurement. That is, the signal-to-noise at low frequencies down to 1 Hz is higher than the noise at DC (data not shown).

Table 3.1 VBR circuit element values, and ΔR_{VBR} , corresponding to the Nyquist plots of Figure 3.5b.

	Synthetic Urine		100 pM DJ-1		30 nM DJ-1		100 nM DJ-1	
	Value	Stdev	Value	Stdev	Value	Stdev	Value	Stdev
R_{sol} (Ω)	331	8	288.7	0.9	293	7	279.3	0.2
R_{VBR} (Ω)	2156	1	2436	5	2641	4	2733	8
ΔR_{VBR} (Ω)	0		280		485		577	
^aCPE, Q (F)	2.77 x 10 ⁻⁵	0.03 x 10 ⁻⁵	2.59 x 10 ⁻⁵	0.01 x 10 ⁻⁵	2.65 x 10 ⁻⁵	0.02 x 10 ⁻⁵	2.520 x 10 ⁻⁵	0.009 x 10 ⁻⁵
^aCPE, n	0.84	0.00	0.85	0.00	0.85	0.00	0.86	0.00

^aConstant phase element (CPE) approximation of the capacitance, $C^{114} Z_{CPE} = \frac{1}{Q(i\omega)^n}$. The phase angle, θ , of the impedance response is, $\theta = -(90*n)^\circ$, with $0 > n > 1$. $n = 1$ corresponds to ideal capacitor behavior.

3.3.3. Tuning the *VBR* signal amplitude using $R_{PEDOT-PSS}$.

Eq. [1] predicts that at low frequencies, increasing $R_{PEDOT-PSS}$ causes R_{VBR} to converge on $R_{PEDOT-virus}$ (Figure 3.6a). If ΔR_{VBR} is generated by the virus-PEDOT top-layer, then an increase in $R_{PEDOT-PSS}$ should increase *VBR* sensitivity. This expectation is confirmed by measurement of ΔR_{VBR} for the protein human serum albumin, HSA, a 66.5 kDa protein that is a marker for renal failure (Figure 3.6). A plot of ΔR_{VBR} versus $R_{PEDOT-PSS}$ for [HSA] = 100 nM shows that increasing $R_{PEDOT-PSS}$ is from 70 Ω to 380 Ω by reducing thickness of this layer, increases the ΔR_{VBR} from 40 Ω to more than 500 Ω (Figure 3.6b).

Nyquist plots for three $R_{PEDOT-PSS}$ values (Figure 3.6c, d, e) document the increase in sensitivity for three *VBR*s. It should be noted that $R_{PEDOT-PSS} \approx 300 \Omega$ is a practical upper limit in our experiments. Attempts to further thin the PEDOT-PSS layer to achieve even higher sensitivities resulted in pronounced irreproducibility in both $R_{PEDOT-PSS}$ and measured ΔR_{VBR} values.

Two calibration plots for HSA in PBS buffer solution acquired using *VBR*s compare the performance of high resistance PEDOT-PSS layers, ($R_{PEDOT-PSS} = 260 - 300 \Omega$) with low resistance PEDOT-PSS layers ($R_{PEDOT-PSS} = 80 - 100 \Omega$, Figure 3.6f). The ΔR_{VBR} signal for HSA increases by between 10x (at low concentrations) to 3x (at high concentrations) across the HSA concentration range encompassed by these data.

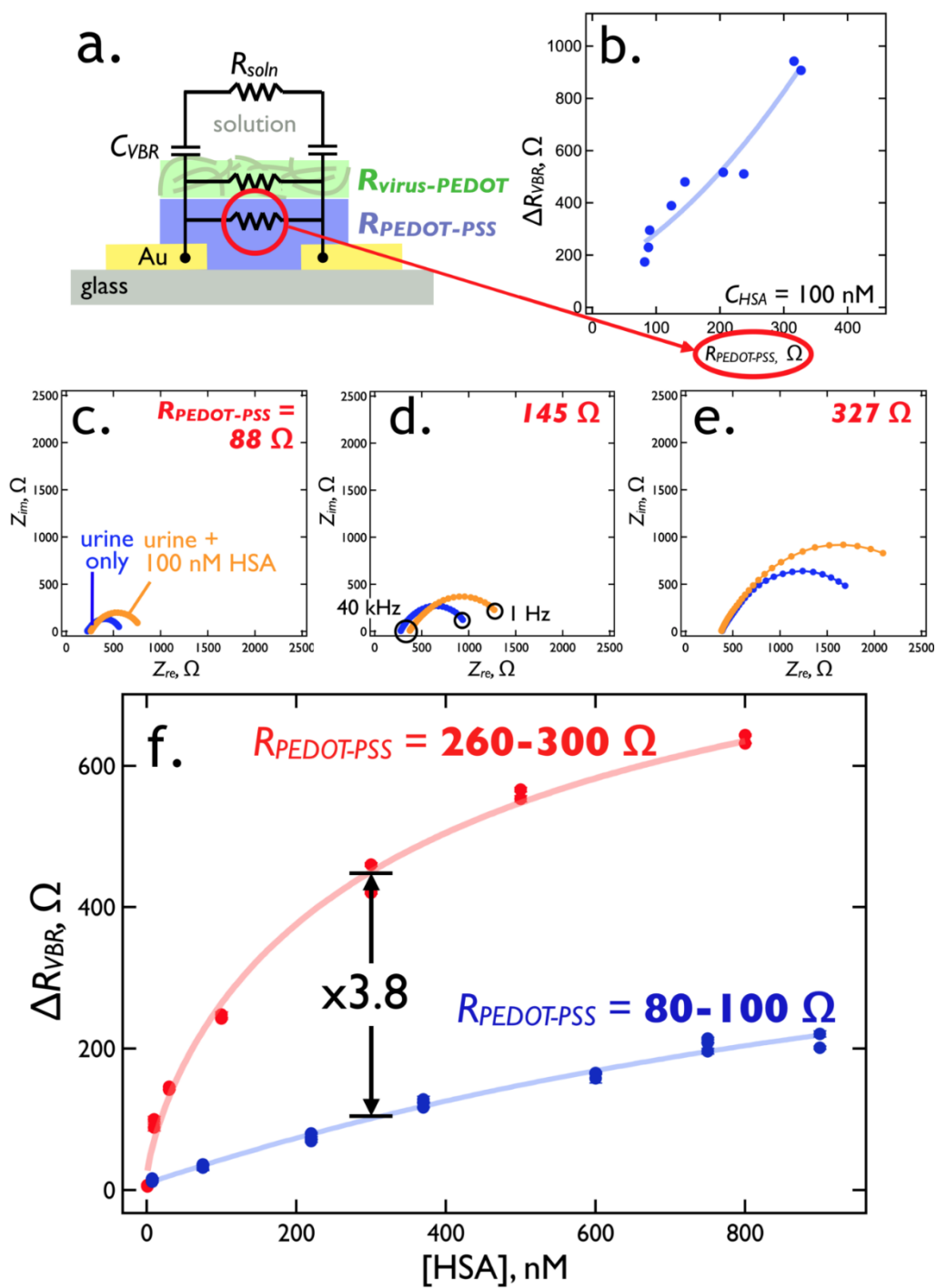


Figure 3.6 RPEDOT-PSS tuning of the VBR sensitivity for HSA. (a). The equivalent circuit for the VBR places the electrical impedance of the virus-PEDOT layer, R_{VBR} , in parallel with that of the PEDOT-PSS bottom layer, $R_{PEDOT-PSS}$, forming a current divider. (b) Increasing $R_{PEDOT-PSS}$ from 80 Ω to 300 Ω , by reducing the PEDOT-PSS layer thickness, forces current, i , through the virus-PEDOT measurement layer, increasing the signal for 100 nM HSA by a factor of 3 to 5 from 200 Ω to more than 900 Ω . (c,d,e) Three Nyquist plots corresponding

to three values of the resistor, RPEDOT-PSS, as indicated. In each plot, impedances are plotted in the complex plane from 1 Hz (right) to 40 kHz (left). A shift in the low frequency Z_{re} from synthetic urine only (blue trace) to 100 nM DJ-1 (orange trace) approximates the signal, ΔR_{VBR} . (f) RVBR versus [HSA] calibration plots for a series of 42 VBR sensors (21 in each plot) with RPEDOT-PSS values in the range from 80 to 100 Ω and 260 to 300 Ω . The higher RPEDOT-PSS devices produce 3 to 5 times more signal amplitude across the HSA binding curve.

$R_{PEDOT-PSS}$ tuning of the VBR sensitivity also works for DJ-1 – a bladder cancer marker that is significantly smaller than HSA (20.8 kDa versus 66.5 kDa). Again, a plot of ΔR_{VBR} versus $R_{PEDOT-PSS}$ for a concentration of DJ-1 of 100 nM in synthetic urine shows that increasing $R_{PEDOT-PSS}$ from 75 Ω to 300 Ω increases ΔR_{VBR} from 50 Ω to 550 Ω (Figure 3.7a). Nyquist plots for three $R_{PEDOT-PSS}$ values (Figure 3.7b, c, d) document the increase in sensitivity for three VBRs.

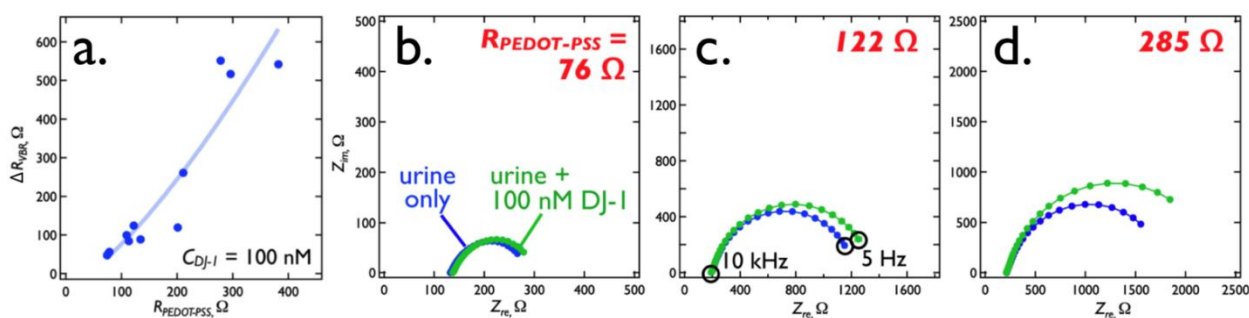


Figure 3.7 RPEDOT-PSS tuning of the VBR sensitivity for DJ-1. (a) Increasing RPEDOT-PSS from 80 Ω to 300 Ω , by reducing the PEDOT-PSS layer thickness increases the signal for 100 nM DJ-1 by a factor of ≈ 10 from 50 Ω to 550 Ω . (b, c, d) Three Nyquist plots corresponding to three values of the resistor, RPEDOT-PSS, as indicated. In each plot, impedances are plotted in the complex plane from 1 Hz (right) to 40 kHz (left). A shift in the low frequency Z_{re} from synthetic urine only (blue trace) to 100 nM DJ-1 (green trace) approximates the signal, ΔR_{VBR} .

Looking more carefully at the DJ-1 sensing performance of VBRs with high resistance PEDOT-PSS layers ($R_{PEDOT-PSS} \approx 300 \Omega$ Nyquist plots (Figure 3.8a, b, c) show the accessible DJ-1 dynamic range extends from a limit-of-detection of 10 pM to 300 nM – a range of more than

four orders of magnitude (see values of all circuit elements for these three VBR sensors in Table 3.2). A plot of ΔR_{VBR} versus DJ-1 concentration across this same range for a total of 35 VBR sensors (Figure 3.8d) conforms to the Hill Equation:⁸⁴

$$\Delta R_{VBR} = \Delta R_{VBR,0} + \frac{\Delta R_{VBR,lim} - \Delta R_{VBR,0}}{1 + \left(\frac{K_D}{[DJ-1]}\right)^h} \quad [3]$$

A best fit of equation [3] to these data yields the following parameter values: $\Delta R_{VBR,lim} = 950 \pm 640 \Omega$, $\Delta R_{VBR,0} = 50 \pm 140 \Omega$, $K_D = 39 \pm 170 \text{ nM}$, $h = 0.3 \pm 0.2$, and $R^2 = 0.94$. It should be noted that these data encompass measurements of DJ-1 in synthetic urine (21 sensors) and in pooled human urine (14 sensors). Each of these VBRs was used for a single DJ-1

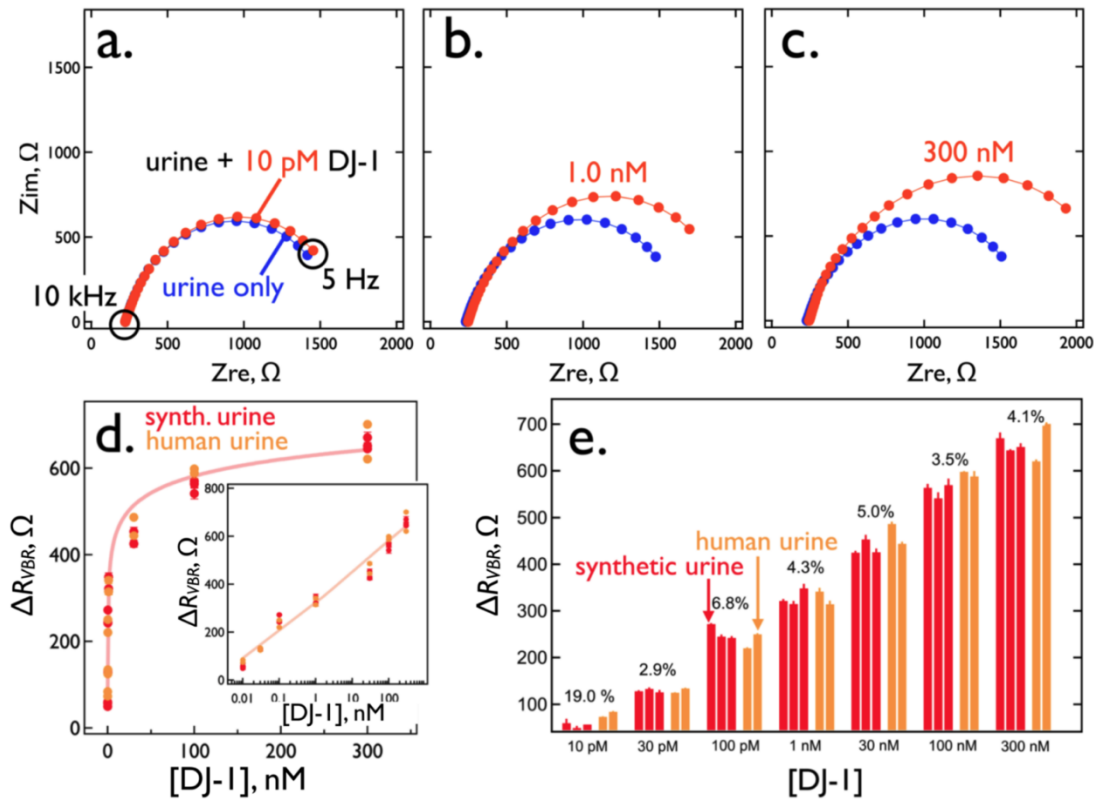


Figure 3.8 DJ-1 sensing performance using VBRs with RPEDOT-PSS = 280 to 300 Ω . (a, b, c) Nyquist plots for three DJ-1 concentrations of (a) 10 pM, (b) 1 nM, and (c) 300 nM. Also

shown (blue traces) are background Nyquist responses in synthetic urine only. (d) A calibration curve for the detection of DJ-1 using the RVBR signal constructed using 21 individual measurements from the same number of VBRs, at seven concentrations. Values of K_D and h (the Hill exponent) obtained from a best fit of the experimental data to equation (2), are indicated. (e) Bar plot for ΔR_{VBR} measurements acquired from 21 electrodes, illustrating the sensor-to-sensor reproducibility of these data. CoVs for these data, shown, are in the 2 to 8% range across four orders of magnitude in DJ-1 concentration. The values of each of the circuit elements is indicated in Table 3.2.

concentration data point in Figure 3.8d. The measured value of h indicates strong negative cooperativity, meaning that the microscopic dissociation constant, K_D , is increased (the affinity interaction is reduced) as the fraction of binding sites occupied by the target protein increases.⁸⁴ This has the effect of stretching the binding curve across a wider range of DJ-1 concentration range – exceeding four orders of magnitude in the present case (Figure 3.8d).

Table 3.2 VBR circuit elemental values corresponding to the Nyquist plots of Figure 3.8a-c.

Fig 8a	Synthetic Urine		10 pM DJ-1	
	Value	Stdev	Value	Stdev
R_{sol} (Ω)	338.5	0.2	333.6	0.7
$R1$ (Ω)	1097	4	1136	8
C_{VBR} (F)	1.040×10^{-5}	4×10^{-8}	1.010×10^{-5}	5×10^{-8}
R_{VBR} (Ω)	1617	2	1674	2
CPE, Q (F)	2.570×10^{-5}	5×10^{-8}	2.54×10^{-5}	2×10^{-7}
CPE, n	0.85	0.00	0.85	0.00
Fig 8b	Synthetic Urine		1 nM DJ-1	
	Value	Stdev	Value	Stdev
R_{sol} (Ω)	331.7	0.4	333.6	0.1
$R1$ (Ω)	1490	2	1823	6
C_{VBR} (F)	8.70×10^{-6}	2×10^{-8}	8.610×10^{-6}	8×10^{-9}

R_{VBR} (Ω)	1663.3	0.4		2010	10
CPE, Q (F)	2.380 x 10 ⁻⁵	9 x 10 ⁻⁸		2.53 x 10 ⁻⁵	3 x 10 ⁻⁷
CPE, n	0.86	0.00		0.86	0.00
Fig 8c					
	Synthetic Urine			300 nM DJ-1	
	Value	Stdev		Value	Stdev
R_{sol} (Ω)	304.5	0.1		275	1
R1 (Ω)	2550	20		4110	50
C_{VBR} (F)	8.49 x 10 ⁻⁶	5 x 10 ⁻⁸		6.99 x 10 ⁻⁶	9 x 10 ⁻⁸
R_{VBR} (Ω)	1983	5		2634	3
CPE, Q (F)	2.66 x 10 ⁻⁵	1 x 10 ⁻⁷		2.78 x 10 ⁻⁵	2 x 10 ⁻⁷
CPE, n	0.86	0.00		0.86	0.00

In principle, the absence of a gate and an applied gate potential referenced to an external reference electrode, leaves open the possibility of potential drift of the channel that could drive doping and de-doping reactions of the PEDOT sensing layers, causing baseline drift of the sensor and degrading reproducibility of the concentration measurements. But the data of Figure 3.8e shows that this “channel conductivity drift” is inconsequential on the time scale of 1-2 minutes required for carrying out VBR measurements of concentration. To this end, we made measurements of DJ-1 conducted in triplicate (for synthetic urine) and duplicate (for human urine) document the reproducibility of VBRs (Figure 3.8e). Sensor-to-sensor coefficients-of-variation (CoV) vary from 2.9% (30 pM), to 4.1% (300 nM), extraordinarily low values. As expected, at the 10 pM LOD, a higher CoV of 19% is obtained. It should be noted that VBRs are effectively single use devices, because the off-rate for bound DJ-1 after a single exposure is several hours (data not shown). This means that individual

VBRs cannot be calibrated; every *VBR* sensor must respond to the same calibration curve placing a premium on the sensor-to-sensor reproducibility.

Nonspecific adsorption at the unmodified virus-PEDOT surface of a *VBR* is negligible, contributing to the simplicity of *VBR* fabrication (Figure 3.9b). Blocking, often accomplished by pre-equilibrating a bioaffinity layer with solutions of bovine serum albumin (BSA), casein,^{115, 116, 117} or poly (ethylene glycol),¹¹⁸ prior to exposure to a target protein, is not required. Three sets of negative controls (Figure 3.9a) for *VBRs* containing no phage, *VBRs* prepared using Stop-4 phage (which has no displayed peptides at its surface), and *VBRs* prepared using DJ-1 binding phage in the presence of Interleukin 6 or IL-6 (a protein of similar size, 20.9 kDa, and pI, 6.2 versus 6.7 for DJ-1) - either produce no measurable signal or a small “negative” signal, corresponding to a negative value of ΔR_{VBR} (Figure 3.9a).

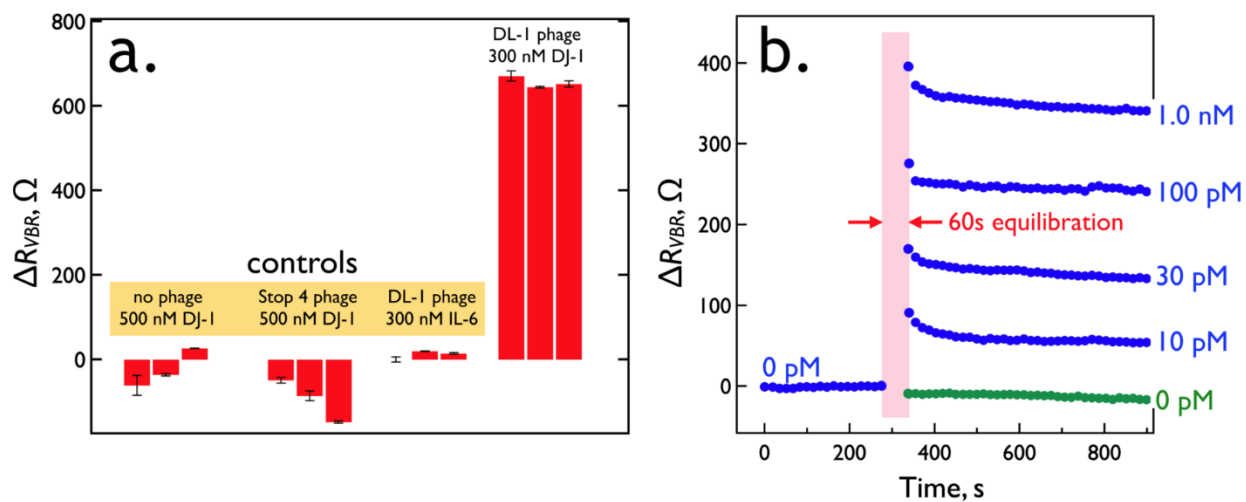


Figure 3.9 VBR specificity and speed. (a) Three control experiments: At left is the response of three VBRs prepared with no phage exposed to 500 nM DJ-1. To the right of this is the response of three VBRs prepared with Stop-4 phage that has no displayed peptides on its surface. Finally, at right are shown the results of three VBRs containing DL1 phage (selected for the binding to DJ-1) upon exposure to IL-6, a protein of similar MW (20.9 kDa) and pI (6.2) to DJ-1 (20.7 kDa and pI of 6.7, respectively). (b) Real-time VBR sensing data.

Responses for five VBR sensors are shown for DJ-1 exposures of 0 pM (green trace), 10 pM, 30 pM, 100 pM, and 1.0 nM. These traces were obtained by first stabilizing sensors in synthetic urine for 9 min, measuring a RVBR baseline at 0.10 Hz, and then interrupting for 1.0 min while the synthetic urine was replaced with synthetic urine supplemented with DJ-1 at the specified concentration, after which ΔR_{VBR} signal was acquired.

Analysis speed and simplicity of operation are two requirements for biosensors that are used either at the point-of-care (PoC) or outside a care facility, at a point-of-need (PoN).^{119,120} The VBR provides for detection of DJ-1 across a range of concentrations within one minute in a dip-and-read modality (Figure 3.9b). Thus, the VBR is well-adapted to PoC and PoN applications.

The frequency-dependent signal-to-noise ratio (S/N) for the VBR (Figure 3.10a) increases with decreasing frequency from 40 kHz to 1.0 Hz. In this measurement, noise is

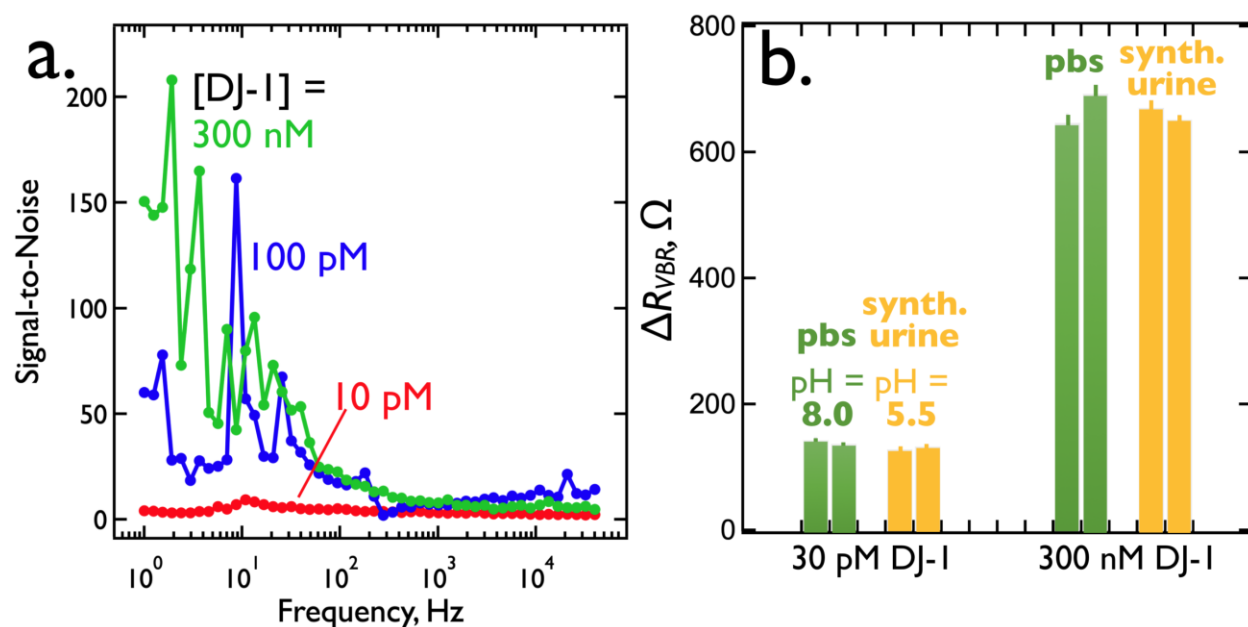


Figure 3.10 (a) Signal-to-noise (S/N) versus frequency for the detection of DJ-1. Shown are three plots of S/N versus frequency measured for three VBRs immersed in three DJ-1-spiked synthetic urine solutions containing DJ-1 at the indicated concentrations. Noise is calculated

as the standard deviation of three replicate measurements at each frequency. S/N consistently increases from high to low frequencies. (b) Comparison of ΔR_{VBR} for the detection of DJ-1 in two electrolytes: synthetic urine (pH = 5.5) and PBS buffer (pH = 8.0). The charge state of DJ-1 (pI = 6.7) inverts across this pH difference and is negatively charged at pH = 8.0 and positively charged at pH = 5.5. However, ΔR_{VBR} at two different concentrations are the same, despite changes in pH, within the reproducibility of these measurements.

defined as the standard deviation of repetitive measurements ($N = 3$) for ΔR_{VBR} (the signal) at a defined concentration of target protein. At a DJ-1 concentration of 300 nM, S/N peaks at 150 at 1.0 Hz and decreases to 60 at 100 pM and 4 at 10 pM, the limit-of-detection. S/N ratios at 40 kHz, in contrast, are in the range from 2 to 14 for this range of DJ-1 concentration. Consistent with the equivalent circuit of Figure 3.5a, increasing frequency reduces the impedance of the virus-PEDOT solution capacitance, Z_C , opening a low impedance path through the analyte solution, R_{soln} , and by-passing the signal-generating current path of the channel. It should be noted that the S/N versus frequency data sets (Figure 3.10a) are themselves noisy. Repeated measurements of these data show that the sharp peaks and valleys seen in these traces are not reproduced. This means that there are temporal variations in the noise present in the VBR circuit. However, the trend of increasing S/N with decreasing frequency remains prominent in these data.

3.3.4. A proposed mechanism for VBR signal generation

The mechanism by which the VBR produces an impedance increase in the presence of target protein is of interest. This mechanism must account for three experimental observations: 1). ΔR_{VBR} is positive. In particular, the sign of the protein charge, positive or

negative, has no influence on the signal. For example, DJ-1 ($pI = 6.7$) can be measured both at $pH = 5.5$ and at 8.0 , corresponding to a positively charged protein, and a negatively charged protein, respectively (Figure 3.10b). ΔR_{VBR} signal is unaffected by this charge inversion. 2). **VBR signal is insensitive to the salt concentration of the test solution.** Previously,⁹⁵ we demonstrated this for the detection of 75 nM HSA in salt solutions ranging from 134 mM to 670 mM NaCl where no significant change in HSA signal was observed. Collectively, (1) and (2) imply that a charge gating mechanism, responsible for signal in field-effect transistors,¹²¹ cannot be operating in VBRs. 3) The signal-to-noise ratio is strongly frequency dependent - S/N is high at low frequency (≈ 1 Hz) and near zero at high frequency (≈ 40 kHz) where it is also independent of the concentration of a target protein. The implication is that **the signal generating process does not require the transmission of AC signal through electrolyte.** This includes electrolyte that is present in the voids within the porous virus-PEDOT signal-generating layer. Thus, R_{VBR} decreases by just 24 Ω or 4% (against a background of 600 Ω) in protein-free aqueous NaCl as C_{NaCl} is increased by a factor of 50 from 0.02 M to 1.00 M (Figure A.2).

A simple mechanism that may account for these observations is shown schematically in Figure 3.11. Here, just the virus-PEDOT layer is illustrated. The virus-PEDOT layer itself is semi-crystalline, containing crystalline PEDOT-only domains surrounded by disordered domains that contain disordered PEDOT chains and, likely, most of the virus particles (Figure 3.11a). Electrical conduction within this layer occurs by two processes: i) intrachain charge transport (via bipolarons) and, ii) interchain electron hopping (Figure 3.11a). Interchain hopping, in particular, can be disrupted by the partitioning of protein into this layer,

promoted by the immunoaffinity partitioning of target protein by virus particles entrained in the virus-PEDOT film.¹²²

This mechanism is analogous to that proposed for chemiresistive gas sensors that exploit a carbon/polymer composite chemiresistor.^{123,124,125,126,127} In these systems, permeation of a carbon/polymer (insulating) composite by a molecule in the vapor phase causes an increase in the volume of the composite and a decrease in the volume fraction of the conducting carbon phase, leading to a reduction in the conductivity of the composite, a process that is described by percolation theory:^{128,129}

$$\sigma = \sigma_0[V - V_c]^\alpha \quad [4]$$

Where σ_0 is the conductivity of the composite in the absence of permeating vapor species, σ is the conductivity of the composite after exposure to this vapor, V is the volume fraction of the conductive component of the composite, V_c is the volume fraction of the conductive phase at the percolation threshold, and α is a scaling exponent that depends only on the dimensionality of the percolation process (2 dimensional or 3 dimensional). Eq (4) is intended to model the conductivity at values of V near the percolation threshold, but more generally, it provides a signal transduction mechanism for chemiresistors in which the resistor is comprised of a nonconductive and a conductive component and for which permeation of analyte(s) induces swelling of this system.

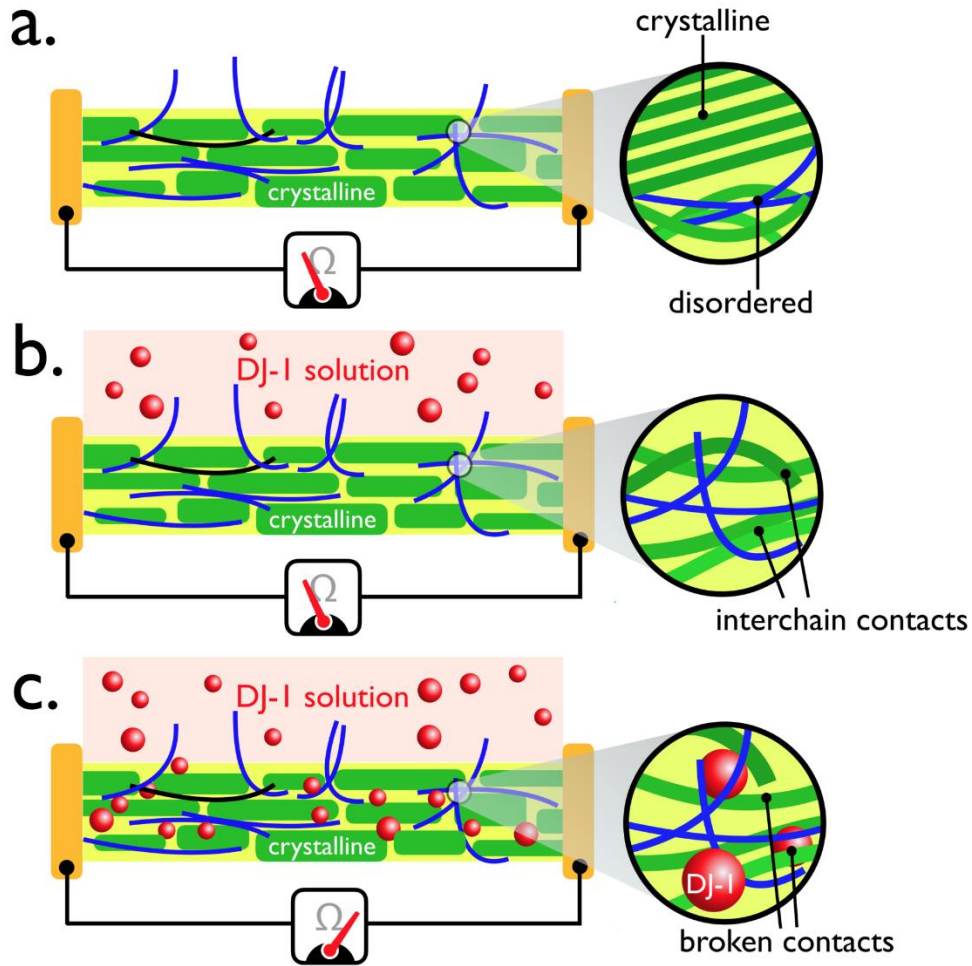


Figure 3.11 Schematic representation of a hypothesized signal transduction mechanism for the VBR. (a) The virus-PEDOT layer shown here consists of semi-crystalline PEDOT with virus particles that are concentrated within disordered regions of the PEDOT layer, (b) When exposed to the DJ-1 protein solution, ΔR_{VBR} is initially zero, because an induction time is associated with the rate-limiting diffusion of the protein into the virus-PEDOT layer. (c) Permeation of the virus-PEDOT layer by DJ-1 is associated with an increase in its resistance as the insulating protein interferes with conduction pathways within this layer.

The mechanism depicted (Figure 3.11) requires that target protein diffuses into the virus-PEDOT layer. Does this occur on the one-minute time-scale of signal generation, and if so, what mass loading of protein is obtained in this layer during this brief period? These questions can be addressed using quartz crystal microbalance (QCM) gravimetry. In this

measurement, a two-layer PEDOT-PSS + virus-PEDOT bioaffinity layer is prepared on a QCM crystal coated with a thin photoresist layer. Exactly the same processes used for *VBR* fabrication (Figure 3.12a), involving the PVD deposition of gold electrodes, spin-coating of the PEDOT-PSS layer, and electrodeposition of the virus-PEDOT layer, are used for the preparation of these layers, for these experiments, the gold electrodes are not used to make electrical measurements.

Upon exposure to DJ-1 solutions, the resonant frequency, f_r , decreases within seconds and stabilizes within ≈ 40 -60 s (Figure 3.12b) Using the Sauerbrey Equation¹³⁰ the observed frequency change, Δf , can be translated into a mass change, Δm :

$$\Delta f = -\frac{f_r}{\rho_q d A} \Delta m \quad [5]$$

where f_r is the resonant frequency of the quartz crystal oscillator in air, ρ_q , is the density of this crystal, d is its thickness, and A is the area of the gold electrodes deposited onto this crystal.

A plot of Δm versus DJ-1 concentration shows saturation behavior resembling the *VBR* calibration plot for DJ-1 (Figure 3.8d). The mass loading saturates at $\approx 4 \mu\text{g}/\text{cm}^2$ which corresponds to more than 1.0 monolayer of DJ-1 at the surface of the virus-PEDOT layer - even if this layer has significant roughness. For purposes of comparison, the mass of a hydrated protein monolayers has been measured using QCM for several proteins including RNAase (13.7 kDa, 300 ng/cm² on silica), bovine serum albumen (66.5 kDa, 150 ng/cm² on silica)¹³¹, and human serum albumin (66.5 kDa, 230 ng/cm² on oxidized gold).¹³² An estimate of the mass of a closest packed DJ-1 monolayer can also be derived from the dimensions of

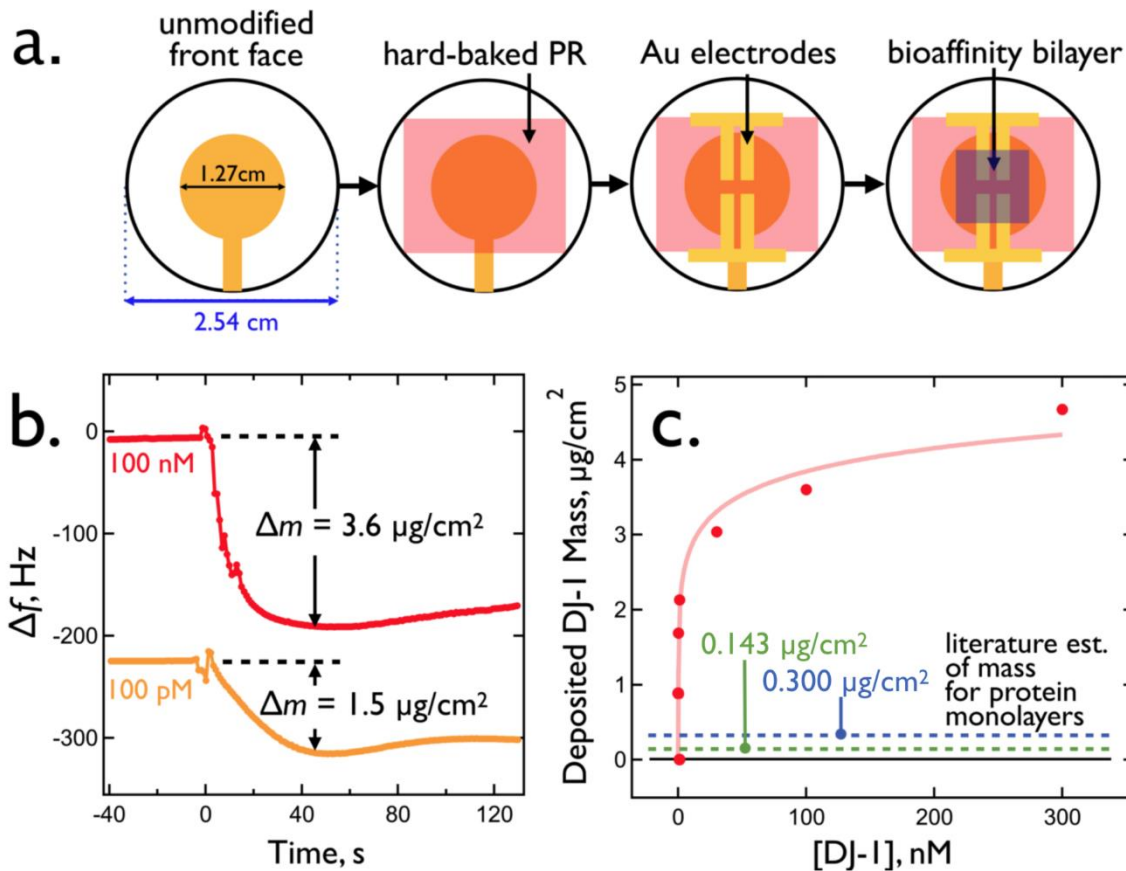


Figure 3.12 Measurement of DJ-1 mass loading for VBR bioaffinity layers using quartz crystal microbalance (QCM) gravimetry. (a) Four step fabrication of a complete VBR bioaffinity layer on a commercial QCM crystal. (b) Change in frequency, Δf , versus time for the exposure of two VBRs to solutions of DJ-1 at 100 pM and 100 nM. The measured DJ-1 mass loading is indicated, and traces are shifted along the Δf axis for clarity. (c) The concentration of DJ-1 versus its measured mass loading. This isotherm was acquired in PBS buffer solution.

this protein previously reported using single crystal x-ray diffraction¹³³. The refined crystallographic data includes 323 structural water molecules per DJ-1 protein, which should be considered a lower bound to the actual water content of this system. The mass of this monolayer is predicted to be 146 ng/cm². The low end (146 ng/cm²) and high end of these estimates (300 ng/cm²) are indicated by dashed lines in Figure 3.12c. Based upon these numbers, the $\approx 4 \mu\text{g}/\text{cm}^2$ plateau measured for DJ-1 corresponds to 13-27 equivalent

protein monolayers. These data are consistent with permeation of DJ-1 into the virus-PEDOT layer, and perhaps the PEDOT-PSS layer as well, on the one-minute time scale as required by the mechanism depicted in Figure 3.11.

Finally, it is useful to confirm that the diffusion coefficient, D_{DJ-1} , required for DJ-1 permeation by diffusion in one minute is physically realistic. D_{DJ-1} can be estimated using the equation:¹³⁴ $D_{DJ-1} = T^2/2t$ where T is the total thickness of the two-layer channel ($\approx 150 - 170$ nm) and t is the time required for diffusive permeation of DJ-1 (≈ 60 s) which we estimate as the time required for signal generation. The range of calculated D_{DJ-1} values is $(1.9 - 2.4) \times 10^{-12}$ cm²/s, which is approximately 5-6 orders of magnitude slower than the diffusion coefficient for proteins of this size ($D \approx 10^{-7} - 10^{-6}$ cm²/s)¹³² in aqueous electrolyte solutions, qualitatively as expected. Potentially, the estimates of T , derived from SEM data (Figure 3.3), could be too low because these values pertain to dried films. However, doubling the estimate of T ($\approx 300 - 340$ nm) produces D_{DJ-1} values of $(7.5 - 9.6) \times 10^{-12}$ cm²/s within an order of magnitude of the dried values.

To test the signal transduction mechanism for VBRs proposed here, simultaneous measurements of the electrical impedance and direct QCM measurements of the mass loading of protein, are required for comparison with the predictions of Eq. [4]. We expect to carry out these measurements soon.

3.4 Summary

The *VBR* is a biosensor that exploits direct electrical communication with virus particles to measure the concentration of protein biomarkers for cancer and disease. These

virus particles, which are engineered to recognize and bind a target protein of interest, are entrained within an electrodeposited virus-PEDOT film. The electrical impedance of this film directly produces the signal required for protein quantitation, eliminating the need for any additional amplification. In addition, no reagents such as redox couples are required for these measurements.

The conductive polymer bilayer comprising the *VBR* channel can be engineered to adjust its sensitivity. In particular, a reduction in the thickness of the PEDOT-PSS bottom layer from 70 nm to 48 nm significantly increases the resistance of this layer, from $\approx 80 \Omega$ to $\approx 300 \Omega$ increasing the *VBR* signal for HSA (66.5 kDa) by a factor of 3x to 10x. Applying this strategy to the detection of a smaller protein, DJ-1 (20.8 kDa) enables the measurement of this bladder cancer marker at concentrations down to 10 pM using a measurement time of 1.0 min. in a dip-and-read modality. The extreme simplicity of the *VBR* allows for its fabrication in three steps, contributing to excellent sensor-to-sensor reproducibility characterized by CoVs below 7% down to 30 pM for DJ-1, across the entire DJ-1 binding curve spanning four orders of magnitude in concentration.

Direct *QCM* measurement of the mass of the bioaffinity bilayer demonstrates that the equivalent of multiple (>10) monolayers of DJ-1 protein are able to diffuse into this layer from solution within one minute, a process that coincides temporally with the generation of the *VBR* impedance signal. The resulting *QCM* binding curve for DJ-1 resembles the binding curve measured by the *VBR* for this protein. Based upon this observation as well as other evidence, a simple model is proposed for signal transduction involving the dilution of the PEDOT conductor by insulating protein molecules resulting in an increased resistance for

this layer, a mechanism analogous to that operating in carbon/polymer chemiresistor gas sensors.

Chapter 4

Oxidized *VBR* for detecting antibodies

4.1 Introduction

The conventional antibody detection is based on ELISA (enzyme linked immunosorbent assay) and MIA (multiplex immunoassay) that rely on lengthy immune-complexing reactions probed by fluorescence measurement. The involvement of expensive confocal system and lab expertise amongst other factors, limits its application to widespread testing. Antibodies are unquestionably an important type of detection marker. Antibodies are produced as a first line of defense against antigens for many human diseases be it oncological, inflammatory, neurological or psychiatric disorders. Quantification of antibodies is not only critical indicator of disease diagnosis and progression,¹³⁵ but it is also helpful in assessing toxicity during drug treatment and tracking efficiency of drug delivery.¹³⁶ A very relatable example, is the COVID pandemic, wherein reliable tests available for diagnosis are based on time consuming, lab exclusive techniques, that can be performed by specialized individuals. The alternative techniques that get commercialized quickly for rapid testing are mostly qualitative. This situation is not helpful especially when the progress and severity of the disease can be correlated with the amounts of antibodies in the body fluid.

Electrochemical immunosensors were created aiming to overcome the drawbacks of conventional antibody testing systems. This work introduces a modified version of *VBR* that is sensitive to anti-bodies. Like the conventional *VBR*, the bioaffinity matrix consists of M13 phage particles co-electrodeposited with PEDOT polymer. M13 phage-based detection of antibodies has been reported in the group with anti-M13 antibody detection limits 20 nM – 300 nM^{33,56,137}. Ionescu et. al. reported amperometric immunosensor for the detection of West Nile virus IgG. Mixture of pyrrole monomer and T7 phage were adsorbed onto glassy carbon disc, followed by electropolymerization. After incubation with a secondary

peroxidase-labeled antibody, the immunosensors were applied to quantitative amperometric detection of antibody with LOD 36 pg/mL in 50 minutes.¹³⁸ To the best of our knowledge, these are the only phage based biosensors for antibodies reported in literature. Most of the current immunosensors employ DNA, aptamers, antigens, antibodies as recognition moieties. Compared to these, the phage production is relatively easy, cheap and these particles can make durable biosensors. The compatibility of phage with *VBR* has been showcased in the previous chapters.

Table 4.1 summarizes electrochemical immunosensors that detect antibodies with impressive limits of detection (LOD). To yield such low LOD, these sensors involve complex and lengthy fabrication procedures. For example, sensors that employ traditional antigen-antibody interaction followed by antigen/antibody labeled with electrochemical indicator, involve long incubation time ranging from 30 minutes to hours. Immobilization techniques like adsorption might be very routine and successful but their applicability to robust sensors is challenged by (a) undesired orientation and probability of desorption due to weak bonds or leaching out in presence of proteins with high charge or number of hydrophobic pockets (b) less dense surface coverage leading to contamination (c) conformational decreased bioactivity with time.¹³⁹ Many crosslinker mediated immobilization depend on generating groups like sulfhydryl/aldehyde groups require aggressive conditions that can produce unwanted reactions and affect binding ability.¹⁴⁰ Addition of electrochemical reaction mediators or enzymatic label tagging elevates the probability with the variability of biomolecule coupling reaction. Multiple washing steps involved compromises with ultimate simple and one-step sensing goal of POC devices. In addition, every other immunosensor based on assembling various biorecognition layers requires an extra step to verify

biomolecule loading, for example observing increased R_{ct} to track the progress of self-assembled monolayer formation on bare electrode^{141,142}. With *VBR*, a few of the above problems have been addressed. Being in its initial stage for antibody detection, a lot of lessons can be learnt from the qualities of the existing sensors and applied to augment the future of *VBR* in antibody sensing.

The previous chapter demonstrated signal enhancing strategy wherein the signal was pushed through the top PEDOT:virus layer upon increasing the resistance of the base PEDOT:PSS layer. In general, it was observed that increased resistance increased the sensitivity of the film and aided signal enhancement. It was also observed that beyond a particular PEDOT-PSS film resistance, the sensor couldn't retain its semi-circle and data procured beyond a particular baseline resistance of 380 ohm did not follow a specific trend.⁶⁴

Protein with molecular weights 20.8 kDa and 66 kDa have been successfully detected with *VBR*. However, detecting antibodies takes a step further to clinical relevance and is a challenge for electrochemical sensors. Using C2 phage and anti-FLAG antibody as model system, the *VBR* was tested for the detection of anti-body anti-FLAG but could not yield reliable signals for various dilutions tested. The need for a different morphology and a possibly resistive sensor could be a solution. Literature reports interesting analytical, sensing and biomedical applications of conducting polymers in different oxidation states. These films were fabricated by applying potential for defined amount of time or charge deposited or fabricating films potentiodynamically. The oxidation of polymers was first studied in polypyrrole. Interest in CP as overoxidized film arose after sensing applications were reported^{143,144,145,146}. The molecular sieve properties of these films were deployed for

hydrazine, dopamine and to exclusively detect uric acid and epinephrine in the presence of UA ascorbic acid^{147,148}. The definition of overoxidation is blurry. It usually involves the application of anodic potential that causes appreciable degradation of electrochemical properties, depending on the synthesis conditions/route of the polymer, the substrate for growth, the electrolyte type and concentration, thickness of the film under investigation.

The effect of oxidation has been summarized by Ujjvari et. Al¹⁴⁹

(a) stress generation in oxidized film (b) crack formation due to internal stress (c) residual products from degraded polymer leave the layer (d) film stress relieved after formation of the cracks (e) partial delamination of the polymer layer resulting in exposure of underlying metal substrate to the electrolyte solution

PEDOT in its oxidized form has served as cation selective emitter and collector in conductive-polymer based ion bipolar junction transistors¹⁵⁰ and for detecting perchlorate ions¹⁵¹, lead ion¹⁵². An overoxidized poly(3,4-ethylenedioxythiophene) film-modified screen-printed carbon electrodes (SPCE/PEDOT_{ox}) successfully detected sub-micromolar concentration of dopamine without the coexisting interferences of ascorbic acid (1000-fold) and uric acid (10-fold)^{153,154}. Following this lead, PEDOT was degraded potentiostatically in a controlled fashion to explore the sensing ability of the oxidized film.

Table 4.1 Electrochemical immunosensors for antibody detection

Antibody detected	Immunosensor bioaffinity layer	Technique	Range	LOD	Ref.
Bovine IgG	Bismuth film-modified nylon membrane-foldable SPCE	Anodic stripping voltammetry/SWV	0-5 $\mu\text{g mL}^{-1}$	0.02 $\mu\text{g mL}^{-1}$	155
Anti-tTG IgG	Anti-humanIgG labeled CdSe/ZnS QD	DPV	0-40 U ml-1	2.2 U ml-1	156
Anti-tTG IgG	Au-dithiol-tTG SAM	Amperometry	0-10 $\mu\text{g/mL}$	390 ng/mL	141
Anti tTG IgA and Anti-tTG IgG	SPCE nanostructured with CNT and AuNP	CV to monitor anodic dissolution of enzymatically generated silver.	0-120 U ml-1	0.53 U ml-1 0.47 U ml-1 Saturation achieved at 40 U ml-1	157
Anti-Hantavirus antibody	SAM of MPA (3-mercaptopropionic acid), (HNp) bound to electrode via EDC/NHS modified surface.	EIS	NA	0.4-300 $\mu\text{g/mL}^{-1}$	158
Digoxin antibodies	thiol-modified hairpin DNA structure labeled with ferrocene bound to an electrode	DPV	1.0-500 pg/mL	0.4 pg/mL	142
Zika virus antibodies	Envelope protein domain III and non-structural protein 1 immobilized on activated carbon SPE	EIS and SWV		53 fg/mL for EDIII 17 fg/mL for NS1	159
CSP antibody	Antigen immobilized on CNT	EIS	17 fg/mL 95.9 fg/mL	17 fg/mL	160
GAD antibody	GAD antigen immobilized on	EIS	0.02 - 2 ng/mL	Pico molar range 48 pg/mL	161

	carboxylated graphene				
HIV ab	Epitope gp41 attached to PNA sequence hybridized to 21 bp DNA signaling strand	Amperometric	1-100 nM	10 nM10min	162
IgE for allergic reaction	Horse IgG3 immobilized on SPE Chitosan film via crosslinking glutaraldehyde	Amperometric	1/300 - 1/1800 dilution	0.5 pg/mL	163
Anti BSA	Pentacene based organic thin film transistor. BSA as catcher probe	OFET	50-1000 nM	50 nM	164
Anti-hepatitis C virus	Dual affinity yeast bio-bricks	CV	0-1000 nM	2 nM	165

*For most works reported in AU ml-1 and compared with ELISA kits are difficult to compare with this work and hence the analytical characteristics of those sensor are not easily comparable.

Abbreviations: tTG = transglutaminase; BSA = bovine serum albumin; AuNP= gold nanoparticles; SPE = screen printed electrode; HIV = human immunodeficiency virus; OFET = organic field effect transistor; GAD = Glutamic acid decarboxylase; CSP = circumsporozoite protein; MPA = 3-mercaptopropionic acid; SAM = self-assembled monolayer; SPCE = screen printed carbon electrode; SWV = Square wave voltammetry; CNT = carbon nanotubes; DPV = differential pulse voltammetry; CV = Cyclic voltammetry

4.2 Experimental Methods

4.2.1 Antibodies and reagents:

MONOCLONAL ANTI-FLAG M2 (produced in mouse) was purchased from creative diagnostics, stock concentration 0.283 mg/mL. C2 phage was prepared in a collaborating lab, Weiss lab. Gold electrodes were prepared by photolithography and physical vapor deposition. The following materials and reagents were purchased commercially and used as

received: PMMA cells (Wainamics Inc., Fremont CA) and bare gold electrodes were oxygen plasma-cleaned (PDC-32G, Harrick Plasma). PEDOT-PSS (poly(3,4-ethylenedioxythiophene) polystyrene sulfonate) Heraeus Clevios™ PH1000 from Ossila; lithium perchlorate 99+% purity from Acros organics; EDOT (3,4-ethylenedioxythiophene) from Sigma Aldrich; ethylene glycol from Macron Fine Chemicals. Phosphate buffered saline (PBS, 10x concentrate) from Sigma Aldrich. 1x concentrate of the PBS yielded a phosphate-buffered saline solution at pH 7.4 with a sodium chloride concentration of 0.154 M and a phosphate buffer concentration of 0.01 M. Human serum S100 was purchased from Sigma Aldrich.

4.2.2 VBR Fabrication

The fabrication process for the *VBRs* is similar to that described in section 3.2.2. Briefly, gold-film electrodes were cleaned in an O₂ plasma for 10 min immediately before use. PEDOT-PSS thickness \approx 270 nm was spin-coated on the gold electrodes at 2500 rpm for 80 s and then heated for 1 h at 90 °C. A PMMA cell was then attached to the PEDOT-PSS film and PEDOT-PSS coated gold electrodes were equilibrated in PBS for 30 min. Next, virus-PEDOT films were electropolymerized onto the PEDOT-PSS/gold-film electrodes using a platinum foil counter and MSE reference electrodes. Potential values mentioned in the text are against MSE unless mentioned otherwise. Virus-PEDOT films were then electrodeposited onto the PEDOT-PSS film from aqueous solutions containing 8 nM M13 bacteriophage, 12.5 mM LiClO₄ and 2.5 mM EDOT by performing two voltammetry scans from 0.2 V to 0.8 V at a scan rate of 20 mV/s. After deposition, the films were oxidized with 12.5 mM LiClO₄ solution, holding the potential at 0.8 V for desired time. A PARSTAT 2263 controlled by

Electrochemistry PowerSuit 2.6 software was used for deposition and oxidation of bioaffinity layer.

4.2.3 Impedance Spectroscopy (IS)

All solutions were prepared and equilibrated at room temperature (20 °C) prior to IS measurements. The *VBR* cell was first rinsed three times with PBS after which impedance measurements were conducted as follows: Background IS measurement (in triplicate) was acquired in PBS without antibody, and a second IS measurement (again in triplicate) was acquired in antibody solution prepared with PBS resulting in indicated concentrations. The sensor was equilibrated for 20 minutes in both PBS and antibody solutions. The difference in Z_{re} between these two measurements at each frequency is ΔR_{VBR} . The two R_{VBR} inputs to ΔR_{VBR} were obtained by fitting an impedance frequency spectrum that spans the range from 1 Hz to 40 kHz. All IS data were acquired using a Princeton Applied Research PARSTAT Model 2263 controlled by Electrochemistry PowerSuit 2.6 software. 50 data points were acquired across a frequency range of 1 Hz to 40 kHz. The amplitude of the applied voltage was 10 mV for all IS measurements. *VBRs* are single use devices. A different *VBR* was therefore used for each measurement. Equivalent circuit fitting was accomplished using EIS Analyzer (ABC Chemistry). Minimization algorithm Powell (300 iterations) was used to generate values for each circuit element.

4.2.4 Control experiments

To test the specificity of the signal, four negative controls were acquired. Background signals were acquired for PEDOT films without phage and with Stop4- M13 virus, with no

displayed peptide binding moieties and tested against 556 ng/mL anti-FLAG. Two antibodies anti-DL1 and anti-GFP (556 ng/mL) was tested for signal with C2 loaded PEDOT film.

4.2.5 SEM Analysis

Scanning electron microscopy (SEM) data were acquired using a FEI Magellan 400L XHR FE-SEM. An accelerating voltage of 2 keV was used for uncoated films and 10 keV for samples coated with 3 nm of iridium.

4.3 Results and Discussion

4.3.1 Fabrication of *VBR*

The fabrication of *VBR* followed the strict screening parameters mentioned in Figure A.1. Appreciating the utility of screening parameters, it is hard to overlook the importance of electrochemical entrapment of phage into the sensor. This method has proved to promote formation of polymeric layer with controlled thickness, constituting a reproducible and non-manual procedure for biosensor fabrication.¹⁶⁶ As opposed to multi-step antibody sensor fabrication, *VBR* fabricates the bioaffinity layer in one step. While techniques like EIS and CV ascertain the bioaffinity layer formation in most sensors, *VBR* reports phage loading while being electropolymerized. The anodic current for second scan significantly is reduced as compared to a scan without phage. With an anodic current of 300 μA , the second scan is expected to land around 200 μA . This observation was supported by SEM wherein phage loading was found to be abundant when *VBR* is constructed with restricted parameters as compared to *VBRs* with anodic current separation lower than 60 - 100 μA . The electrodeposition of bioaffinity layer was followed by the oxidation of *VBR* (figure 4.1a),

performed via two routes. 1) Chronoamperometric method (CA): A potential of 0.8 V was applied for different time limits to sensors filled with 12.5 mM LiClO_4 (figure 4.1b). CA50 and CA100 refer to CA experiment performed at 0.8 V for 50 seconds and 100 seconds respectively. 2) A cyclic voltammetry was performed in 12.5 mM LiClO_4 0.8 V - 1 V at 20mV/s scan rate. This method is referred to as potentiodynamic method, hereafter (figure 4.1c). The color of the film changes from light blue to transparent upon oxidation, an effect which has been observed previously.¹⁶⁷

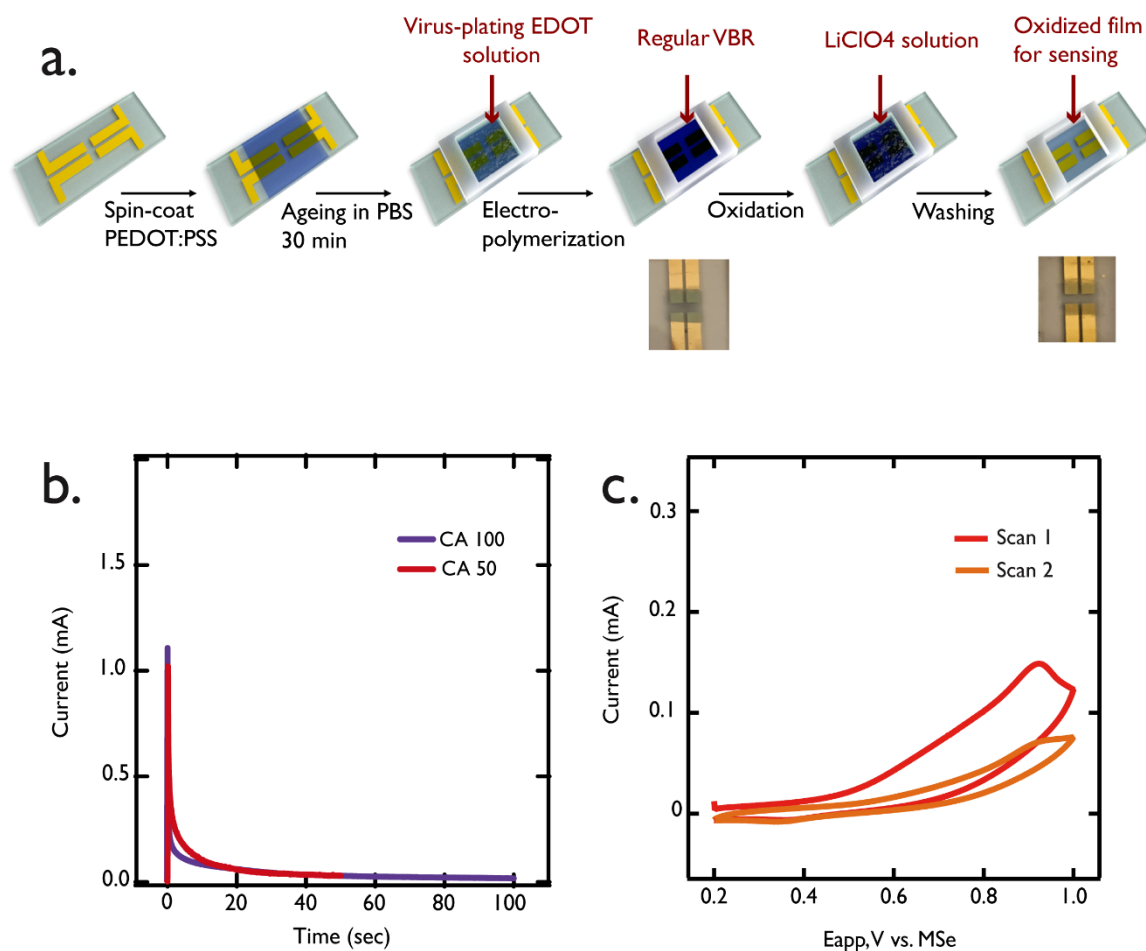


Figure 4.1 Fabrication of VBR (a) Schematic cartoon of VBR fabrication. The regular film fabrication follows the procedure mentioned in section A.2. Thereafter, the cell is filled with 12.5 mM LiClO_4 solution and oxidized. The oxidized film appears transparent as compared

to the regular PEDOT film. Images of regular VBR and oxidized VBR are placed right below their respective cartoons. (b) Chronoamperometric method of oxidation holds the potential 0.8 V vs MSE for different time points, example for 50 seconds (CA50) and 100 seconds CA100, depicted in the figure. (c) Potentiodynamic method involves sweeping the potential from 0.2 to 1 V vs MSE for two cycles at 20 mV/s.

4.3.2 Optimization of oxidation method: CA vs potentiodynamic oxidation

Oxidation methods reported in the literature constitutes two popular routes that were tested with *VBR*. A potentiodynamic scan exceeding the deposition oxidation potential was chosen to over-oxidize the pre-deposited Virus-PEDOT films. When 7 different *VBR* chips were over-oxidized potentiodynamically, an inconsistent baseline measurement (figure 4.2 a) was recorded accompanied by film delamination in 90% of the sensors tested for this method. This treatment might work well for thick films but failed to fabricate reproducible sensor baselines.¹⁶⁸ Another observation was the inconsistent position of the oxidation peak which happens to be an indicative of deactivation of conducting polymer films.¹⁶⁹ As opposed to this observation, when films were subjected to oxidation at a constant potential of 0.8 V for two time points 50 seconds and 100 seconds, films were able to retain the semi-circle and remained intact on the electrode surface (figure 4.2 b). It is important to mention that the films were also tested at a high potential of 1 V for various time limits ranging from 30 seconds to 120 seconds. CA performed at 1 V can be considered as a harsh treatment for these PEDOT:virus films. Two observations were prominent for oxidation at 1 V. The films would either rupture upon oxidation or a double semi-circle Nyquist representative of the formation of two different interface on the sensor was observed. Overall effect of oxidation can be summarized as increased resistance^{170,171} and decrease in the low frequency capacitance.¹⁷² It is evident from figure 4.2c that oxidation treatment

tremendously increased the resistance of the PEDOT:virus film. The film resistance increased from regular $\sim 1.5 \text{ k}\Omega$ to $\sim 8 \text{ k}\Omega$ for CA50 and $15 \text{ k}\Omega$ for CA100. Prolonged oxidation has two possible effects: Conjugation length is shortened as electrons are drawn from the π bond of the PEDOT backbone or overall shortening of polymer backbone due to degradation of the backbone.¹⁶⁸

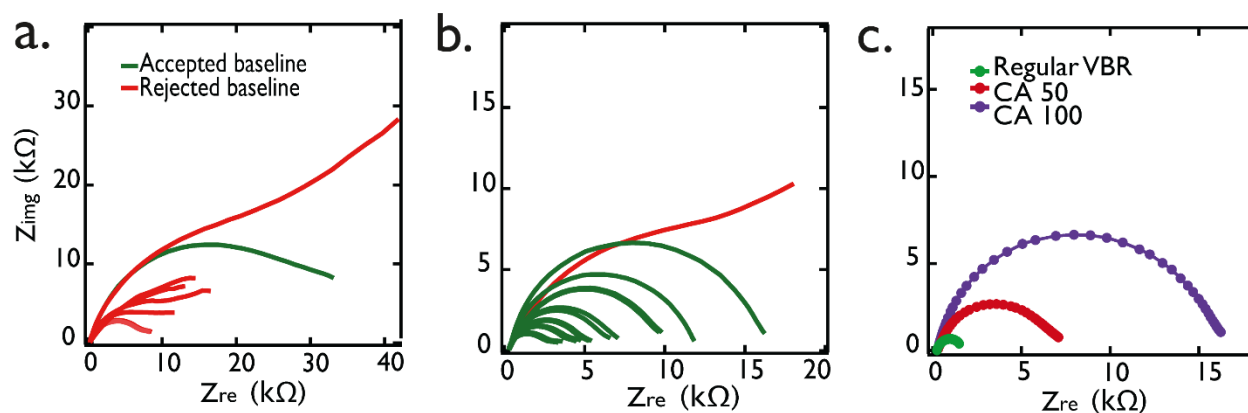


Figure 4.2 The Nyquist plots for oxidized films. The overall effect of oxidation can be recognized as increased resistance of the bioaffinity films. Each film tested contains the virus particles to include the effect of uneven surface that results from virus loading (a) Increased resistance is depicted from regular VBR. Higher the time limit for oxidation, higher is the resistance. (b) The baseline Nyquist for 7 devices is presented. The loss of semi-circle is accounted for stripping of bioaffinity layer from the gold electrode. (c) The higher success rate obtained for CA oxidation for 50 and 100 seconds. 10 out of 11 devices tested retained their semi-circle and the films didn't delaminate.

4.3.3 Detection of DJ1 protein for sensor optimization

The new device configuration was first tested with DJ1 marker, to assess the effect of oxidation treatment on sensing abilities of VBR. Three important observations can be summarized. (1) Approximately tenfold signal enhancement was observed for 4 concentrations of DJ1 marker tested, figure 4.3a (2) The background signal increased with

increased signal detection. The control experiments yielded $\sim 200 \Omega$ background as opposed to $\sim 20 \Omega$ for the regular *VBR*, figure 4.3b (3) The equilibration time increased from 10 minutes (reported for regular *VBR*) to 20 minutes for both baseline and protein detection.

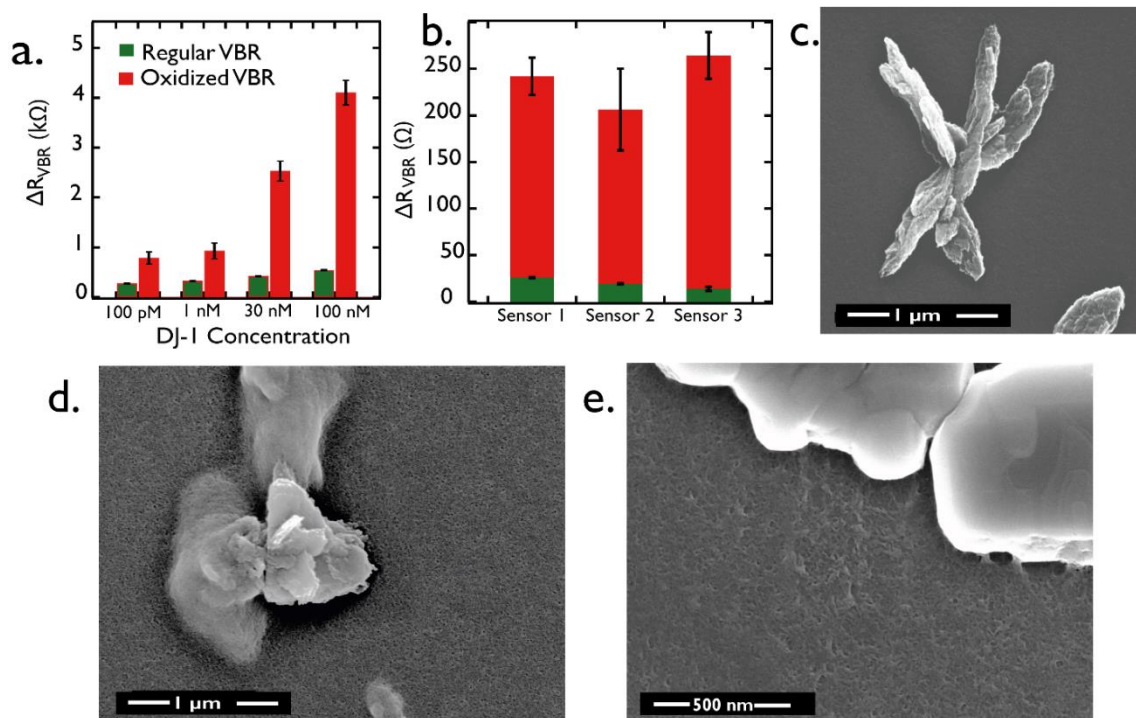


Figure 4.3 (a) Comparing signals for 100 nM DJ1 from regular and oxidized VBR for 4 different concentrations. The signals were averaged from three devices, the error bars represent the standard deviation for three devices. (b) Highest signals from three control sensors were compared with the highest background obtained for oxidized sensors. The orange bar stacked upon green bar is the extra background signal generated for the oxidized VBR. (c) Plan view SEM for sputtered sample of regular PEDOT film. The surface appears to be smooth compared to (d) oxidized VBR, wherein pores are visible, and surface appears to be rough. (e) A magnified image of oxidized film. Oxidized films retain the PEDOT stalagmites from the regular film without any significant change of structure.

The SEM images for the oxidized film displayed a porous structure as compared to the non-oxidized film. PEDOT and polypyrrole based biosensors have described the role played by porous oxidized films for selective cation-anion sensing and exclusion of huge

undesirable biomolecules. By adjusting the oxidation conditions, the size of the pores can be tuned to desirable application. For *VBR*, detecting proteins up to 66 kDa (HSA) was established successfully but larger biomolecules were never tested. If larger biomolecules couldn't penetrate the bioaffinity layer, the introduction of porous film would help generate signals from the *VBRs*.

4.3.4 Antibody detection with oxidized *VBR*

With the above observations in place, there were, one regular and two oxidized configurations awaiting to be tested for antibody detection. The N-terminus of the C2 peptide carried a FLAG-tag (seq: DYKDDDDK). The FLAG-tag is an artificially synthesized peptide that binds specifically binds an anti-FLAG IgG antibody. Regular films loaded with C2 phage poorly detected the antibody in question and failed to follow a meaningful trend on increasing the concentration of antibody, accompanied with appreciable irreproducibility. Films oxidized at 0.8 V 50 secs displayed some activity for two concentrations of anti-FLAG but was limited to detecting the same. On the other hand, films oxidized at 0.8 V 100 secs worked best for detecting anti-FLAG in the range 0.88 $\mu\text{g}/\text{mL}$ 0.93 $\mu\text{g}/\text{mL}$. Oxidized films based on polypyrrole mentions the importance of increased porosity of their glucose sensor that enables diffusion into the matrix and access the active sites of the enzyme loaded in their sensor.^{173,174,175,152} Similar effect may explain why antibody sensing activates only beyond a certain morphological change has been induced by oxidation for 100 secs. More porous structure might allow for more antibodies to percolate through the film. Secondly, it is also possible that the polymeric structure of PEDOT might be distorted enough for easy

accommodation of big antibody biomolecules. Microscopic characterization of the oxidized phage incorporated films ascertained that virus particle distribution was not hampered by the oxidation treatment of the bioaffinity layer. Though the SEM imaging hints about virus distribution on the surface, the XPS depth profiling studies are in progress. Initial data (not shown here) suggests the presence of phage upto nm deep into the film. It makes sense, as QCM experiments back up the mechanism that involves the protein to seep into the PEDOT film in order to distort the electrical contacts. On the same note, had most of the sensing signal been extracted from the surface, antibody detection shouldn't be difficult with regular *VBR*.

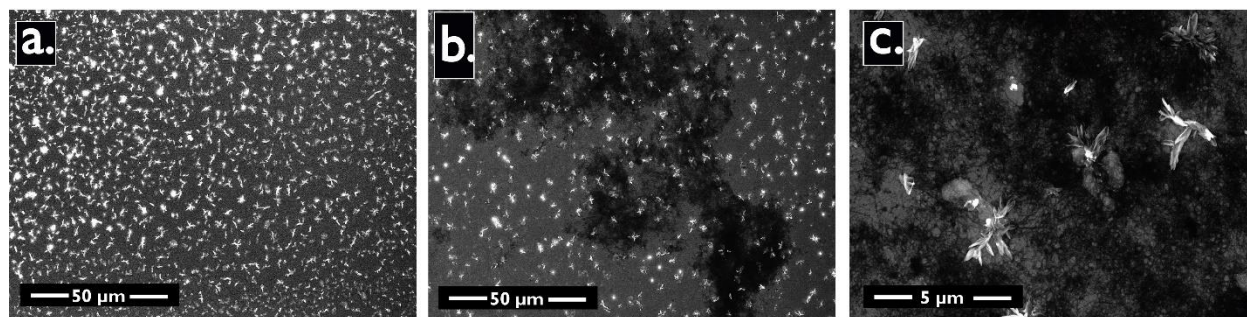


Figure 4.4 Plan view SEM for (a) oxidized PEDOT films without virus particles incorporated (b) Oxidized PEDOT:virus films at the same magnification as (a), confirming the presence of dense phage particles that remain on the film despite oxidation treatment. This clarifies that phage loading remains unaffected during the treatment. The non-uniform distribution of the virus particles is evident in this image (c) magnified image of PEDOT:virus film.

Two Nyquist plots are presented for low concentration and high concentration anti-FLAG detection. The limit of detection of this sensor for anti-FLAG is 188 ng/mL. The Nyquist for antibody detection were recorded after 20 minutes of equilibration with antibody solution. The sensor retained its ability to maintain a low coefficient of variation (<13 %), for the 20 sensors tested. The signals obtained in these experiments are extracted directly

from the bioaffinity film and do not require any additional amplification. The background signal was slightly higher ($\sim 450 \Omega$) compared to than that obtained for CA50 sensor configuration. This bolsters the assumption that prolonged oxidation treatment leads to more permeability of the molecules. This modification undoubtedly yields higher signals but also invites high background signal. This observation, however, does not affect the capability of the sensor to cleanly distinguish between the control and analyte of interest. A certain background defines the lowest acceptable signal and also specifies the limit of detection. Four control experiments were performed to validate the signal originated only from the specific interactions of the anti-FLAG antibody with C2 phage (figure 4.3d). The first control studied the response of polymer itself without any phage towards a high anti-FLAG concentration, 556 ng/mL (blue bars). This helps assess the signal generated from the interaction of the antibody of interest with the polymeric film. The second control (maroon bars) assesses the effect added by phage body lacking specific epitope for sensing anti-FLAG (556 ng/mL). The last two controls tested the C2 loaded sensor's non-specificity towards two antibodies (both 556 ng/mL), anti-DL1 represented by orange bars and anti-GFP (green fluorescent protein) represented by green bars.

It would be interesting to study if the limit of detection for DJ1 biomarker is lowered with this sensor configuration. If the LOD is not changed, it might simply imply the role played by the availability of binding sites on the phage and its affinity towards the analyte. For example, HSA and DJ1 both displayed different LOD, also, their apparent K_d available from ELISA data proved that the affinity for the target analyte was different for both L3 phage and DL1 phage, possibly accounting for different limits of detection. Therefore, the scope of improvement of limit of detection should be investigated with another phage and antibody

combination bearing better affinity than the current phage-antibody. A plot of ΔR_{VBR} versus anti-FLAG concentration across this same range for a total of 20 VBR sensors (Figure 4.3e) conforms to the Hill Equation:⁸⁴

$$\Delta R_{VBR} = \Delta R_{VBR,0} + \frac{\Delta R_{VBR,lim} - \Delta R_{VBR,0}}{1 + \left(\frac{K_D}{[\text{anti-FLAG}]} - 1\right)^h} \quad 176$$

The Hill fit to the calibration curve yields the following values:

$\Delta R_{VBR,lim} = 8131.3 \pm 299 \Omega$, $\Delta R_{VBR,0} = 823.61 \pm 212 \Omega$, $K_D = 393.69 \pm 9.28 \text{ ng/mL}$, $h = 6.3746 \pm 0.775$, and $R^2 = 0.94$. The high hill coefficient may be attributed to the homotropic positive cooperativity displayed by antibodies.¹⁷⁷ It could also be a result of contributions from the avidity effect of epitope-antibody interaction.

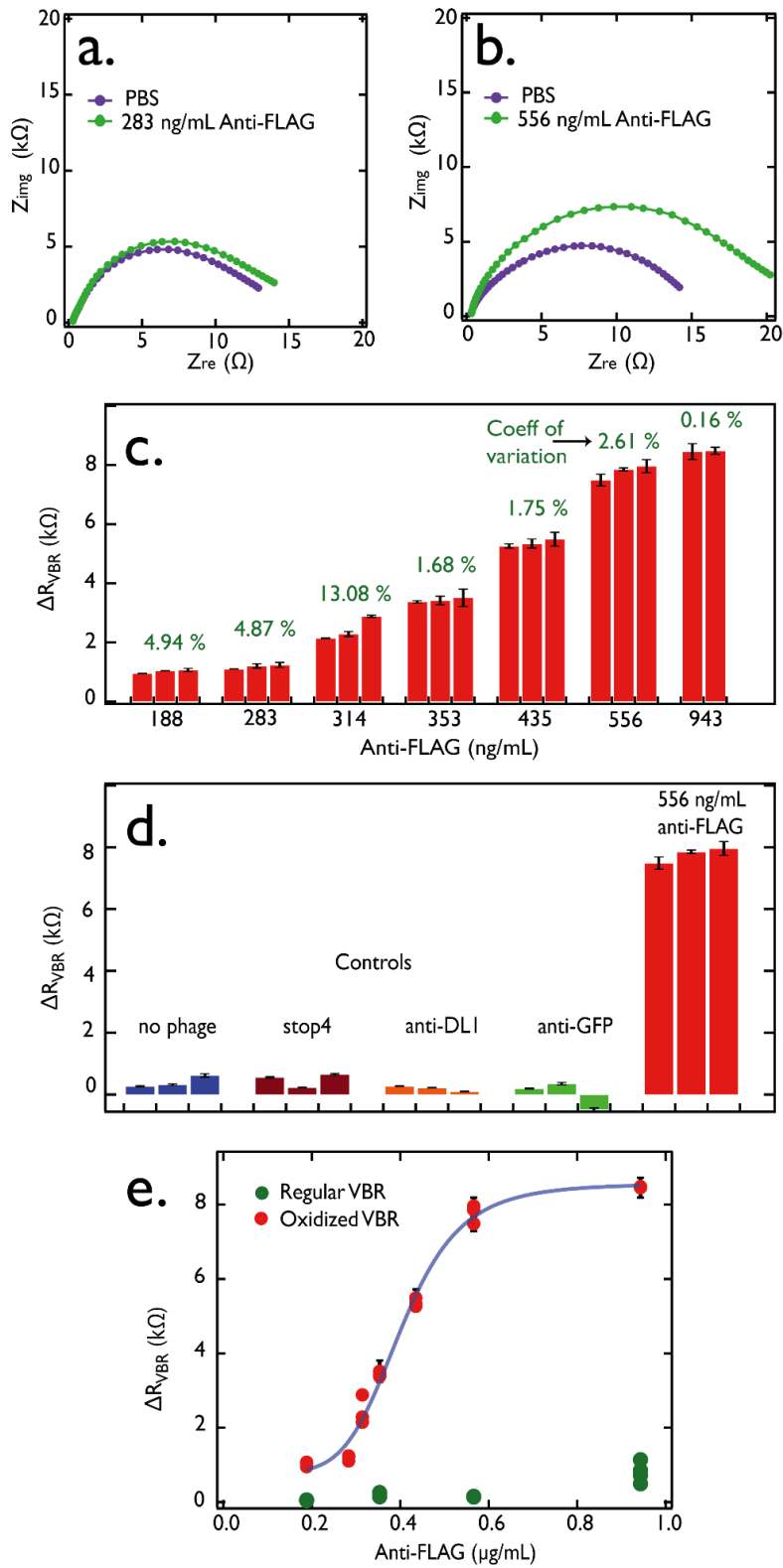


Figure 4.5 Detection of Anti-FLAG antibody with C2 phage loaded sensors. (a, b) Nyquist plots for a low concentration and high concentration anti-FLAG. Plots were obtained after

20-minute incubation in PBS for baseline measurement (purple) and 20-minute incubation of anti-FLAG (green)spiked in PBS. (c) Bar plot displaying signals imparted by 20 individual sensors. The CoVs lower than 13% assure that oxidation doesn't affect the reproducibility of the sensor. (d) Oxidized VBR specificity towards anti-FLAG detection for four control experiments. (e) Calibration plot fit to the Hill equation. The green dots display the signals generated by regular VBR in response to anti-FLAG.

4.3.5 Serum measurements

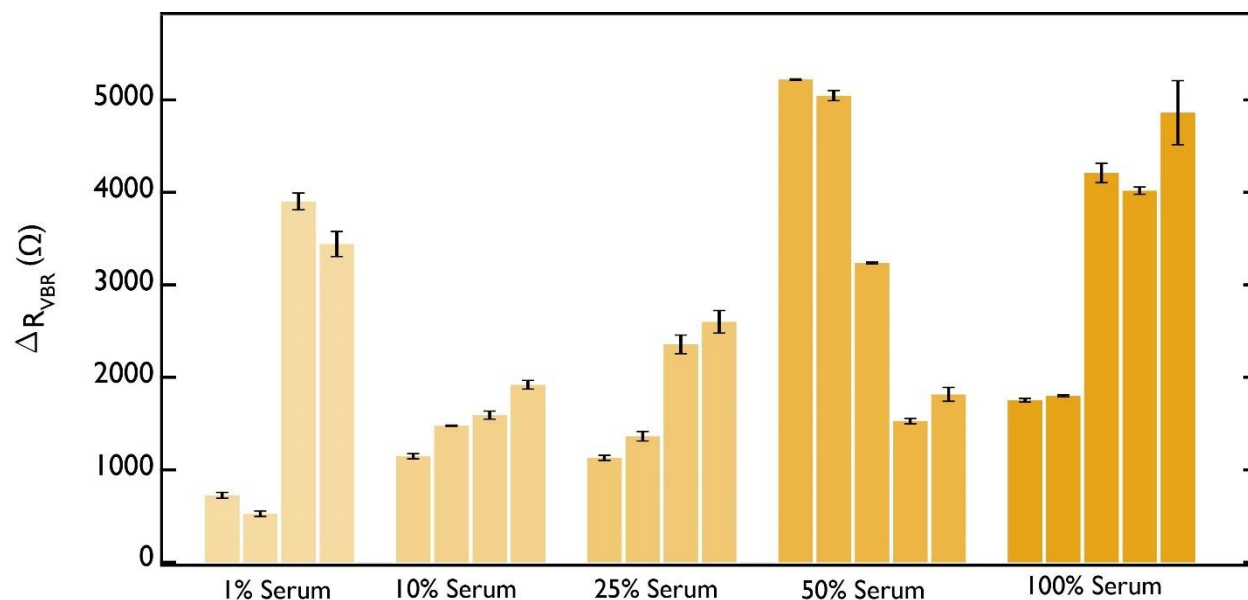


Figure 4.6 Serum measurements for individual devices. The high variability depicted can affect reliable antibody measurements.

To test the applicability of the sensor in human samples, human serum dilutions ranging from 1% to 100 % was subjected to sensor pre-equilibrated with PBS. The sensor surface was not passivated with blocking solutions for this experiment. Figure 4.6 depicts that serum generated high background signals without a blocking strategy. Using serum without devising for a blocking strategy will not only affect the limit of detection but will cut down on the range of antibody detection.

4.4 Summary

Detecting analytes for a wide variety of molecular weights is considered one of the desirable attributes of a biosensor. Detecting antibodies with electrochemical sensors promises to eliminate the complexity and exclusivity of the current test methods. Based on the *VBR* that reliably detected protein analytes HSA and Dj1, detection of antibodies was attempted to simplify antibody detection. While the regular *VBR* was found to be blind to detecting antibodies, morphological changes induced by oxidation, enabled oxidized *VBR* to detect antibodies. This did not affect the uninvolvement of the fabrication procedure and the sensor continued to distinguish between the electrical impedance of solution from the impedance signal generated by the bioaffinity film. The oxidized *VBR* was glazed with C2 phage for anti-FLAG concentration ranging from 188 ng/mL to 943 ng/mL. The sensor's performance wasn't affected in terms of reproducibility, but the equilibration time for measurement increased due to structural changes of the oxidized film.

Bibliography

- (1) Grieshaber, D.; MacKenzie, R.; Vörös, J.; Reimhult, E. *Sensors* **2008**, *8* (3), 1400–1458. <https://doi.org/10.3390/s8031400>.
- (2) Salimi, A.; Compton, R. G.; Hallaj, R. *Anal. Biochem.* **2004**, *333* (1), 49–56. <https://doi.org/10.1016/j.ab.2004.06.039>.
- (3) Rahman, M. M.; Umar, A.; Sawada, K. *Sensors Actuators B Chem.* **2009**, *137* (1), 327–333. <https://doi.org/10.1016/j.snb.2008.10.060>.
- (4) Liu, Y.; Yuan, R.; Chai, Y.; Tang, D.; Dai, J.; Zhong, X. *Sensors Actuators B Chem.* **2006**, *115* (1), 109–115. <https://doi.org/10.1016/j.snb.2005.08.048>.
- (5) Wang, Y. T.; Yu, L.; Wang, J.; Lou, L.; Du, W. J.; Zhu, Z. Q.; Peng, H.; Zhu, J. Z. *J. Electroanal. Chem.* **2011**, *661* (1), 8–12. <https://doi.org/10.1016/j.jelechem.2011.06.024>.
- (6) Tertiş, M.; Florea, A.; Feier, B.; Marian, I. O.; Silaghi-Dumitrescu, L.; Cristea, A.; Săndulescu, R.; Cristea, C. *J. Nanosci. Nanotechnol.* **2015**, *15* (5), 3385–3393. <https://doi.org/10.1166/jnn.2015.10208>.
- (7) Wang, L.; Xu, M.; Han, L.; Zhou, M.; Zhu, C.; Dong, S. *Anal. Chem.* **2012**, *84* (17), 7301–7307. <https://doi.org/10.1021/ac300521d>.
- (8) Yan, G.; Wang, Y.; He, X.; Wang, K.; Liu, J.; Du, Y. *Biosens. Bioelectron.* **2013**. <https://doi.org/10.1016/j.bios.2013.01.010>.
- (9) Loo, A. H.; Bonanni, A.; Pumera, M. *Nanoscale* **2013**, *5* (11), 4758. <https://doi.org/10.1039/c3nr00511a>.
- (10) Ghorbani-Bidkorbeh, F.; Shahrokhian, S.; Mohammadi, A.; Dinarvand, R. *Electrochim. Acta* **2010**, *55* (8), 2752–2759. <https://doi.org/10.1016/j.electacta.2009.12.052>.
- (11) Yang, Z.; Zhang, C.; Zhang, J.; Bai, W. *Biosens. Bioelectron.* **2014**, *51*, 268–273. <https://doi.org/10.1016/j.bios.2013.07.054>.
- (12) Zhao, J.; Chen, G.; Zhu, L.; Li, G. *Electrochem. commun.* **2011**, *13* (1), 31–33. <https://doi.org/10.1016/j.elecom.2010.11.005>.
- (13) Wang, A.; Ornelas, C.; Astruc, D.; Hapiot, P. *J. Am. Chem. Soc.* **2009**, *131* (19), 6652–6653. <https://doi.org/10.1021/ja900645j>.
- (14) Zhai, D.; Liu, B.; Shi, Y.; Pan, L.; Wang, Y.; Li, W.; Zhang, R.; Yu, G. *ACS Nano* **2013**, *7* (4), 3540–3546. <https://doi.org/10.1021/nn400482d>.
- (15) Lei, R.; Guo, C.; Xiong, H.; Dong, C.; Zhang, X.; Wang, S. *Electroanalysis* **2014**, *26* (5), 1004–1012. <https://doi.org/10.1002/elan.201300640>.
- (16) Liu, G.; Qi, M.; Zhang, Y.; Cao, C.; Goldys, E. M. *Anal. Chim. Acta* **2016**, *909*, 1–8.

- <https://doi.org/10.1016/j.aca.2015.12.023>.
- (17) Niu, X.; Huang, L.; Zhao, J.; Yin, M.; Luo, D.; Yang, Y. *Anal. Methods* **2016**, *8* (5), 1091–1095. <https://doi.org/10.1039/C5AY01747E>.
- (18) Lippa, P. B.; Sokoll, L. J.; Chan, D. W. *Clin. Chim. Acta* **2001**, *314* (1–2), 1–26. [https://doi.org/10.1016/S0009-8981\(01\)00629-5](https://doi.org/10.1016/S0009-8981(01)00629-5).
- (19) Chaubey, A.; Malhotra, B. D. *Biosens. Bioelectron.* **2002**, *17* (6–7), 441–456. [https://doi.org/10.1016/S0956-5663\(01\)00313-X](https://doi.org/10.1016/S0956-5663(01)00313-X).
- (20) Michael, D. J.; Wightman, R. M. *J. Pharm. Biomed. Anal.* **1999**, *19* (1–2), 33–46. [https://doi.org/10.1016/S0731-7085\(98\)00145-9](https://doi.org/10.1016/S0731-7085(98)00145-9).
- (21) Sakata, T. *ACS Omega* **2019**, *4* (7), 11852–11862. <https://doi.org/10.1021/acsomega.9b01629>.
- (22) Patolsky, F.; Zayats, M.; Katz, E.; Willner, I. *Anal. Chem.* **1999**, *71* (15), 3171–3180. <https://doi.org/10.1021/ac9901541>.
- (23) Pei, R.; Cheng, Z.; Wang, E.; Yang, X. *Biosens. Bioelectron.* **2001**, *16* (6), 355–361. [https://doi.org/10.1016/S0956-5663\(01\)00150-6](https://doi.org/10.1016/S0956-5663(01)00150-6).
- (24) Caras, S.; Janata, J. *Anal. Chem.* **1980**, *52* (12), 1935–1937. <https://doi.org/10.1021/ac50062a035>.
- (25) Luo, X.-L.; Xu, J.-J.; Zhao, W.; Chen, H.-Y. *Sensors Actuators B Chem.* **2004**, *97* (2–3), 249–255. <https://doi.org/10.1016/j.snb.2003.08.024>.
- (26) Zhang, W.; Wang, R.; Luo, F.; Wang, P.; Lin, Z. *Chinese Chem. Lett.* **2020**, *31* (3), 589–600. <https://doi.org/10.1016/j.ccllet.2019.09.022>.
- (27) da Silva, E. T. S. G.; Souto, D. E. P.; Barragan, J. T. C.; de F. Giarola, J.; de Moraes, A. C. M.; Kubota, L. T. *ChemElectroChem* **2017**, *4* (4), 778–794. <https://doi.org/10.1002/celec.201600758>.
- (28) Gooding, J. J. *Electroanalysis* **2002**, *14* (17), 1149–1156. [https://doi.org/10.1002/1521-4109\(200209\)14:17<1149::AID-ELAN1149>3.0.CO;2-8](https://doi.org/10.1002/1521-4109(200209)14:17<1149::AID-ELAN1149>3.0.CO;2-8).
- (29) Prieto-Simón, B.; Campàs, M.; Marty, J.-L. *Bioanal. Rev.* **2010**, *1* (2–4), 141–157. <https://doi.org/10.1007/s12566-010-0010-1>.
- (30) Ghindilis, A. L.; Atanasov, P.; Wilkins, E. *Electroanalysis* **1997**, *9* (9), 661–674. <https://doi.org/10.1002/elan.1140090902>.
- (31) Zhen, G.; Egli, V.; Vörös, J.; Zammaretti, P.; Textor, M.; Glockshuber, R.; Kuennemann, E. *Langmuir* **2004**, *20* (24), 10464–10473. <https://doi.org/10.1021/la0482812>.
- (32) Tavallaie, R.; McCarroll, J.; Le Grand, M.; Ariotti, N.; Schuhmann, W.; Bakker, E.; Tilley, R. D.; Hibbert, D. B.; Kavallaris, M.; Gooding, J. J. *Nat. Nanotechnol.* **2018**, *13* (11), 1066–1071. <https://doi.org/10.1038/s41565-018-0232-x>.

- (33) Yang, L.-M. C.; Tam, P. Y.; Murray, B. J.; McIntire, T. M.; Overstreet, C. M.; Weiss, G. A.; Penner, R. M. *Anal. Chem.* **2006**, *78* (10), 3265–3270.
<https://doi.org/10.1021/ac052287u>.
- (34) Smith, G. P.; Petrenko, V. A. *Chem. Rev.* **1997**, *97* (2), 391–410.
<https://doi.org/10.1021/cr960065d>.
- (35) Smith, G. P. *Angew. Chemie Int. Ed.* **2019**, *58* (41), 14428–14437.
<https://doi.org/10.1002/anie.201908308>.
- (36) Winter, G.; Milstein, C. Man-Made Antibodies. *Nature*. January 1991, pp 293–299.
<https://doi.org/10.1038/349293a0>.
- (37) Marks, J. D.; Hoogenboom, H. R.; Bonnert, T. P.; McCafferty, J.; Griffiths, A. D.; Winter, G. *J. Mol. Biol.* **1991**, *222* (3), 581–597. [https://doi.org/10.1016/0022-2836\(91\)90498-U](https://doi.org/10.1016/0022-2836(91)90498-U).
- (38) Weiss, G. A.; Penner, R. M. *Anal. Chem.* **2008**, *80* (9), 3082–3089.
<https://doi.org/10.1021/ac086009h>.
- (39) Li, Z.; Chen, G. Y. *Nanomaterials* **2018**, *8* (5), 278–283.
<https://doi.org/10.3390/nano8050278>.
- (40) Petrenko, V. A.; Vodyanoy, V. J. *J. Microbiol. Methods* **2003**, *53* (2), 253–262.
[https://doi.org/10.1016/S0167-7012\(03\)00029-0](https://doi.org/10.1016/S0167-7012(03)00029-0).
- (41) Petrenko, V. A. *Microelectronics J.* **2008**, *39* (2), 202–207.
<https://doi.org/10.1016/j.mejo.2006.11.007>.
- (42) Nanduri, V.; Sorokulova, I. B.; Samoylov, A. M.; Simonian, A. L.; Petrenko, V. A.; Vodyanoy, V. *Biosens. Bioelectron.* **2007**, *22* (6), 986–992.
<https://doi.org/10.1016/j.bios.2006.03.025>.
- (43) Yang, L.-M. C.; Diaz, J. E.; McIntire, T. M.; Weiss, G. A.; Penner, R. M. *Anal. Chem.* **2008**, *80* (4), 933–943. <https://doi.org/10.1021/ac071470f>.
- (44) Yang, L. C.; Diaz, J. E.; McIntire, T. M.; Weiss, G. a; Penner, R. M. *Anal. Chem.* **2008**, *80* (15), 5695–5705. <https://doi.org/10.1021/ac8008109>.
- (45) Zhang, S.; Huang, F.; Liu, B.; Ding, J.; Xu, X.; Kong, J. *Talanta* **2007**, *71* (2), 874–881.
<https://doi.org/10.1016/j.talanta.2006.05.081>.
- (46) Yan, F.; Sadik, O. A. *Anal. Chem.* **2001**, *73* (21), 5272–5280.
<https://doi.org/10.1021/ac015516v>.
- (47) Yan, F.; Sadik, O. A. *J. Am. Chem. Soc.* **2001**, *123* (46), 11335–11340.
<https://doi.org/10.1021/ja005719l>.
- (48) Ruan, C.; Yang, L.; Li, Y. *Anal. Chem.* **2002**, *74* (18), 4814–4820.
<https://doi.org/10.1021/ac025647b>.
- (49) Liu, J.; Tian, S.; Neilsen, P. E.; Knoll, W. *Chem. Commun.* **2005**, No. 23, 2969–2971.

- <https://doi.org/10.1039/b419425j>.
- (50) Yang, L.; Li, Y.; Erf, G. F. *Anal. Chem.* **2004**, *76* (4), 1107–1113. <https://doi.org/10.1021/ac0352575>.
- (51) Taggart, D. K.; Yang, Y.; Kung, S.-C.; McIntire, T. M.; Penner, R. M. *Nano Lett.* **2011**, *11* (1), 125–131. <https://doi.org/10.1021/nl103003d>.
- (52) Xiang, C.; Kung, S.-C.; Taggart, D. K.; Yang, F.; Thompson, M. A.; Güell, A. G.; Yang, Y.; Penner, R. M. *ACS Nano* **2008**, *2* (9), 1939–1949. <https://doi.org/10.1021/nn800394k>.
- (53) Xiang, C.; Yang, Y.; Penner, R. M. *Chem. Commun.* **2009**, No. 8, 859. <https://doi.org/10.1039/b815603d>.
- (54) Lamboy, J. A.; Arter, J. A.; Knopp, K. A.; Der, D.; Overstreet, C. M.; Palermo, E. F.; Urakami, H.; Yu, T.-B.; Tezgel, O.; Tew, G. N.; et al. *J. Am. Chem. Soc.* **2009**, *131* (45), 16454–16460. <https://doi.org/10.1021/ja9050873>.
- (55) Donovan, K. C.; Arter, J. A.; Weiss, G. A.; Penner, R. M. *Langmuir* **2012**, *28* (34), 12581–12587. <https://doi.org/10.1021/la302473j>.
- (56) Arter, J. A.; Taggart, D. K.; McIntire, T. M.; Penner, R. M.; Weiss, G. A. *Nano Lett.* **2010**, *10* (12), 4858–4862. <https://doi.org/10.1021/nl1025826>.
- (57) Arter, J. A.; Diaz, J. E.; Donovan, K. C.; Yuan, T.; Penner, R. M.; Weiss, G. A. *Anal. Chem.* **2012**, *84* (6), 2776–2783. <https://doi.org/10.1021/ac203143y>.
- (58) Menke, E. J.; Thompson, M. A.; Xiang, C.; Yang, L. C.; Penner, R. M. *Nat. Mater.* **2006**, *5* (11), 914–919. <https://doi.org/10.1038/nmat1759>.
- (59) Chang, S. S. *Rev. Urol.* **2004**, *6 Suppl 10*, S13-8.
- (60) O’Keefe, D. S.; Bacich, D. J.; Heston, W. D. W. *Prostate* **2004**, *58* (2), 200–210. <https://doi.org/10.1002/pros.10319>.
- (61) Diaz, J. E.; Yang, L.-M. C.; Lamboy, J. A.; Penner, R. M.; Weiss, G. A. Synthesis of a Virus Electrode for Measurement of Prostate Specific Membrane Antigen. In *Methods in molecular biology (Clifton, N.J.)*; 2009; pp 255–274. https://doi.org/10.1007/978-1-60327-569-9_16.
- (62) Mohan, K.; Donovan, K. C.; Arter, J. A.; Penner, R. M.; Weiss, G. A. *J. Am. Chem. Soc.* **2013**, *135* (20), 7761–7767. <https://doi.org/10.1021/ja4028082>.
- (63) Donovan, K. C.; Arter, J. A.; Pilolli, R.; Cioffi, N.; Weiss, G. A.; Penner, R. M. *Anal. Chem.* **2011**, *83* (7), 2420–2424. <https://doi.org/10.1021/ac2000835>.
- (64) Bhasin, A.; Sanders, E. C.; Ziegler, J. M.; Briggs, J. S.; Drago, N. P.; Attar, A. M.; Santos, A. M.; True, M. Y.; Ogata, A. F.; Yoon, D. V.; et al. *Anal. Chem.* **2020**, *92* (9), 6654–6666. <https://doi.org/10.1021/acs.analchem.0c00534>.
- (65) Mohan, K.; Penner, R. M.; Weiss, G. A. *Curr. Protoc. Chem. Biol.* **2015**, *7* (2), 53–72.

<https://doi.org/10.1002/9780470559277.ch140213>.

- (66) Ogata, A. F.; Edgar, J. M.; Majumdar, S.; Briggs, J. S.; Patterson, S. V.; Tan, M. X.; Kudlacek, S. T.; Schneider, C. A.; Weiss, G. A.; Penner, R. M. *Anal. Chem.* **2017**, *89* (2), 1373–1381. <https://doi.org/10.1021/acs.analchem.6b04840>.
- (67) Bhasin, A.; Ogata, A. F.; Briggs, J. S.; Tam, P. Y.; Tan, M. X.; Weiss, G. A.; Penner, R. M. *Nano Lett.* **2018**, *18* (6), 3623–3629. <https://doi.org/10.1021/acs.nanolett.8b00723>.
- (68) Simon, D. T.; Gabrielsson, E. O.; Tybrandt, K.; Berggren, M. *Chem. Rev.* **2016**, *116* (21), 13009–13041. <https://doi.org/10.1021/acs.chemrev.6b00146>.
- (69) Lanzani, G. *Nat. Mater.* **2014**, *13* (8), 775–776. <https://doi.org/10.1038/nmat4021>.
- (70) Liao, C.; Zhang, M.; Yao, M. Y.; Hua, T.; Li, L.; Yan, F. *Adv. Mater.* **2015**, *27* (46), 7493–7527. <https://doi.org/10.1002/adma.201402625>.
- (71) Cohen-Karni, T.; Qing, Q.; Li, Q.; Fang, Y.; Lieber, C. M. *Nano Lett.* **2010**, *10* (3), 1098–1102. <https://doi.org/10.1021/nl1002608>.
- (72) Cohen-Karni, T.; Casanova, D.; Cahoon, J. F.; Qing, Q.; Bell, D. C.; Lieber, C. M. *Nano Lett.* **2012**, *12* (5), 2639–2644. <https://doi.org/10.1021/nl3011337>.
- (73) Pankratova, G.; Hasan, K.; Leech, D.; Hederstedt, L.; Gorton, L. *Electrochem. commun.* **2017**, *75*, 56–59. <https://doi.org/10.1016/j.elecom.2016.12.010>.
- (74) Yuan, Y.; Shin, H.; Kang, C.; Kim, S. *Bioelectrochemistry* **2016**, *108*, 8–12. <https://doi.org/10.1016/j.bioelechem.2015.11.001>.
- (75) Kaneko, M.; Ishikawa, M.; Hashimoto, K.; Nakanishi, S. *Bioelectrochemistry* **2017**, *114*, 8–12. <https://doi.org/10.1016/j.bioelechem.2016.11.001>.
- (76) Xue, W.; Jiang, X.; Harima, Y. *Synth. Met.* **2010**, *160* (7–8), 803–807. <https://doi.org/10.1016/j.synthmet.2010.01.026>.
- (77) Harris, P. D.; Arnold, W. M.; Andrews, M. K.; Partridge, A. C. *Sensors Actuators B Chem.* **1997**, *42* (3), 177–184. [https://doi.org/10.1016/S0925-4005\(97\)80334-6](https://doi.org/10.1016/S0925-4005(97)80334-6).
- (78) Bruschi, P.; Cacialli, F.; Nannini, A.; Neri, B. *J. Appl. Phys.* **1994**, *76* (6), 3640–3644. <https://doi.org/10.1063/1.357427>.
- (79) Yu, L.; Zhang, Y.; Hu, C.; Wu, H.; Yang, Y.; Huang, C.; Jia, N. *Food Chem.* **2015**, *176*, 22–26. <https://doi.org/10.1016/j.foodchem.2014.12.030>.
- (80) Eissa, S.; Siaj, M.; Zourob, M. *Biosens. Bioelectron.* **2015**, *69*, 148–154. <https://doi.org/10.1016/j.bios.2015.01.055>.
- (81) Zhang, J.; Wu, D.-Z.; Cai, S.-X.; Chen, M.; Xia, Y.-K.; Wu, F.; Chen, J.-H. *Biosens. Bioelectron.* **2016**, *75*, 452–457. <https://doi.org/10.1016/j.bios.2015.09.006>.
- (82) Li, N.; Brahmendra, A.; Veloso, A. J.; Prashar, A.; Cheng, X. R.; Hung, V. W. S.; Guyard, C.; Terebiznik, M.; Kerman, K. *Anal. Chem.* **2012**, *84* (8), 3485–3488. <https://doi.org/10.1021/ac3003227>.

- (83) Gao, Z.; Deng, H.; Shen, W.; Ren, Y. *Anal. Chem.* **2013**, *85* (3), 1624–1630. <https://doi.org/10.1021/ac302883c>.
- (84) Kurganov, B. ; Lobanov, A. ; Borisov, I. ; Reshetilov, A. . *Anal. Chim. Acta* **2001**, *427* (1), 11–19. [https://doi.org/10.1016/S0003-2670\(00\)01167-3](https://doi.org/10.1016/S0003-2670(00)01167-3).
- (85) Chu, C.-H.; Sarangadharan, I.; Regmi, A.; Chen, Y.-W.; Hsu, C.-P.; Chang, W.-H.; Lee, G.-Y.; Chyi, J.-I.; Chen, C.-C.; Shiesh, S.-C.; et al. *Sci. Rep.* **2017**, *7* (1), 5256. <https://doi.org/10.1038/s41598-017-05426-6>.
- (86) Dockal, M.; Carter, D. C.; Rüker, F. *J. Biol. Chem.* **1999**, *274* (41), 29303–29310. <https://doi.org/10.1074/jbc.274.41.29303>.
- (87) Meier, A. R.; Bahureksa, W. A.; Heien, M. L. *J. Phys. Chem. C* **2016**, *120* (37), 21114–21122. <https://doi.org/10.1021/acs.jpcc.6b04622>.
- (88) Pasha, A.; Khasim, S.; Al-Hartomy, O. A.; Lakshmi, M.; Manjunatha, K. G. *RSC Adv.* **2018**, *8* (32), 18074–18083. <https://doi.org/10.1039/C8RA01061G>.
- (89) Stoian, A. B.; Pirvu, C.; Demetrescu, I. Effects of PEG on the Stability and Electrochemical Properties of PEDOT: PSS Films Obtained by Spin Coating. In *2014 International Semiconductor Conference (CAS)*; IEEE, 2014; pp 81–84. <https://doi.org/10.1109/SMICND.2014.6966397>.
- (90) Chou, T.-R.; Chen, S.-H.; Chiang, Y.-T.; Lin, Y.-T.; Chao, C.-Y. *J. Mater. Chem. C* **2015**, *3* (15), 3760–3766. <https://doi.org/10.1039/C5TC00276A>.
- (91) Majorek, K. A.; Porebski, P. J.; Dayal, A.; Zimmerman, M. D.; Jablonska, K.; Stewart, A. J.; Chruszcz, M.; Minor, W. *Mol. Immunol.* **2012**, *52* (3–4), 174–182. <https://doi.org/10.1016/j.molimm.2012.05.011>.
- (92) Di Meo, A.; Bartlett, J.; Cheng, Y.; Pasic, M. D.; Yousef, G. M. *Mol. Cancer* **2017**, *16* (1), 80. <https://doi.org/10.1186/s12943-017-0644-5>.
- (93) Kumar, P.; Nandi, S.; Tan, T. Z.; Ler, S. G.; Chia, K. S.; Lim, W.-Y.; Bütow, Z.; Vordos, D.; De laTaille, A.; Al-Haddawi, M.; et al. *Oncotarget* **2015**, *6* (15), 13539–13549. <https://doi.org/10.18632/oncotarget.3841>.
- (94) Soukup, V.; Capoun, O.; Pesl, M.; Vavrova, L.; Sobotka, R.; Levova, K.; Hanus, T.; Zima, T.; Kalousova, M. *Neoplasma* **2019**, *66* (06), 1019–1023. https://doi.org/10.4149/neo_2019_190124N74.
- (95) Bhasin, A.; Ogata, A. F.; Briggs, J. S.; Tam, P. Y.; Tan, M. X.; Weiss, G. A.; Penner, R. M. *Nano Lett.* **2018**, *18* (6), 3623–3629. <https://doi.org/10.1021/acs.nanolett.8b00723>.
- (96) Ku, J. Y.; Lee, C. H.; Lee, K.; Kim, K. H.; Baek, S. R.; Park, J. H.; Lee, J. Z.; Park, H. J.; Han, S. H.; Jeong, I. Y.; et al. *Eur. Urol. Suppl.* **2017**, *16* (3), e1450–e1453. [https://doi.org/10.1016/S1569-9056\(17\)30884-9](https://doi.org/10.1016/S1569-9056(17)30884-9).
- (97) D’Costa, J. J.; Goldsmith, J. C.; Wilson, J. S.; Bryan, R. T.; Ward, D. G. *Bl. Cancer* **2016**, *2* (3), 301–317. <https://doi.org/10.3233/BLC-160054>.

- (98) Seki, Y.; Takahashi, M.; Takashiri, M. *RSC Adv.* **2019**, *9* (28), 15957–15965. <https://doi.org/10.1039/C9RA02310K>.
- (99) Purdy, K. R.; Fraden, S. *Phys. Rev. E* **2004**, *70* (6), 061703. <https://doi.org/10.1103/PhysRevE.70.061703>.
- (100) Donovan, K. C.; Arter, J. A.; Weiss, G. A.; Penner, R. M. *Langmuir* **2012**, *28* (34), 12581–12587. <https://doi.org/10.1021/la302473j>.
- (101) Kim, D.-J.; Lee, N.-E.; Park, J.-S.; Park, I.-J.; Kim, J.-G.; Cho, H. J. *Biosens. Bioelectron.* **2010**, *25* (11), 2477–2482. <https://doi.org/10.1016/j.bios.2010.04.013>.
- (102) Picca, R. A.; Manoli, K.; Macchia, E.; Sarcina, L.; Di Franco, C.; Cioffi, N.; Blasi, D.; Österbacka, R.; Torricelli, F.; Scamarcio, G.; et al. *Adv. Funct. Mater.* **2020**, *30* (20), 1904513. <https://doi.org/10.1002/adfm.201904513>.
- (103) Gentili, D.; D'Angelo, P.; Militano, F.; Mazzei, R.; Poerio, T.; Bruciale, M.; Tarabella, G.; Bonetti, S.; Marasso, S. L.; Cocuzza, M.; et al. *J. Mater. Chem. B* **2018**, *6* (33), 5400–5406. <https://doi.org/10.1039/C8TB01697F>.
- (104) Gualandi, I.; Tessarolo, M.; Mariani, F.; Cramer, T.; Tonelli, D.; Scavetta, E.; Fraboni, B. *Sensors Actuators B Chem.* **2018**, *273*, 834–841. <https://doi.org/10.1016/j.snb.2018.06.109>.
- (105) Kim, Y.; Lim, T.; Kim, C.-H.; Yeo, C. S.; Seo, K.; Kim, S.-M.; Kim, J.; Park, S. Y.; Ju, S.; Yoon, M.-H. *NPG Asia Mater.* **2018**, *10* (11), 1086–1095. <https://doi.org/10.1038/s41427-018-0097-3>.
- (106) Macchia, E.; Romele, P.; Manoli, K.; Ghittorelli, M.; Magliulo, M.; Kovács-Vajna, Z. M.; Torricelli, F.; Torsi, L. *Flex. Print. Electron.* **2018**, *3* (3), 034002. <https://doi.org/10.1088/2058-8585/aad0cb>.
- (107) Fu, Y.; Wang, N.; Yang, A.; Law, H. K.; Li, L.; Yan, F. *Adv. Mater.* **2017**, *29* (41), 1703787. <https://doi.org/10.1002/adma.201703787>.
- (108) Gualandi, I.; Tonelli, D.; Mariani, F.; Scavetta, E.; Marzocchi, M.; Fraboni, B. *Sci. Rep.* **2016**, *6* (1), 35419. <https://doi.org/10.1038/srep35419>.
- (109) Zhang, F.; Johansson, M.; Andersson, M. R.; Hummelen, J. C.; Inganäs, O. *Adv. Mater.* **2002**, *14* (9), 662–665. [https://doi.org/10.1002/1521-4095\(20020503\)14:9<662::AID-ADMA662>3.0.CO;2-N](https://doi.org/10.1002/1521-4095(20020503)14:9<662::AID-ADMA662>3.0.CO;2-N).
- (110) Thomas, J. P.; Zhao, L.; McGillivray, D.; Leung, K. T. *J. Mater. Chem. A* **2014**, *2* (7), 2383–2389. <https://doi.org/10.1039/c3ta14590e>.
- (111) Ouyang, J.; Xu, Q.; Chu, C.-W.; Yang, Y.; Li, G.; Shinar, J. *Polymer (Guildf)*. **2004**, *45* (25), 8443–8450. <https://doi.org/10.1016/j.polymer.2004.10.001>.
- (112) Poverenov, E.; Li, M.; Bitler, A.; Bendikov, M. *Chem. Mater.* **2010**, *22* (13), 4019–4025. <https://doi.org/10.1021/cm100561d>.
- (113) (nee Włodarczyk), K. C.; Karczewski, J.; Jasiński, P. *Electrochim. Acta* **2015**, *176*, 156–

161. <https://doi.org/10.1016/j.electacta.2015.07.006>.
- (114) Brug, G. J.; van den Eeden, A. L. G.; Sluyters-Rehbach, M.; Sluyters, J. H. *J. Electroanal. Chem. Interfacial Electrochem.* **1984**, *176* (1–2), 275–295. [https://doi.org/10.1016/S0022-0728\(84\)80324-1](https://doi.org/10.1016/S0022-0728(84)80324-1).
- (115) Islam, F.; Haque, M. H.; Yadav, S.; Islam, M. N.; Gopalan, V.; Nguyen, N.-T.; Lam, A. K.; Shiddiky, M. J. A. *Sci. Rep.* **2017**, *7* (1), 133. <https://doi.org/10.1038/s41598-017-00206-8>.
- (116) Frey, B. L.; Jordan, C. E.; Kornguth, S.; Corn, R. M. *Anal. Chem.* **1995**, *67* (24), 4452–4457. <https://doi.org/10.1021/ac00120a003>.
- (117) Pasinszki, T.; Krebsz, M.; Tung, T. T.; Losic, D. *Sensors* **2017**, *17* (8), 1919. <https://doi.org/10.3390/s17081919>.
- (118) Ortiz-Aguayo, D.; del Valle, M. *Sensors* **2018**, *18* (2), 354. <https://doi.org/10.3390/s18020354>.
- (119) Roda, A.; Michelini, E.; Zangheri, M.; Di Fusco, M.; Calabria, D.; Simoni, P. *TrAC Trends Anal. Chem.* **2016**, *79*, 317–325. <https://doi.org/10.1016/j.trac.2015.10.019>.
- (120) Brás, E. J. S.; Fortes, A. M.; Chu, V.; Fernandes, P.; Conde, J. P. *Analyst* **2019**, *144* (16), 4871–4879. <https://doi.org/10.1039/C9AN01002E>.
- (121) Kaisti, M. *Biosens. Bioelectron.* **2017**, *98*, 437–448. <https://doi.org/10.1016/j.bios.2017.07.010>.
- (122) Karr, L. J.; Shafer, S. G.; Harris, J. M.; Van Alstine, J. M.; Snyder, R. S. *J. Chromatogr. A* **1986**, *354*, 269–282. [https://doi.org/10.1016/S0021-9673\(01\)87028-X](https://doi.org/10.1016/S0021-9673(01)87028-X).
- (123) Field, C. R.; Yeom, J.; Salehi-Khojin, A.; Masel, R. I. *Sensors Actuators B Chem.* **2010**, *148* (1), 315–322. <https://doi.org/10.1016/j.snb.2010.05.026>.
- (124) Alizadeh, T.; Rezaloo, F. *Sensors Actuators B Chem.* **2013**, *176*, 28–37. <https://doi.org/10.1016/j.snb.2012.08.049>.
- (125) Llobet, E. *Sensors Actuators B Chem.* **2013**, *179*, 32–45. <https://doi.org/10.1016/j.snb.2012.11.014>.
- (126) Hangarter, C. M.; Chartuprayoon, N.; Hernández, S. C.; Choa, Y.; Myung, N. V. *Nano Today* **2013**, *8* (1), 39–55. <https://doi.org/10.1016/j.nantod.2012.12.005>.
- (127) Doleman, B. J.; Sanner, R. D.; Severin, E. J.; Grubbs, R. H.; Lewis, N. S. *Anal. Chem.* **1998**, *70* (13), 2560–2564. <https://doi.org/10.1021/ac971238h>.
- (128) Lux, F. *J. Mater. Sci.* **1993**, *28* (2), 285–301. <https://doi.org/10.1007/BF00357799>.
- (129) McLachlan, D. S.; Blaszkiewicz, M.; Newnham, R. E. *J. Am. Ceram. Soc.* **1990**, *73* (8), 2187–2203. <https://doi.org/10.1111/j.1151-2916.1990.tb07576.x>.
- (130) Sauerbrey, G. *Zeitschrift fuer Phys.* **1959**.

- (131) Kondo, A.; Murakami, F.; Higashitani, K. *Biotechnol. Bioeng.* **1992**, *40* (8), 889–894. <https://doi.org/10.1002/bit.260400804>.
- (132) Rodahl, M.; Höök, F.; Fredriksson, C.; Keller, C. A.; Krozer, A.; Brzezinski, P.; Voinova, M.; Kasemo, B. *Faraday Discuss.* **1997**, *107*, 229–246. <https://doi.org/10.1039/a703137h>.
- (133) Honbou, K.; Suzuki, N. N.; Horiuchi, M.; Niki, T.; Taira, T.; Ariga, H.; Inagaki, F. *J. Biol. Chem.* **2003**, *278* (33), 31380–31384. <https://doi.org/10.1074/jbc.M305878200>.
- (134) Allen J. Bard, L. R. F. *Electrochemical Methods: Fundamentals and Applications, 2nd Edition*; 2001.
- (135) Ballew, J. T.; Murray, J. A.; Collin, P.; Maki, M.; Kagnoff, M. F.; Kaukinen, K.; Daugherty, P. S. *Proc. Natl. Acad. Sci.* **2013**, *110* (48), 19330–19335. <https://doi.org/10.1073/pnas.1314792110>.
- (136) Scott, A. M.; Wolchok, J. D.; Old, L. J. *Nat. Rev. Cancer* **2012**, *12* (4), 278–287. <https://doi.org/10.1038/nrc3236>.
- (137) Yang, L. M. C.; Diaz, J. E.; McIntire, T. M.; Weiss, G. A.; Penner, R. M. *Anal. Chem.* **2008**, *80* (15), 5695–5705. <https://doi.org/10.1021/ac8008109>.
- (138) Ionescu, R. E.; Cosnier, S.; Herrmann, S.; Marks, R. S. *Anal. Chem.* **2007**, *79* (22), 8662–8668. <https://doi.org/10.1021/ac0707129>.
- (139) Mollarasouli; Kurbanoglu; Ozkan. *Biosensors* **2019**, *9* (3), 86. <https://doi.org/10.3390/bios9030086>.
- (140) Pei, Z.; Anderson, H.; Myrskog, A.; Dunér, G.; Ingemarsson, B.; Aastrup, T. *Anal. Biochem.* **2010**, *398* (2), 161–168. <https://doi.org/10.1016/j.ab.2009.11.038>.
- (141) Dulay, S.; Lozano-Sánchez, P.; Iwuoha, E.; Katakis, I.; O’Sullivan, C. K. *Biosens. Bioelectron.* **2011**, *26* (9), 3852–3856. <https://doi.org/10.1016/j.bios.2011.02.045>.
- (142) Wei, W.; Zhang, L.; Ni, Q.; Pu, Y.; Yin, L.; Liu, S. **2014**, *845*, 38–44.
- (143) Li, J.; Lin, X.-Q. *Anal. Chim. Acta* **2007**, *596* (2), 222–230. <https://doi.org/10.1016/j.aca.2007.05.057>.
- (144) West, N.; Baker, P.; Waryo, T.; Ngece, F. R.; Iwuoha, E. I.; O’Sullivan, C.; Katakis, I. *J. Bioact. Compat. Polym.* **2013**, *28* (2), 167–177. <https://doi.org/10.1177/0883911512472277>.
- (145) Li, J.; Lin, X. *Sensors Actuators B Chem.* **2007**, *124* (2), 486–493. <https://doi.org/10.1016/j.snb.2007.01.021>.
- (146) Borazjani, M.; Mehdinia, A.; Jabbari, A. *J. Solid State Electrochem.* **2018**, *22* (2), 355–363. <https://doi.org/10.1007/s10008-017-3762-5>.
- (147) Majidi, M. R.; Jouyban, A.; Asadpour-Zeynali, K. *Electrochim. Acta* **2007**, *52* (21), 6248–6253. <https://doi.org/10.1016/j.electacta.2007.04.019>.

- (148) Tu, X.; Xie, Q.; Jiang, S.; Yao, S. *Biosens. Bioelectron.* **2007**, *22* (12), 2819–2826. <https://doi.org/10.1016/j.bios.2006.11.022>.
- (149) Ujvári, M.; Gubicza, J.; Kondratiev, V.; Szekeres, K. J.; Láng, G. G. *J. Solid State Electrochem.* **2015**, *19* (4), 1247–1252. <https://doi.org/10.1007/s10008-015-2746-6>.
- (150) Tybrandt, K.; Larsson, K. C.; Richter-Dahlfors, A.; Berggren, M. *Proc. Natl. Acad. Sci. U. S. A.* **2010**, *107* (22), 9929–9932. <https://doi.org/10.1073/pnas.0913911107>.
- (151) Bendikov, T. A.; Harmon, T. C. *Anal. Chim. Acta* **2005**, *551* (1–2), 30–36. <https://doi.org/10.1016/j.aca.2005.07.004>.
- (152) Hui, Y.; Bian, C.; Wang, J.; Tong, J.; Xia, S. *Sensors* **2017**, *17* (3), 628. <https://doi.org/10.3390/s17030628>.
- (153) Lin, J.-M.; Su, Y.-L.; Chang, W.-T.; Su, W.-Y.; Cheng, S.-H. *Electrochim. Acta* **2014**, *149*, 65–75. <https://doi.org/10.1016/j.electacta.2014.10.030>.
- (154) Harish, S.; Mathiyarasu, J.; Phani, K. L. N.; Yegnaraman, V. *J. Appl. Electrochem.* **2008**, *38* (11), 1583–1588. <https://doi.org/10.1007/s10800-008-9609-0>.
- (155) Kokkinos, C.; Angelopoulou, M.; Economou, A.; Prodromidis, M.; Florou, A.; Haasnoot, W.; Petrou, P.; Kakabakos, S. *Anal. Chem.* **2016**, *88* (13), 6897–6904. <https://doi.org/10.1021/acs.analchem.6b01625>.
- (156) Martín-Yerga, D.; González-García, M. B.; Costa-García, A. *Talanta* **2014**, *130*, 598–602. <https://doi.org/10.1016/j.talanta.2014.07.010>.
- (157) Neves, M. M. P. S.; González-García, M. B.; Nouws, H. P. A.; Costa-García, A. *Biosens. Bioelectron.* **2012**, *31* (1), 95–100. <https://doi.org/10.1016/j.bios.2011.09.044>.
- (158) Gogola, J. L.; Martins, G.; Caetano, F. R.; Ricciardi-Jorge, T.; Duarte dos Santos, C. N.; Marcolino-Junior, L. H.; Bergamini, M. F. *J. Electroanal. Chem.* **2019**, *842*, 140–145. <https://doi.org/10.1016/j.jelechem.2019.04.066>.
- (159) Cabral-miranda, G.; Cardoso, A. R.; Ferreira, L. C. S.; Sales, M. G. F.; Bachmann, M. F. *Biosens. Bioelectron.* **2018**, *113* (January), 101–107. <https://doi.org/10.1016/j.bios.2018.04.058>.
- (160) Cardoso, A. R.; Cabral-Miranda, G.; Reyes-Sandoval, A.; Bachmann, M. F.; Sales, M. G. F. *Biosens. Bioelectron.* **2017**, *91*, 833–841. <https://doi.org/10.1016/j.bios.2017.01.031>.
- (161) Premaratne, G.; Niroula, J.; Patel, M. K.; Zhong, W.; Suib, S. L.; Kalkan, A. K.; Krishnan, S. *Anal. Chem.* **2018**, *90* (21), 12456–12463. <https://doi.org/10.1021/acs.analchem.8b01565>.
- (162) Mahshid, S. S.; Mahshid, S.; Vallée-Bélisle, A.; Kelley, S. O. *Anal. Chem.* **2019**, *91* (8), 4943–4947. <https://doi.org/10.1021/acs.analchem.9b00648>.
- (163) Prado, I. C.; Souza, A. L. A.; Provance-Jr, D. W.; Cassella, R. J.; De-Simone, S. G. *Anal. Biochem.* **2017**, *538*, 13–19. <https://doi.org/10.1016/j.ab.2017.09.008>.

- (164) Khan, H. U.; Jang, J.; Kim, J. J.; Knoll, W. *J. Am. Chem. Soc.* **2011**, *133* (7), 2170–2176. <https://doi.org/10.1021/ja107088m>.
- (165) Aronoff-Spencer, E.; Venkatesh, A. G.; Sun, A.; Brickner, H.; Looney, D.; Hall, D. A. *Biosens. Bioelectron.* **2016**, *86*, 690–696. <https://doi.org/10.1016/j.bios.2016.07.023>.
- (166) Cosnier, S. *Biosens. Bioelectron.* **1999**, *14* (5), 443–456. [https://doi.org/10.1016/S0956-5663\(99\)00024-X](https://doi.org/10.1016/S0956-5663(99)00024-X).
- (167) Levasseur, D.; Mjejri, I.; Rolland, T.; Rougier, A. *Polymers (Basel)*. **2019**, *11* (1), 1–12. <https://doi.org/10.3390/polym11010179>.
- (168) Zykwiniska, A.; Domagala, W.; Pilawa, B.; Lapkowski, M. *Electrochim. Acta* **2005**, *50* (7–8), 1625–1633. <https://doi.org/10.1016/j.electacta.2004.10.026>.
- (169) Harada, H.; Fuchigami, T.; Nonaka, T. *J. Electroanal. Chem.* **1991**, *303* (1–2), 139–150. [https://doi.org/10.1016/0022-0728\(91\)85121-5](https://doi.org/10.1016/0022-0728(91)85121-5).
- (170) Palmisano, F.; Malitesta, C.; Centonze, D.; Zambonin, P. G. *Anal. Chem.* **1995**, *67* (13), 2207–2211. <https://doi.org/10.1021/ac00109a046>.
- (171) Hsu, C. F.; Zhang, L.; Peng, H.; Travas-Sejdic, J.; Kilmartin, P. A. *Curr. Appl. Phys.* **2008**, *8* (3–4), 316–319. <https://doi.org/10.1016/j.cap.2007.10.049>.
- (172) Marchesi, L. F. Q. P.; Simões, F. R.; Pocrifka, L. A.; Pereira, E. C. *J. Phys. Chem. B* **2011**, *115* (31), 9570–9575. <https://doi.org/10.1021/jp2041263>.
- (173) Safarnavadeh, V.; Zare, K.; Fakhari, A. R. *Biosens. Bioelectron.* **2013**, *49*, 159–163. <https://doi.org/10.1016/j.bios.2013.04.043>.
- (174) Witkowski, A.; Brajter-Toth, A. *Anal. Chem.* **1992**, *64* (6), 635–641. <https://doi.org/10.1021/ac00030a012>.
- (175) Amouzadeh Tabrizi, M.; Shamsipur, M.; Mostafaie, A. *Mater. Sci. Eng. C* **2016**, *59*, 965–969. <https://doi.org/10.1016/j.msec.2015.10.093>.
- (176) Kurganov, B. ; Lobanov, A. ; Borisov, I. ; Reshetilov, A. . *Anal. Chim. Acta* **2001**, *427* (1), 11–19. [https://doi.org/10.1016/S0003-2670\(00\)01167-3](https://doi.org/10.1016/S0003-2670(00)01167-3).
- (177) Blake II, R. C.; Ohmura, N.; Lackie, S. J.; Li, X.; Delehanty, J. B.; Darwish, I. A.; Blake, D. A. Monoclonal Antibodies That Exhibit Allosteric Binding Behavior. In *Trends Monoclonal Antibody Res*; 2005.
- (178) Matsuda, N.; Kimura, M.; Queliconi, B. B.; Kojima, W.; Mishima, M.; Takagi, K.; Koyano, F.; Yamano, K.; Mizushima, T.; Ito, Y.; et al. *Sci. Rep.* **2017**, *7* (1), 1–15. <https://doi.org/10.1038/s41598-017-13146-0>.
- (179) Eggertsson, G.; Söll, D. *Microbiol. Rev.* **1988**, *52* (3), 354–374.

Appendix A

Supplementary information for Chapter 3

A.1 Process windows compliance assessment of VBRs.

VBRs were evaluated at every step of the fabrication process to ensure the reproducibility of signal at each DJ-1 concentration. Starting with the fabrication by photolithography of gold electrodes, the VBR is prepared in five steps (Figure A.1). The parameters measured at each of these steps is indicated in the diagram for Fig. S1. In this diagram, the following definitions apply: R_{au} is the dc resistance of the gold electrodes prepared in step 1, measured along their longest dimension, $R_{PEDOT-PSS}$ is the dc resistance of the PEDOT-PSS film produced in step 2, Z_{im} and Z_{re} are the baseline impedances measured for the PEDOT-PSS film after incubation in PBS for 30 min in step 3; i_p is the peak current for the electropolymerization, by cyclic voltammetry, of the virus-PEDOT composite in step 4. The VBR device yield using the process windows described below was $\approx 60\%$.

Step 1: The DC resistance between two end-points on the individual gold pad should be 3.9 to 5 Ω . This resistance adds to the resistance of spin-coated PEDOT-PSS resistance to yield the final DC resistance across PEDOT-PSS coated electrodes.

Step 2: Chips with DC resistance across the baked PEDOT-PSS films of 240 to 380 Ω are then used for further fabrication.

Step 3: To eliminate the baseline drift, the PEDOT-PSS films from the previous step are immersed in PBS for 30 minutes. This step results in increased resistance of the swollen PEDOT-PSS film, tracked by the Nyquist $Z_{re} = 300 - 500 \Omega$ and $Z_{im} = 80 - 150 \Omega$ values.

Step 4: The cyclic voltammogram is indicative of EDOT polymerization quality and phage entrapment. The shape of the voltammogram along with the anodic peak current (i_p) values are important screening parameters. The i_p separation between two subsequent scans is approximately 1×10^{-4} A.

Step 5: Visual inspection of the newly formed biorecognition layer for any abrasions, prevents unusual Nyquist drift and non-specific signals.

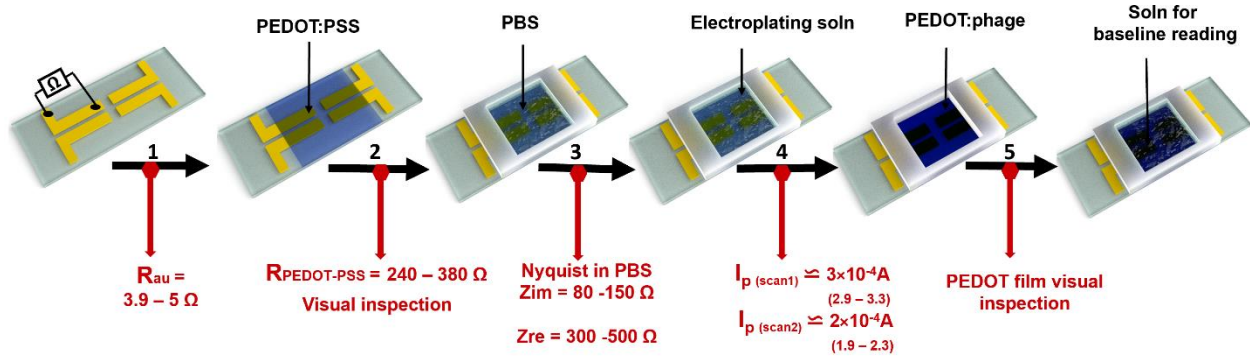


Figure A.1. Process flow for the VBR fabrication process, including the process window parameters that were enforced for this process, indicated in red.

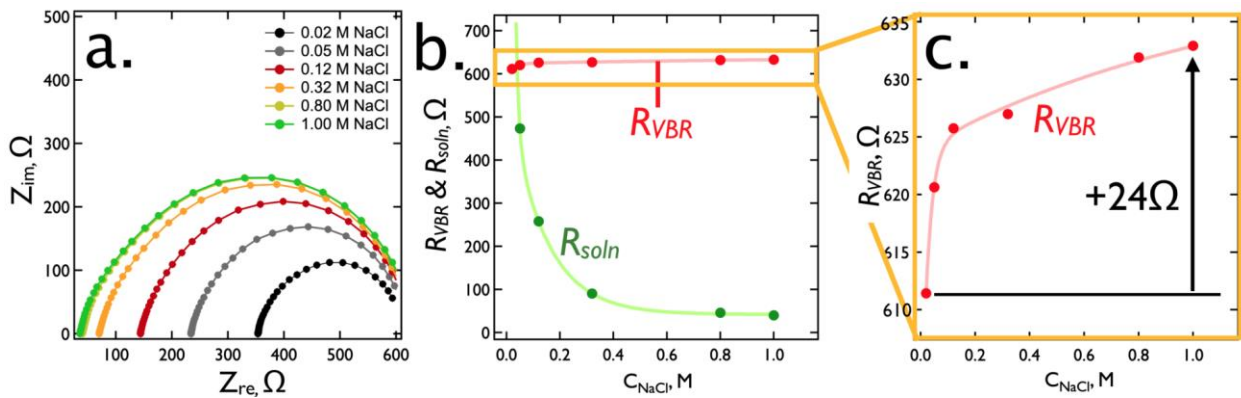


Figure A.2. – Influence of C_{NaCl} on VBR response in the absence of protein. a). Nyquist plots for a single VBR in six aqueous NaCl solutions ranging in concentration from 0.02 M to 1.0 M,

as indicated. b). Plot of R_{VBR} and R_{soln} as a function of C_{NaCl} . R_{soln} (green trace) decreases in proportion to $1/C_{NaCl}$ qualitatively as expected, but R_{VBR} is weakly affected, increasing by just 24Ω against a background of $\approx 600 \Omega$ (b,c).

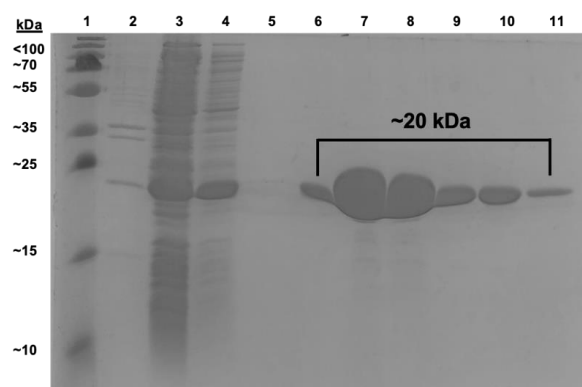
A.2 Expression and purification of the bladder cancer biomarker and protein deglycase DJ-1

The plasmid pET3a-His-DJ1 was heat shock-transformed into BL21(DE3) *E. coli* cells and incubated overnight on an agar plate supplemented with carbenicillin (50 $\mu\text{g}/\text{mL}$). A single colony was selected and inoculated into 20 mL of LB media supplemented with carbenicillin (50 $\mu\text{g}/\text{mL}$) before incubation overnight at 37 °C with shaking at 225 rpm. A 5 mL aliquot of the overnight culture was transferred to 500 mL of LB media supplemented with carbenicillin (50 $\mu\text{g}/\text{mL}$) and shaken at 225 rpm and 37 °C until OD_{600} reached 0.6. The culture was induced through addition of IPTG (1 mM), and was incubated at 30 °C with shaking at 225 rpm for 4 h.

Following bacterial overexpression, the culture was centrifuged at 6 krpm (4302 x g) for 30 min at 4 °C, and the supernatant was discarded. The resulting pellet was resuspended in 25 mL of lysis buffer (1X TBS, 10 mM 2-mercaptoethanol (BME), 1X Halt™ protease inhibitor cocktail, pH 7.5) and lysed by sonication. This lysed cell solution was centrifuged at 10 krpm (11952 x g) for 1 h at 4 °C. The protein was purified from the supernatant by immobilized metal affinity chromatography (IMAC) with Ni^{2+} -NTA resin (BioRad). The resultant eluted fractions were visualized by 12% acrylamide SDS-PAGE and ImageJ analysis (Figure A.3). The appropriate eluted fractions were combined and stored at -20 °C in storage buffer (1X TBS, 10 mM BME, 50% glycerol, pH 7.5). DJ-1 enzyme activity was assayed by hemithioacetal consumption.¹⁷⁸ Briefly, methylglyoxal (7.5 mM) and L-glutathione (7.5 mM)

were mixed and pre-incubated for 30 min at room temperature in sodium phosphate (50 mM, pH 7.0) to form hemithioacetals. DJ-1 (1 μ M), diluted in sodium phosphate (50 mM, pH 7.0), was then added to the reaction mixture. Changes in hemithioacetal levels were monitored over 90 min as a time-dependent change in the characteristic absorbance at 288 nm.

a.



Lane	Sample
1	PageRuler Plus Prestained Protein Ladder
2	<i>E. coli</i> cell pellet
3	Cell lysate
4	Wash 1
5	Wash 2
6	Elution 1
7	Elution 2
8	Elution 3
9	Elution 4
10	Elution 5
11	Elution 6

b.

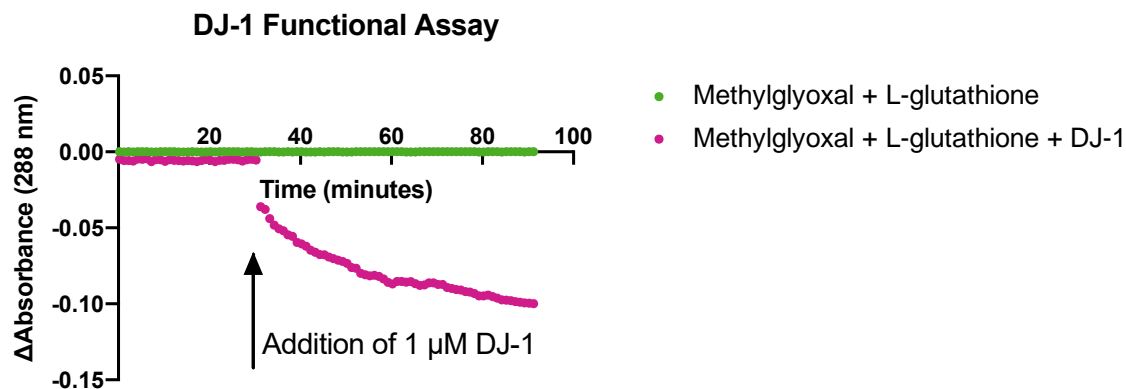


Figure A.3. a). SDS-PAGE analysis of purified DJ-1 after IMAC purification. ImageJ analysis of similar gels quantified DJ-1 purity as >99% post-purification. b). DJ-1 enzyme activity assay. DJ-1 (1 μ M) was added to methylglyoxal (7.5 mM) and L-glutathione (7.5 mM). The

decrease in absorbance at 268 nm over 90 min compared to the negative control indicates changes in hemithioacetal levels and demonstrates the expected DJ-1 enzyme activity.

A.3 Selection of DJ-1 ligands

Four rounds of phage-based selections identified four DJ-1 binding phage. In each round, 15 wells of a 96-well Nunc MaxiSorp microtiter plate were coated with DJ-1 (10 µg/mL) in PBS (pH 8.0, 100 µL per well) and incubated overnight at 4 °C with shaking at 150 rpm. This solution was discarded and a blocking solution containing 0.2% (w/v) nonfat milk in PBS (400 µL per well) were added to the wells, and the plate was incubated at room temperature at 150 rpm for 30 min. In sequential rounds, this blocking step was performed with hen egg white lysozyme, ovalbumin, or a mixture of BSA and HSA to minimize selection of peptide ligands to blocking agents.

After washing three times with wash buffer (0.05% (v/v) TWEEN 20 in PBS, 300 µL per well), mega random peptide libraries (MRPLs)⁶⁶ were diluted to a final concentration of 60 nM in binding buffer (0.2% (w/v) BSA, 0.05% (v/v) TWEEN 20 in PBS). The diluted libraries were added to the microtiter plate (100 µL per well) before incubation for 90 min with shaking at 150 rpm at room temperature. Next, the wells were washed to remove non-specific phage ligands. In each round of selections, the numbers of washes were increased by three to a maximum of 15.

The bound phage were eluted from the plate by adding 0.1 M HCl (100 µL per well) and sonicating the plate in a water bath for 10 min. The eluted phage solution was immediately neutralized by transferring the solution to 1/3 volume of Tris-HCl (1 M, pH 8.0). A portion of the eluted phage solution was used to infect a 20 mL LB culture (supplemented with 5

µg/mL tetracycline) of log phage *E. coli* XL1 Blue cells. The cells were incubated with shaking at 225 rpm at 37 °C for 1 h. Next, the culture was further infected with M13K07 helper phage (NEB) to achieve a multiplicity of infection of 4.6. After 45 min of incubation at 37 °C with shaking at 225 rpm, the culture was transferred to 200 mL of 2YT (16 g tryptone, 5 g NaCl, 10 g yeast extract in 1 L autoclaved water) supplemented with 50 µg/mL carbenicillin and 20 µg/mL kanamycin and incubated at 225 rpm at 37 °C for 16 to 18 h.

The cultures were centrifuged at 10 krpm (15300 x g) for 10 min. The supernatant was decanted into a centrifuge tube containing 1/5 the volume of PEG-8000 (20%, w/v) and NaCl (2.5 M). The tube was inverted 5 times and stored on ice for 30 min followed by an additional centrifugation at 10 krpm (15300 x g) for 15 min. The supernatant was decanted, and tubes were centrifuged for an additional 4 min at 4 krpm (2429 x g). The pellets were resuspended in PBS and the precipitation steps were repeated. Phage concentrations were quantified by measuring absorbance at 268 nm. Finally, the phage were diluted to 60 nM, flash frozen with glycerol (10%, v/v), and stored at -80 °C.

After four rounds of selections, spot assays were performed on 96 selectants. Briefly, individual phage colonies were amplified in 96 deep well plates as before. After centrifugation at 3 krpm (1462 x g), the supernatants were assayed by phage-based ELISA (see *Phage ELISA* method) to assess binding to either DJ-1 or the blocking agent, casein. From these screens, four unique potential DJ-1 ligands were isolated and identified by Sanger sequencing. The peptides' specificity for DJ-1 was tested by additional screening for binding to a panel of proteins including BSA, HSA, ovalbumin, lysozyme, and *E. coli* supernatant. Only two of the four potential ligands showed specificity for DJ-1 (Table A1).

Ultimately, only one ligand was incorporated into the sensor design due to its significantly stronger apparent binding affinity than the other ligand, as measured by ELISA. This ligand is referred to as DJ-1 ligand one (DL1).

Table A.1. DJ-1 binding ligand peptide sequences isolated by phage display selections.

Ligand	1	2	3	4	5	6	7	8	9	10	11	12	13	14	15	16	17	18	19	20
DL1	K	Y	R	Y	V	C	H	D	V	G	G	T	L	Y	C	I	R	D	*	V
DL2	R	P	T	L	Q	E	L	C	*	T	I	Y	V	C	Y	F	V	D	L	G

Asterisk (*) indicates TAG Amber stop codon.

A.4 Site-directed mutagenesis of DL1

A.5 Phage propagation and purification

The phagemid DNA was transformed into SS320 competent *E. coli*, and transformants were plated on a carbenicillin-supplemented (50 µg/mL) agar plate before incubation at 37 °C overnight. A single colony was selected to inoculate 25 mL of 2YT supplemented with carbenicillin (50 µg/mL) and tetracycline (2.5 µg/mL). The culture was shaken at 37 °C until OD₆₀₀ reached 0.5; then, 30 µM IPTG and sufficient M13KO7 to achieve a multiplicity of infection of 4.6 was added. After an additional 45 min incubation, 8 mL of the culture was used to inoculate a 150 mL of 2YT supplemented with carbenicillin (50 µg/mL), kanamycin (20 µg/mL), and IPTG (30 µM). This culture was incubated at 30 °C with shaking at 225 rpm for 18 h.

The phage were precipitated as described above, and the resulting phage pellets were resuspended in 1X PBS with TWEEN 20 (0.05%, v/v) and glycerol (10%, v/v), separated into

1 mL aliquots, flash frozen with liquid nitrogen, and stored at -80 °C. To prepare for devices or ELISAs, the phage solution was thawed on ice, precipitated a second time, and diluted to 40 nM in either LiClO₄ (12.5 mM) or PBS, respectively.

A.6 Phage ELISA

To characterize the apparent binding affinity of the selected phage, 5 µg/mL of DJ-1 in Na₂CO₃ (50 mM, pH 9.6, 100 µL per well) were added to a 96-well Nunc MaxiSorp microtiter plate. The plate was incubated at 4 °C with shaking at 225 overnight. Next day, the solution was discarded and a blocking solution of BSA (0.2%, w/v) in PBS (400 µL per well) was added to the coated wells. The plate was next incubated at room temperature for 30 min with shaking at 150 rpm. The coated wells were washed three times with wash buffer (300 µL per well), followed by the addition of either DL1 or negative control Stop4 phage serially diluted in binding buffer (100 µL per well). The plate was incubated for 60 min at room temperature and shaking at 150 rpm. Next, the plate was washed three times. Finally, a 1:5000 dilution of HRP/anti-M13 monoclonal conjugate (GE Healthcare Life Sciences, 100 µL per well) was added, and the plate was incubated at room temperature with shaking at 150 rpm for 30 min. After five additional washes with wash buffer and one with PBS, 1-Step™ Ultra TMB-ELISA Substrate Solution (ThermoScientific, 100 µL per well) were added to each well. After 5 min, H₂SO₄ (2 M, 100 µL) was added to the wells and the absorbance at 450 nm was measured with an Epoch Microplate Spectrophotometer (BioTek). Data were analyzed with GraphPad Prism 8 and fit with a four-parameter logistic curve fit. The apparent dissociation constant ($K_{d, app}$) for the interaction between the phage-displayed DL1 and DJ-1 was calculated to be 14 pM.

A.7 DJ-1 phage-antibody sandwich ELISA

To simulate the DJ-1/DL1 interaction in the VBR format, DL1 (1 nM) and Stop4 (1 nM) phages were bound to a 96-well microtiter plate as described above. The plate was treated identically to the indirect phage ELISA until the first binding step; DJ-1 dilutions were prepared and 100 μ L of the diluted proteins were added to every well. The plate was incubated for 60 min at room temperature with shaking at 150 rpm. After washing three times with wash buffer, the primary antibody, PARK7/DJ-1 Antibody (LifeSpan Biosciences, Inc.), was diluted to 1:1000 in binding buffer and 100 μ L were added to each well. The plate was incubated again for 60 min at room temperature with shaking at 150 rpm, and washed three times. A secondary antibody, anti-rabbit IgG (Sigma-Aldrich), was diluted to 1:5000 in binding buffer and 100 μ L were added to each well. The plate was incubated for 30 min and washed five times with wash buffer and once with PBS. Finally, the HRP activity was detected as described above and the $K_{d,app}$ was determined to be 206 nM. (Figure 3.1b)